Thermal Stability, Microstructures and Mechanical Properties of Nanostructured/Ultrafine Structured Cu-5vol.%Al_2O_3 Nanocomposites Fabricated by High Energy Mechanical Milling and Powder Compact Extrusion

A thesis

submitted in fulfillment

of the requirements for the degree

of

Doctor of Philosophy

at

The University of Waikato

by

DENGSHAN ZHOU

THE UNIVERSITY OF WAIKATO

Te Whare Wānanga o Waikato

2014

Abstract

Ultrafine structured metal matrix nanocomposites (MMNCs) have received much attention due to their attractive engineering applications and scientific interest. On the engineering aspect, ultrafine structured MMNCs have a higher room temperature strength and better high temperature performance due to grain boundary strengthening, nanoparticle strengthening and Zener pinning effects compared to their metal matrices. On the scientific aspect, there is the question of whether the linear superposition of basic strengthening mechanisms, which is applicable to conventional precipitation-hardened alloys, is still valid in evaluating the strength of ultrafine structured MMNCs. In general, there might be a synergistic effect among different strengthening mechanisms when the grain sizes of matrices of MMNCs are reduced down to the submicrometer range. In this thesis, a model system of Cu-5vol.%Al_2O_3 was selected to study with the aim of deepening and reinforcing the understanding of the microstructure/property relationship and contributions of various strengthening mechanisms to the overall strength of ultrafine structured MMNCs.

Nanostructured Cu-5vol.%Al_2O_3 nanocomposite powder particles were produced by high energy mechanical milling (HEMM) of a powder mixture of Cu powder and Al_2O_3 nanopowder. The nanocomposite powders were then annealed at 300-600°C for up to 5 h. The powders had a high thermal stability at temperatures up to 600°C. After annealing at 600°C for 5 h, Cu nanograins in the microstructure of the nanocomposite powder particles only grew slightly and the microstructure of the Cu matrix of powder particles was still well within the nanostructure range. The activation energy for the grain growth of the Cu nanograins was determined to be 63.4 kJ/mol, which is much lower than that of coarse grained monolithic Cu and similar to that of nanocrystalline monolithic Cu, and suggests the grain growth behavior is controlled by grain boundary diffusion. The impressive thermal stability of the microstructure of the powder particles is mainly associated with the effect of Al_2O_3 nanoparticles on the grain growth through inhibiting the grain boundary diffusion.

Ultrafine structured Cu-5vol.%Al_2O_3 nanocomposite samples were synthesized by powder compact extrusion at 750 and 900°C, and their microstructures and tensile properties were characterized. The microstructural characterization showed that there is no significant difference in the mean Cu grain sizes for both samples but the sample extruded at 900°C has far less Al_2O_3 nanoparticles in comparison to the sample extruded at 750°C. The tensile testing results exhibited that the 900°C extruded sample has a larger strength and higher ductility at fracture as compared to those of the 750°C extruded sample. This shows that the dissolution of Al_2O_3 nanoparticles in the Cu matrix takes place when the powder compact is heated and extruded at 900°C, and the dissolution of the Al_2O_3 nanoparticles leads to superior tensile properties of the sample extruded at 900°C.

Further ultrafine structured Cu-5vol.%Al_2O_3 nanocomposite samples were prepared by extrusion of powder compacts of nanostructured Cu-5vol.%Al_2O_3 nanocomposite powder at temperatures ranging from 300 to 900°C. The experimental results showed that Cu grains and the sizes and volume fractions of Al_2O_3 nanoparticles of bulk ultrafine structured Cu-5vol.%Al_2O_3 nanocomposite samples increased with the increase of the extrusion temperature. The average sizes of Cu grains and Al_2O_3 nanoparticles and the volume fraction of Al_2O_3 nanoparticles of the extruded samples increased from 132 nm, 43 nm and 0.75% to 263 nm, 100 nm and 4%, respectively, as the extrusion temperature increased from 300 to 900°C. The increases in the sizes and volume fraction of the Al_2O_3 nanoparticles with the increase of the extrusion temperature were caused by the precipitation of Al_2O_3 nanoparticles during extrusion. The samples extruded at 400°C or lower fractured prematurely without yielding, while the samples extruded at T≥500°C fractured after yielding. The yield strengths and ultimate tensile strengths of such materials changed only slightly with the increase of the extrusion temperature and had values in the range 466-517 and 546-564 MPa. However, the tensile ductility of the extruded samples was proportional to the extrusion temperature and increased from 0.76 to 5.82% with increasing the extrusion temperature from 500 to 900°C. The slight decrease of yield strength and significant

increase of the ductility of the consolidated sample with increasing extrusion temperature suggests that the level of interparticle atomic bonding in the consolidated samples increases with increased extrusion temperature. It is speculated that the fracture of the samples extruded at T $\leq 800^{o}C$ is associated with the weak bonding of residual interparticle boundaries which have not been transformed into grain boundaries. When the extrusion temperature T $\geq 800^{o}C$, the area of the residual interparticle boundaries may be too small to play any major role in causing the fracture of the consolidated sample. Analysis of the contributions of different strengthening mechanisms demonstrates that grain boundary strengthening makes the largest contribution to the strength of the extruded samples relative to the nanoparticle strengthening and strain hardening and experimentally measured yield strength of the extruded samples can be predicted appropriately by the sum of Peierls stress, grain boundary strengthening, nanoparticle strengthening and strain hardening.

The effect of annealing on an ultrafine structured Cu-5vol.%Al_2O_3 nanocomposite sample made by powder compact extrusion at $900^{o}C$ was investigated by annealing for 1h at different temperatures in the range of 500-$900^{o}C$. This revealed that Al_2O_3 nanoparticles provided excellent thermal stability to the ultrafine structured Cu-5vol.%Al_2O_3 nanocomposite sample. The microstructure and microhardness of the sample remained stable up to annealing at $800^{o}C$ for 1 h. High resistance of Al_2O_3 nanoparticles to coarsening was responsible for this high thermal stability. The microhardness increase observed for the sample annealed at $700^{o}C$ for 1 h came from the precipitation of small Al_2O_3 nanoparticles. On the other hand, the sudden drop in microhardness of the sample annealed at $900^{o}C$ for 1 h was related to the coarsening of small Al_2O_3 nanoparticles and grain growth of the Cu matrix.

This thesis concludes with suggestions for future work that would extend on from the findings presented here.

List of Publications

Zhou DS, Zhang DL, Munore P, Kong C (2013) Factors Controlling the Tensile Properties of Ultrafine Structured Cu-5vol.%Al_2O_3 Nanocomposite Prepared by High Energy Mechanical Milling and Powder Compact Extrusion. Materials Science and Engineering: A 84:64-72.

Zhou DS, Torrens R, Zhang DL, Munore P, Kong C (2014) Thermal Stability of the Nanostructure of Mechanically Milled Cu-5vol.%Al_2O_3 Nanocomposite Powder Particles. Journal of Materials Research 29(8): 996-1005.

Zhou DS, Torrens R, Zhang DL, Munore P, Kong C (2014) Grain and Nanoparticle Coarsening of an Ultrafine Structured Cu-5vol.%Al_2O_3 Nanocomposite during Isochronal Annealing. Submitted.

Zhou DS, Torrens R, Zhang DL, Munore P, Kong C (2014) A high strength and high electrical conductivity ultrafine grained Cu-5vol.%Al_2O_3 composite prepared by high energy mechanical milling and powder compact extrusion. In preparation.

Acknowledgements

I would like to take this opportunity to thank some people who helped me when I was in hard times during the last three years. Without the kind and selfless assistance, it is very hard to image how I could have got through those years.

I am grateful to my three mentors: Dr Rob Torrens, Prof. Janis Swan and Prof. Deliang Zhang. I appreciate Rob's considerable effort in editing the thesis. He carefully and strictly checked every single sentence in the thesis and gave many valuable suggestions and comments to improve it. He even processed the chapters of the thesis when he was on his holiday. I owe him a formal thanks: Thank you very much, Rob. Janis shared with me some useful experiences on how to write a good thesis. I am indebted to Deliang for the offer from the University of Waikato which enrolled me as a PhD candidate in the School of Engineering. Deliang has an international scientific vision in the field of powder metallurgy. He is always nice and was patient with my mistakes. During the past three years, he has never stopped training me on how to write a good scientific paper and how to perform quality scientific work.

I would like to thank Dr Charlie Kong and Prof. Paul Munroe from the University of New South Wales, Australia. They helped me with the preparation of TEM specimens of powder and bulk samples by FIB and the production of TEM pictures from the FIB specimens. I thank them for their cooperation and contribution to this thesis. I'd also like to give my thanks to Prof. Challapalli Suryanarayana from the University of Central Florida, USA, for his suggestion on cryomilling.

I would like to extend my gratitude to the technical and administrative staff from the School of Engineering of the University of Waikato: Chris Wang, Yuanji Zhang,

Helen Turner, Brett Nichol, Indar Singh, Steve Hardy, Annette Rodgers and Mary Dalbeth.

I am highly obliged to my colleagues from the metallic materials research group for their assistance, support and understanding in both the research project and daily life. Dr Mingtu Jia, Mr Zhibo Zhang, Mr Huiyang Lu and Dr Fei Yang helped me with the extrusion of samples. Miss Qian Xu showed me many beautiful places around Hamilton City and taught me to drive. Mr Amro Gazawi taught me ball milling when I first joined in the group. Ms Stella Raynova was always nice and supportive when I asked for her help. I had many pleasant talks and chats with Mr Navaneeth Velluva, Mr Kenneth Sichone, Mr Izhar Aziz, Mr Paul Ewart and Mr Jia Lou.

I want to express my huge appreciation to my family members, especially to my lovely and sweet wife, Mrs Qian Bu; she has always been supportive and understanding.

Finally, the financial support from the China Scholarship Council, China; and Ministry of Science and Technology, New Zealand; has been greatly appreciated.

Table of Contents

List of Figures

List of Tables

Abbreviations

BSE	Backscattered Electron
CG	Coarse Grained
DS	Dispersion Strengthened
ECAP	Equal Channel Angular Pressing
EDM	Electric Discharge Machining
EDX	Energy Dispersive X-Ray Spectroscopy
FIB	Focused Ion Beam
HEMM	High Energy Mechanical Milling
HIP	Hot Isostatic Pressing
HPT	High Pressure Torsion
MMCs	Metal Matrix Composites
MMNC	Metal Matrix Nanocomposite
MMNCs	Metal Matrix Nanocomposites
NC	Nanocrystalline
ODS	Oxide Dispersion Strengthened
PCE	Powder Compact Extrusion
SADPs	Selected Area Electron Diffraction Patterns
SE	Secondary Electron
SEM	Scanning Electron Microscopy
STEM	Scanning Transmission Electron Microscopy
SPS	Spark Plasma Sintering
TEM	Transmission Electron Microscopy
UFG	Ultrafine Grained
UFS	Ultrafine Structured
UTS	Ultimate Tensile Stress
XRD	X-Ray Diffraction
XRF	X-Ray Fluorescence
YS	Yield Strength

Chapter One

Introduction and Literature Review

1.1 Introduction

The high energy mechanical milling (HEMM) method was invented in 1970 by John S. Benjamin [1]. He initially employed it to uniformly distribute Y_2O_3 and ThO_2 nanoparticles in nickel-based superalloys to improve their high temperature strength. Later, HEMM was extensively and frequently used to produce various complex composite materials to extend their high temperature applications. In 1989, Luton and co-workers [2] milled a mixture of Al and Al_2O_3 powders in liquid nitrogen media. The milled powder was then treated by hot isostatic pressing (HIP) followed by hot extrusion to synthesize Al-Al_2O_3 composites with a grain size in the range of 50-300 nm. They found that most particles in the composite sample were complex aluminum oxy-nitride particles which were typically 2 to 10 nm in diameter. This fine structured Al strengthened by Al(ON) particles exhibited excellent room and high temperature properties in tensile and creep tests. In the same year, the terminology of nanocrystalline (NC) was proposed officially in a review by Herbert Gleiter [3]. From this review, it is known that HEMM is one of the most powerful methods to produce NC materials which typically have mean grain sizes less than 100 nm. Such new materials are expected to possess unique strength according to the extrapolation of the Hall-Petch relationship [4-5]. However, NC materials are naturally unstable [6-7] due to the presence of a vast amount of grain boundaries. This intrinsically unstable character of NC materials makes their consolidation at high temperatures without significant coarsening impossible as NC grains have a huge driving force to grow. To make use of the unique mechanical and physical properties associated with the high volume fraction of grain boundaries, it is of vital importance to prepare bulk NC samples.

Huang et al. [8] in 1992 reported that the cryomilled NC NiAl still maintained a nanostructure with a grain size in the range from 10 to 40 nm after one hour annealing at 1100°C and concluded that the inhibition of AlN nanoparticles on the grain growth was responsible for the high thermal stability observed. This finding indicates that NC materials can be fabricated with the help of second phase nanoparticles, which may make the production of bulk ultrafine grained (UFG) and NC materials viable.

In this PhD study, a composite powder of nanostructured Cu matrix with a dispersion of 5vol.%Al_2O_3 nanoparticles was prepared by HEMM of a mixture of copper powder and alumina nanoparticles. Grain growth kinetics of the nanostructured composite powder, along with microstructures and tensile properties of bulk samples made by extrusion of the powder compacts of nanostructured composite powder at different temperatures was investigated. Furthermore, a relationship which predicts the yield strength of the ultrafine structured (UFS) Cu-5vol.%Al_2O_3 nanocomposite is proposed based on an analysis of different strengthening mechanisms in the extruded samples and the effect of isochronal annealing of bulk ultrafine structured Cu-5vol.%Al_2O_3 extruded at 900°C.

This thesis has seven chapters. Chapter One reviews the literature on NC/UFG metals and alloys, including strength, ductility, and stability. The research on second phase nanoparticle dispersion strengthened (DS) Cu matrix composites is also considered in Chapter One. The initial materials and experimental procedures are provided in Chapter Two. In Chapter Three, the grain growth kinetics of nanostructured Cu-5vol.%Al_2O_3 composite powder particles is presented and discussed. Chapter Four presents and analyzes the factors in determining the yield strength of extruded UFS Cu-5vol.%Al_2O_3 composite samples, which has been published in the Journal of Materials Science and Engineering A (see Appendix A). Chapter Five presents the effect of extrusion temperature on microstructure and tensile properties of extruded UFS Cu-5vol.%Al_2O_3 composite samples. A basic model is proposed to predict the yield strength of the extruded sample based on the discussion of the dependence of

strengthening mechanisms on microstructural features. Chapter Six presents and describes the effect of heat treatment on the microstructure and hardness of the sample extruded at 900°C. Conclusions and recommendations for the future research are summarized and given in Chapter Seven.

1.2 Overview of NC Metals and Alloys

NC metals and alloys, typically with an average grain size less than 100 nm, exhibit quite different deformation behavior and microstructural response to loading as compared with their coarse-grained (CG) counterparts. For conventional materials, plastic deformation is dominated by a dislocation-assisted process and both the flow stress and grain size normally do not vary with the loading conditions, whereas in NC materials the deformation is mainly determined by a grain boundary-mediated process, moreover, the flow stress exhibits a high strain rate sensitivity (face-centered cubic NC metals) and dynamic grain growth probably occurs during prolonged mechanical tests [9-12]. Such unique behaviors observed in NC materials are closely related to their nanoscale grains, i.e. a substantial proportion of atoms reside at grain boundaries. Due to this intrinsically microstructural feature, NC materials possess a very high strength and hardness. However, both nanograins and large volume fraction of the grain boundary present in NC materials also lead to poor ductility and disappointing thermal stability which severely limit their structural applications and service temperatures [13-15]. Hence, some critical issues such as the synthesis of bulk samples, ductility and microstructural and thermal stabilities must be overcome for NC materials to be used extensively as structural components.

1.3 Mechanical Properties of NC and UFG Metals/Alloys

1.3.1 Strength

The strength of single phase conventional polycrystalline materials is dependent on the interaction of dislocations with intragranular defects (such as solute atoms, dislocation configurations and stacking faults) and grain boundaries. As grain sizes are significantly reduced, intragranular defects are effectively suppressed which results in pronounced grain boundary strengthening. The enhanced strength (or hardness) due to grain size reduction can be derived from the empirical Hall-Petch relation [4-5]:

$$\Delta\sigma_{gb} = k_{HP} d^{-1/2} \qquad (1\text{-}1)$$

where $\Delta\sigma_{gb}$ is the increase of yield strength due to grain boundary strengthening, k_{HP} is a material-dependent constant and d is the mean grain size. Based on Equation (1-1), extraordinary mechanical strength can be expected through nanostructuring. Indeed, ultrahigh strength and hardness have been observed recently in NC and UFG metals. For example, hardness has been found to increase with decreasing grain size [16] in Cu with grain sizes as small as 10 nm still following the Hall-Petch relationship and the corresponding hardness of 3 GPa is about 20 times higher than that in CG Cu (~150 MPa). A summary of the hardness of Cu vs. $d^{-1/2}$ based on the data reported in the published literature [17-23,16,24] is presented in Figure 1.1.

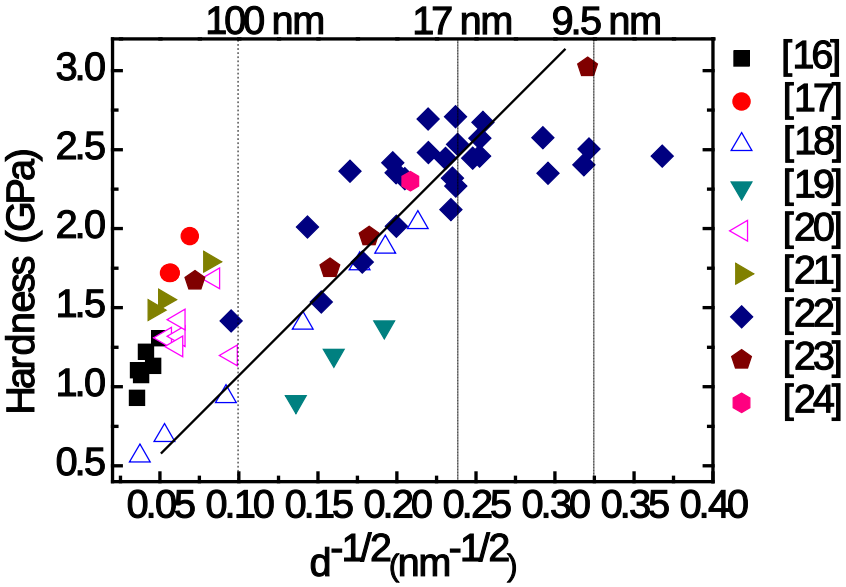

Figure 1.1: Dependence of hardness of Cu on its grain size.

As shown in Figure 1.1, for some Cu sample, however, the dependence of the hardness on the grain size is still valid for grain sizes smaller than 15 nm. Similar Hall-Petch relationships between hardness and grain size have also been reported by Knapp and Follstaedt for NC Ni [25] and by Schuh et al. in NC Ni-W alloys [26] where the grain size is in the several nanometer scale. Based on experimental observations and computer simulations [27-34], it has been widely accepted that the activity of intragranular dislocations is greatly suppressed when the grain size of NC materials is in the range from 30 to 100 nm, in this size range dislocation-dominated deformation still remains; however, with further decreasing the grain size, a transition in the deformation mechanism from the dislocation-assisted deformation to grain boundary-mediated deformation appears, i.e. for the grain sizes below 15 nm, the grain boundary-involved deformation process such as grain boundary sliding and grain rotation dominate the plasticity of the material. Equation (1-1) is established on the physical background of the difficulty of the initiation of dislocations and motion of dislocations inside grains, the Hall-Petch relation breaks down and softening subsequently occurs when the grain boundary-mediated mechanisms start to operate, as shown in Figure 1.1. This so-called inverse Hall-Petch behavior arises when the average grain sizes of NC materials are at very small values (normally less than 15

nm). In such NC materials, the presence of the inverse Hall-Petch effect, which results in softening, is mainly caused by the grain boundary sliding deformation process during loading. This suggests that if the grain boundary sliding deformation behavior in NC materials is greatly limited or even eliminated NC materials could become stronger. Numerous investigations including experiments and simulations have revealed that the suppression of the grain boundary sliding of NC materials can be achieved by low temperature annealing [35-38], high pressure [39], doping with an alloying element which has very limited solubility in the solvent and large atomic size mismatch with the host atoms [40-44] and adding second phase nanoparticles into grain boundaries [45]. For example, as shown in Figure 1.2, the magnitude of the grain boundary sliding of Cu strongly depends on the atomic size of the alloying element doped in grain boundaries.

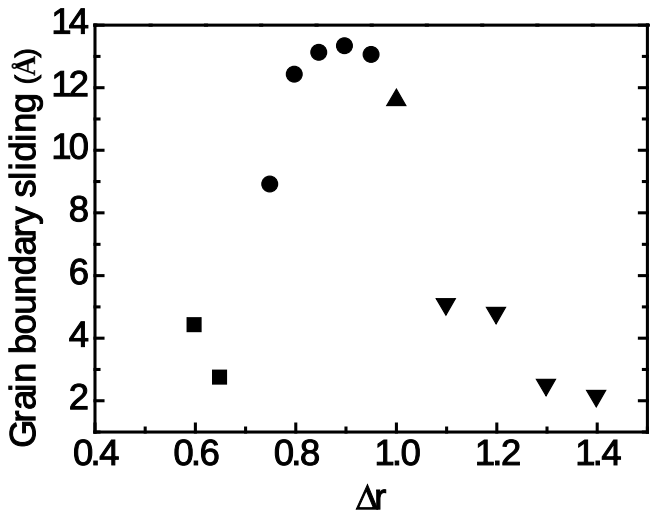

Figure 1.2: Magnitudes of grain boundary sliding versus sizes of its dopants [42].

It manifests that the dopants which have large atomic size mismatch with the Cu matrix can effectively inhibit the amount of the grain boundary sliding during loading. Molecular dynamic simulations performed by Vo et al. [41] showed that after doping with up to 1.9 at.% Nb the strength of NC Cu appears to approach the value of the theoretical strength of a perfect Cu single crystal, indicating that the segregated Nb atoms have a pronounced effect on the onset of the plasticity of the NC Cu. Very recently Özerinç et al. [46] verified the simulation result obtained by Vo et. al [41] by

performing nanoindentation hardness measurements on NC Cu-Nb alloys synthesized by direct current magnetron sputtering. Low temperature annealing experiments of NC Ni and Ni-W alloys conducted by Rupert et. al [38] and Wang et. al [35], respectively, showed that after annealing treatments the samples show an increase in their strength. The authors attributed such strength improvement to grain boundary relaxation. The results mentioned above demonstrate that the mechanism of plastic deformation of NC materials can be influenced by their grain boundary energy and/or grain boundary chemical composition, which indicates that the properties of NC metals and alloys could be enhanced by engineering their grain boundaries.

1.3.2 Ductility

In general, for a metal, ductility and strength are mutually exclusive, i.e. one normally should sacrifice one of them to achieve the enhancement of the other. Refining grain sizes down to the nanometer scale can appreciably improve the strength of metals based on the Hall-Petch relationship. Their ductility, however, decreases markedly with the reduction of the grain size. Elongations at fracture for some NC metals and alloys was extracted from published data [47-50,35,23,51-74] and is shown in Figure 1.3.

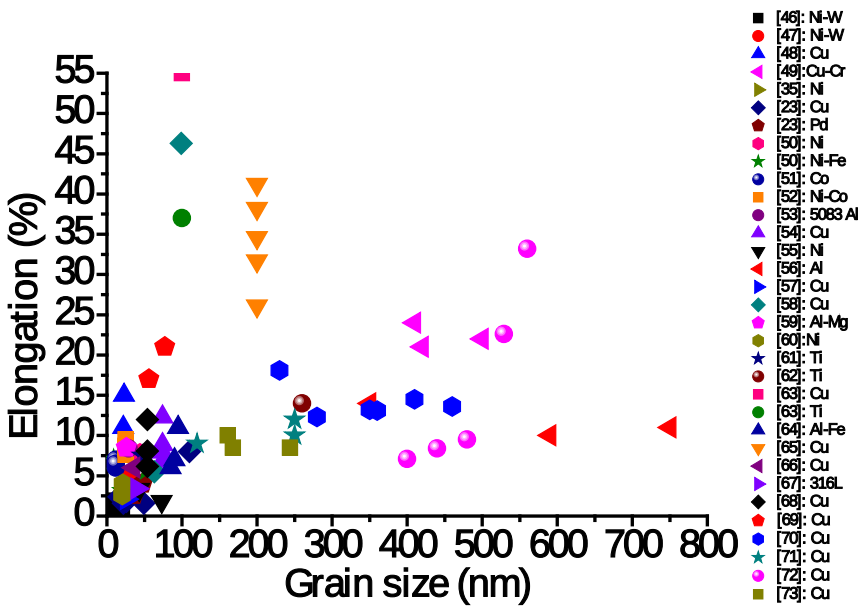

Figure 1.3: Elongation versus grain size.

From Figure 1.3, it is clear that most of the elongations to fracture of NC materials are less than 10%. Although the majority of elongations at fracture for UFG materials are in the range of 10%-30%, this result is still worse than that of CG materials. According to the reported literature, poor ductility in UFG and NC materials compared to their conventional counterparts may come from the following three factors [75-76,14,77,13,78-82]: (1) high sensitivity to flaws from processing and sample preparation processes; (2) low strain hardening capability due to small grains and (3) low resistance to crack propagation because of a large amount of grain boundaries. In other words, to obtain good ductility in high strength UFG and NC materials, the sample synthesized is required to have a high purity as well as possess a high strain hardening ability to prevent the early onset of the localized deformation.

Continuous effort by researchers around the world has found that artifact-free bulk NC materials can be produced using one step techniques based on severe plastic deformation methods, such as equal channel angular pressing (ECAP) [83-84], high pressure torsion (HPT) [85] and hydrostatic extrusion [62]. Sanders et al. [23] has shown that purifying NC metals could further improve their extraordinary strengths, whereas their ductility is still disappointing. Low ductility of a high purity NC metal originates from its small grains [86]. It has been shown that the plastic deformation of NC materials under externally applied forces is accommodated by grain boundary-related relaxation processes such as emission and absorption of dislocations at grain boundaries and grain boundary sliding as traditional Frank-Read sources are not allowed to exist within nanoscale grains [31]. Such deformation mechanisms in NC materials leads to a very poor storage of dislocations during deformation and thus the presence of local deformation instability resulting from the weak strain hardening ability. The strain hardening of NC materials can be readily and quickly represented by the ratio of ultimate tensile stress (UTS) to yield strength (YS) [81]. Figure 1.4 shows the ratio of UTS to YS of NC/UFG materials vs. grain size; the ratio in NC/UFG materials is around 1.25 based on the reported work. This value of 1.25 is much lower than that of CG materials, in which such ratio is normally over 2 [81].

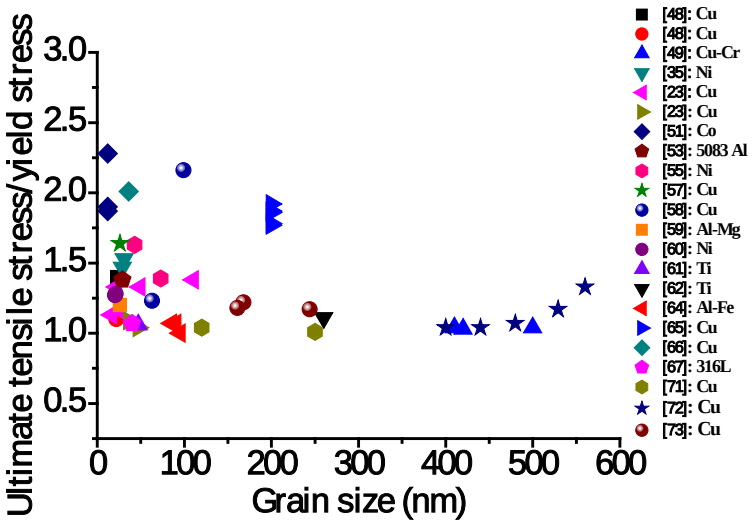

Figure 1.4: Ratios of ultimate tensile strength to yield strength versus grain sizes.

According to Hart's criterion [87], to maintain stable deformation to a large strain in tension for a tested specimen, the following relation has to be satisfied:

$$\gamma + m \geq 1 \qquad (1\text{-}2),$$

where γ is the normalized strain hardening rate and equal to $\frac{1}{\sigma}(\frac{\partial \ln \sigma}{\partial \ln \dot{\varepsilon}})_{\varepsilon,T}$ and m is the strain rate sensitivity and equal to $\left(\frac{\partial \ln \sigma}{\partial \ln \dot{\varepsilon}}\right)_{\varepsilon,T}$. Equation (1-2) suggests that for a material with small grains one could improve either strain hardening rate or strain rate sensitivity to achieve a large stable strain during tensile testing. With this idea, various strategies such as bimodal grain size distribution [86,88-89], second phase particles/precipitates [90-95], stacking faults [96-97], and twins [98-99], have been used to extend a high strain hardening rate to a large plastic deformation to delay and suppress the onset of the localized plastic deformation of NC and UFG metals/alloys. For a bimodal NC system, small grains offer strength and large grains provide room for the accumulation of dislocations and blunt cracks [86]. In such systems, stable strain hardening is provided by large grains. Hence, these systems normally have high ductility but relatively low yield strength as large grains yield prior to the yielding of small grains. To enhance the ductility of NC/UFG materials without sacrificing their exceptional strength, one introduces intragranular defects such as second phase precipitates, stacking faults and twins to transfer the accumulation of dislocations

from grain boundaries to grain interiors. Both strength and ductility of NC/UFG materials can be improved significantly. According to the Equation (1-2), the stable plastic deformation of NC/UFG materials during tensile testing can also be extended by increasing the value of the strain rate sensitivity. Unlike the strain hardening rate which determines the level of the uniform deformation, a high strain rate sensitivity can effectively diffuse local necking to resist inhomogeneous deformation and then offer a noticeable post-uniform deformation [100-101]. Indeed, near-perfect tensile stress-strain curves can be produced by using a low strain rate at which the strain hardening is considered to be absent [102-103]. Overall, the tensile properties of NC/UFG materials can be optimized by achieving high strain hardening capacity and strain rate sensitivity via tailoring the microstructures of grains and/or grain boundaries.

1.4 Stability of NC Materials

NC materials are inherently thermodynamically unstable due to the presence of the high volume fraction of grain boundaries. Accordingly, under high consolidation temperatures, nanostructured powder particles always tend to spontaneously reduce their total grain boundary area (i.e. grain growth) to decrease the free energy of the system. This coarsening behavior during consolidation of nanostructured powder particles should be suppressed/avoided to retain the unique properties of NC materials. It has been shown that the driving force for grain growth is from the curvature of the boundary [104-105] in which the velocity, ν, of the grain boundary motion can be expressed as:

$$\nu = M \frac{\gamma_0}{R} \qquad (1\text{-}3),$$

where M, which follows an Arrhenius relationship, is the grain boundary migration, γ_0 is the specific grain boundary energy and R is the mean grain radius. According to Equation (1-3), it is clear that both thermodynamic and kinetic strategies can be

applied to stabilize the nanostructure of the material. The thermodynamic concept for stabilization of nanostructures was first proposed by Jörg Weissmüller [106-107] on the basis of a dilute solid solution alloy and had an initial form as given below:

$$\gamma = \gamma_0 - \Gamma\left(\Delta H^{seg} - kT\log[X]\right) \quad (1\text{-}4),$$

where the grain boundary energy with segregated solute atoms (γ) is a linear function of the grain boundary energy of pure solvent (γ_0), enthalpy of segregation, ΔH^{seg}, and segregation entropy change ($kT\log[X]$). Γ, k, T and $[X]$ in Equation (1-4) are the solute excess at the grain boundary, Boltzmann constant, absolute temperature and global solute content, respectively. In Equation (1-4), Weissmüller just considered the elastic strain energy contribution to the segregation enthalpy under which γ may be reduced to be 0 if a sufficiently high atomic size mismatch between solute and solvent atoms is present and in the meantime the solute has a strong segregation tendency in the solvent. In this situation, NC grain size stabilization can be completely achieved since the driving force for grain growth disappears. However, in addition to the elastic strain energy caused by the size mismatch, both electronic interaction and surface energy also play roles in the enthalpy of grain boundary segregation [108-109]. Darling and co-workers incorporated the electronic interaction into the segregation enthalpy and then developed a modified thermodynamic equation to predict the thermal stability of NC Fe alloys [110-111]. The predicted results were in good agreement with the experimental evidence. Although the aforementioned thermodynamic method has success in some NC alloy systems for a certain range of temperatures, the stability of the nanostructure achieved through it mainly depends on the equilibrium of grains and grain boundaries of the material to the solute concentrations. This suggests that the nanostructure in NC alloys with segregated atoms would lose its stability if the equilibrium state of the grain boundaries in the solute content is interrupted and disturbed such as the precipitation of the second phase. Indeed, several studies have confirmed the loss of the thermal stability of NC alloys due to the formation of the intermetallic compounds [111-112].

Hence, complete stability of NC materials requires them being stable against both grain growth and phase separation. To evaluate whether a NC alloy system with a positive enthalpy of mixing can reach the complete stability or not, Murdoch and Schuh [113-114] recently developed an analytical model based on the regular solution model to achieve this goal. They used their own model to calculate the minimum energy NC free energy curve and then compared it with the classical bulk phases. As a result, a criterion associated with the enthalpies of mixing and segregation was derived by them for predicting the complete stability of binary NC alloys. It is worth pointing out that the kinetic technique stemming from the solute drag also plays a part in the thermodynamic stabilization of NC alloys.

Based on Equation (1-3), the kinetic strategy which can effectively slow down the grain boundary mobility, M, through pore drag, solute drag or pinning by precipitates or second phase nanoparticles is another important way to stabilize NC materials. Although the kinetic strategy cannot completely stop the grain growth of NC materials at very high temperatures as M follows an Arrhenius relationship, it can significantly reduce the growth rate of NC grains and thus limit the mean grain size in the nanometer scale. In a recent review, Koch and co-workers [115] concluded that the kinetic strategy by Zener pinning in NC stabilization is more effective than the thermodynamic method for $T \geq 0.75\ T_m$ (T_m is the melting point of the matrix in Kelvin scale). The kinetic strategy was first proposed by Zener and reported by Smith [116] to relate the grain size to second phase particles. According to Zener's analysis, second phase particles with a volume fraction, f, and a radius, r, will exert a pinning force on the grain boundary when they are distributed uniformly into a metal. Such pinning force, F_z, generated by particles will retard the movement of the grain boundary and has the following expression [104,116]:

$$F_z = \frac{3 f \gamma_0}{2r} \qquad (1\text{-}5).$$

On the other hand, for a material with a mean grain radius, R, the driving force for its grain growth, F_d, can be expressed as given below [104,116]:

$$F_d = \frac{2\gamma_0}{R} \quad (1\text{-}6).$$

The grains of the material will cease to grow when an equilibrium state is reached, i.e., $F_z=F_d$. Under this situation, the stabilized grain size of the material is equal to:

$$R = \frac{4r}{3f} \quad (1\text{-}7).$$

Using Equation (1-7), the final grain size of the material with a dispersion of second phase particles can be predicted. However, as Equation (1-7) was derived based on assumptions such as a homogeneous distribution of particles, identical particle size and isotropic grain boundary energy, the final grain size predicted by Equation (1-7) for a second phase particle dispersed system usually deviates from the actual grain size in the material and shows a higher value. To obtain a more accurate prediction, a modified Zener equation was proposed by Manohar and co-workers [117-118] and expressed in the form of:

$$R = 0.17\frac{r}{f} \quad (1\text{-}8).$$

However, in NC systems, second phase nanoparticles tend to locate at positions like grain boundaries, triple junctions and quadruple points [119-120]. For this exceptional situation, it is too early to say that the grain sizes in NC materials with second phase nanoparticles are still dictated by Equation (1-7) or (1-8). In spite of this, the kinetic strategy has had a huge success in the stabilization of NC materials and a series of NC alloys such as NC Al, Mg, Cu and Fe alloys have been produced with the help of Zener pinning [54,121-123].

1.5 Second Phase Nanoparticle DS Cu Matrix Composites

1.5.1 Introduction

The performance of materials has always been required to improve to keep up with the pace of the development of a civilization. For instance, DS copper matrix

nanocomposites have been used to replace conventional copper alloys which are usually produced by a combination of solid solution and thermomechanical processing for high temperature applications such as resistance welding electrodes, electrical contacts and heat-resistant parts [124-125]. In such applications, the retention of high strength and good conductivity at elevated temperatures must be achieved according to the requirements of service conditions. Copper alloys strengthened by both solutes and dislocation configurations cannot maintain such properties at high temperatures, or even for intermediate temperatures, due to the recovery of secondary structures and the sensitivity of conductivity to solute atoms [126]. Although copper alloys reinforced by precipitates of refractory phases (e.g. W, Ta, Nb and Cr) can exhibit good performance within a certain range of temperatures, they usually have lower softening temperatures compared with Cu strengthened by ceramic nanoparticles due to coarsening of precipitates [127]. Copper with a fine dispersion of ceramic nanoparticles not only have a higher strength at elevated temperatures, but also better resistance to softening relative to those copper alloys mentioned above. Hence, DS Cu matrix nanocomposites can substantially extend the materials high temperature applications. As discussed in Section 1.4, it has been well established that second phase nanoparticles distributed at grain boundaries of a metal can exert a pinning force on the grain boundary to resist its migration to suppress the grain growth during thermomechanical processing [116]. Many researchers have successfully fabricated UFG and NC Cu matrix composites via introducing a homogeneous distribution of second phase nanoparticles in the Cu matrix [128-139].

1.5.2 Fabrication of Nanostructured Cu Matrix Composite Powders

It has been pointed out by Morris and Morris [140] that the stability of dispersoids in DS materials is closely associated with their distribution and a homogeneous distribution of dispersoids can effectively resist particle coarsening occurring during the consolidation process; thus refining the microstructure of the matrix and improving the properties of the material. Nanostructured Cu matrix composite powders can be produced by external oxidation [141], thermochemical treatment

[129,133,142], thermal spraying [143] and HEMM [144,135-136,145-147]. Among these approaches, HEMM is the most appropriate to combine with subsequent thermal processing because of its high efficiency in creating a uniform dispersion of second phases, particularly for an immiscible system or a high content of second phase nanoparticles. For example, HEMM is commonly applied to form supersaturated solid solutions for immiscible systems such as Cu-Ta [148-149] and Cu-Nb [150,121,140] and then annealing as-milled alloy powders at certain temperatures for a period of time to allow the homogeneous precipitation of small Ta and Nb particles. Moreover, an alternative way to produce nanostructured Cu matrix composite powder particles with a dispersion of in-situ formed second phase nanoparticles is a solid state reaction method which produces second phase nanoparticles in the Cu matrix through the reaction between additive elements during HEMM and annealing of as-milled powders [144,146]. Apart from these two methods, HEMM of a mixture of second phase nanoparticles and Cu powders could be the simplest way to introduce second phase nanoparticles externally into Cu to produce the nanostructured Cu matrix composite powder particles without any subsequent thermal processing.

1.5.3 Consolidation of Nanostructured Cu Matrix Composite Powder Particles

It is known that consolidation of nanostructured DS metal powder particles into useful bulk engineering components can be achieved by various techniques such as spark plasma sintering (SPS) [151], HIP [152], hot pressing [153], sinter forging [154] and hot extrusion [155-156]. In some cases, two or three such consolidation techniques are combined to complete the consolidation [157]. The technique adopted to consolidate nanostructured powder particles largely depends on the characteristics of the powder particles, and is generally chosen to limit the grain growth as much as possible during consolidation. For instance, SPS method may be the first choice to be used to consolidate nanometer sized powder particles so as to avoid the significant coarsening of the nanostructure of powder particles, as this consolidation technique can finish the consolidation process at relatively low temperatures and within a short time [154,151]. The extremely high activity of nanometer sized particles makes them very difficult to

process with conventional consolidation methods such as HIP plus hot extrusion. This traditional consolidation method in powder metallurgy usually requires both a high temperature and long time which is a very high risk for retaining fine structures of powder particles after consolidation. Nevertheless, nanostructured and micrometer sized powder particles with a dispersion of second phase nanoparticles prepared by HEMM are able to be consolidated using this conventional method. For this kind of powder particles, high temperature consolidation processes only result in a limited extent of coarsening in the microstructure of the matrix due to the retardation effect of second phase nanoparticles. Thus, an UFS metal matrix composite can be easily produced by using the suppression of second phase nanoparticles on the grain growth of the metal matrix via the Zener mechanism.

1.5.4 Mechanical and Electrical Properties of Bulk UFG Cu Matrix Composites

Previous studies have clearly revealed that the microstructure and mechanical properties of UFG metals dispersed with second phase nanoparticles are closely associated with the particle size [158], volume fraction [159-160] and distribution in the matrix [95]. Of course, the fabrication effect should be taken into account as well in terms of discussing the relationship between the microstructure and property of second phase nanoparticle DS UFG metals. Figure 1.5 summarizes the mechanical data published on the UFG Cu matrix composites.

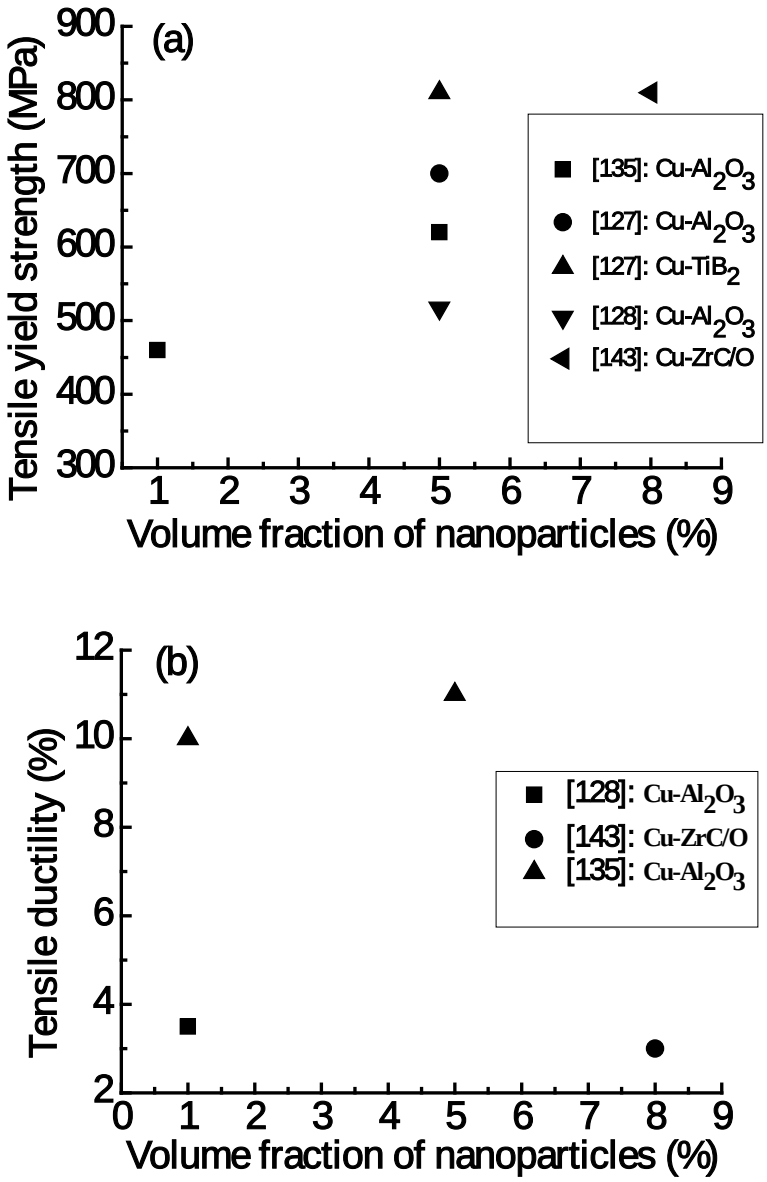

Figure 1.5: Tensile yield strength (a) and ductility (b) of ultrafine structured Cu matrix composites.

It is apparent that UFG Cu matrix composites offer very high tensile yield strengths which are almost 3~6 times that of CG Cu (~150 MPa) (Figure 1.5(a)). This high yield strength observed in the experiments for UFG Cu with a fine dispersion of nanoparticles is primarily ascribed to grain size strengthening through the Hall-Petch relationship and nanoparticle dispersion strengthening associated with the Orowan mechanism. On the other hand, tensile ductility of such materials shown in Figure 1.5(b) exhibit a much lower value in the range of 3-12% compared with that of

conventional copper (~40%). This significant decrease in ductility of DS systems is mainly attributed to the poor ability to relax the stress concentration resulting from grain refinement. In other words, UFG grains in DS materials have low capacity in accumulating dislocations during plastic deformation. The data presented in Figure 1.5 implies that the tensile properties of UFG Cu matrix composites are highly related to various microstructural parameters such as mean nanoparticle size and volume fraction of nanoparticles, mean grain size and fabrication method. Although the role of grain size distribution of the matrix is excluded here, one should realize its importance, especially in ductility. If we put these structural parameters away, the key point in determining the tensile results of UFG metal matrix composites is the direct interaction between dislocations and nanoparticles. For a given quantity of second phase nanoparticles, the tensile strength and ductility of UFG metal matrix composites would be significantly enhanced if this direct interaction is improved. Creating intragranular nanoparticles as much as possible is a very effective way to increase this interaction [95].

Electrical conductivity of UFG Cu matrix composites is another very important property. For some applications like spot welding, both high temperature strength and good conductivity are required simultaneously. Figure 1.6 presents room temperature electrical conductivities of coarse grained and UFG Cu matrix nanocomposites. It is seen that second phase nanoparticles slightly degrade the electrical conductivity of conventional copper, as given by the solid circle symbol shown in Figure 1.6 [161]. However, UFG copper matrix reinforced by second phase nanoparticles shown in Figure 1.6 have electrical conductivity values of less than 55%IACS. It has been shown that the electrical conductivity of a metal is very sensitive to the lattice distortion caused by alloying elements [126] and grain boundaries [143]. These two structural defects can greatly reduce the mean free path of electrons and increase the probability of the electron scattering and thus decrease the electrical conductivity of the metal. Hence, the much lower electrical conductivity observed for UFG Cu dispersed with nanoparticles relative to the coarse grained Cu matrix nanocomposites

is mainly due to the presence of large volume fraction of grain boundaries (solid triangle symbol shown in Figure 1.6). The electrical conductivity of UFG Cu matrix composites will be further reduced if the impurity is introduced during the fabrication process like HEMM (squares shown in Figure 1.6).

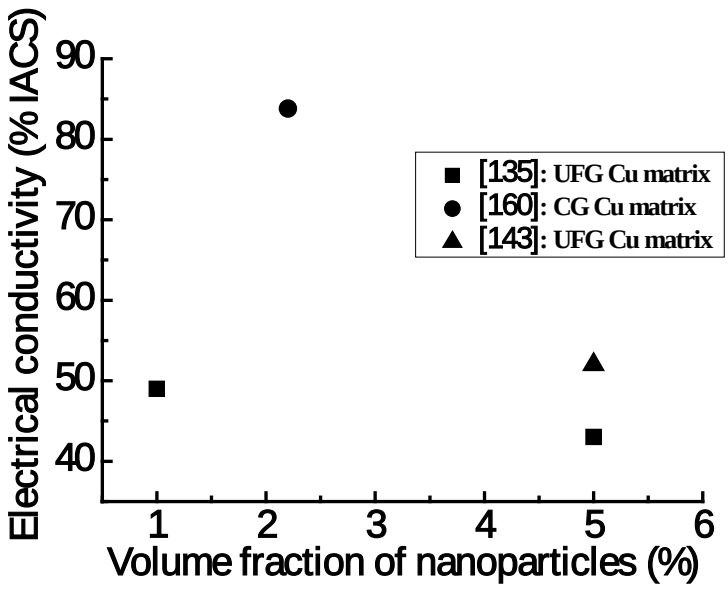

Figure 1.6: Electrical conductivities of coarse grained and ultrafine structured Cu matrix composites.

Based on the literature survey, it has been found that so far much effort has been made on the fabrication of UFS metal matrix nanocomposites (MMNCs) through nanostructured metal matrix nanocomposite (MMNC) powders. However, a systematic and comprehensive investigation of thermal stability of the nanostructured MMNC powder particles and the influence of the consolidation temperature on the microstructures and tensile properties of bulk UFS MMNCs has not yet been found. Such fundamental studies can allow us to understand how the microstructure of nanostructured MMNCs reacts to the annealing temperature which could give some very important information for us to optimize the subsequent consolidation process and to establish a relationship of processing, microstructure and mechanical property of the UFS MMNCs. Combining this information with proper heat treatment, an UFS copper matrix nanocomposite sample with a high strength and good conductivity is

expected to be produced.

1.6 Objectives of This Study

This PhD project has three goals to achieve. Firstly, get a fundamental understanding of the grain growth kinetics of the nanostructured metal matrix composites prepared by HEMM; secondly, establish an extrusion temperature dependence of the microstructural evolution and tensile properties of UFS metal matrix composites, extruded from powder compacts of milled nanostructured metal matrix composite powder particles; last but not least, obtain a preliminary understanding of strengthening mechanisms of UFS metal matrix composites. These three aims in the present study are examined and investigated based on a model system of nanostructured Cu-5vol.%Al_2O_3 composite powder particles prepared by HEMM.

1.7 References

1. Benjamin JS (1970) Dispersion strengthened superalloys by mechanical alloying. Metallurgical Transactions 1 (10):2943-2951
2. Luton M, Jayanth C, Disko M, Matras S, Vallone J Cryomilling of nano-phase dispersion strengthened aluminum. In: Mat. Res. Soc. Symp. Proc, 1989. Cambridge Univ Press, pp 79-86
3. Gleiter H (1989) Nanocrystalline materials. Progress in Materials Science 33 (4):223-315
4. Hall EO (1951) The deformation and ageing of mild steel: III discussion of results. Proceedings of the Physical Society Section B 64 (9):747-752
5. Petch N (1953) The cleavage strength of polycrystals. Journal of Iron Steel Institute 174:25-28
6. Fecht HJ (1990) Intrinsic instability and entropy stabilization of grain boundaries. Physical Review Letters 65 (5):610-613
7. Fecht H, Hellstern E, Fu Z, Johnson W (1990) Nanocrystalline metals prepared by high-energy ball milling. Metallurgical Transactions A 21 (9):2333-2337
8. Huang B, Vallone J, Klein C, Luton M In-Situ Synthesis of Particle Dispersed Nanocrystalline NiAl by Cryomilling. In: MRS Proceedings, 1992. Cambridge Univ Press, pp 171-176
9. Kumar K, Van Swygenhoven H, Suresh S (2003) Mechanical behavior of nanocrystalline metals and alloys. Acta Materialia 51 (19):5743-5774

10. Dao M, Lu L, Asaro R, De Hosson JTM, Ma E (2007) Toward a quantitative understanding of mechanical behavior of nanocrystalline metals. Acta Materialia 55 (12):4041-4065
11. Meyers MA, Mishra A, Benson DJ (2006) Mechanical properties of nanocrystalline materials. Progress in Materials Science 51 (4):427-556
12. Rupert T, Gianola D, Gan Y, Hemker K (2009) Experimental observations of stress-driven grain boundary migration. Science 326 (5960):1686-1690
13. Ma E (2003) Instabilities and ductility of nanocrystalline and ultrafine-grained metals. Scripta Materialia 49 (7):663-668
14. Koch CC (2003) Optimization of strength and ductility in nanocrystalline and ultrafine grained metals. Scripta Materialia 49 (7):657-662
15. Chookajorn T, Murdoch HA, Schuh CA (2012) Design of stable nanocrystalline alloys. Science 337 (6097):951-954
16. Chen J, Lu L, Lu K (2006) Hardness and strain rate sensitivity of nanocrystalline Cu. Scripta materialia 54 (11):1913-1918
17. Hayashi K, Eto H (1989) Pressure-Sintering of Iron, Cobalt, Nickel and Copper Ultrafine Powders and the Crystal Grain Size and Hardness of the Compacts. Journal of the Japan Institute of Metals 53 (2):221-226
18. Zhilyaev A, Swaminathan S, Gimazov A, McNelley T, Langdon T (2008) An evaluation of microstructure and microhardness in copper subjected to ultra-high strains. Journal of Materials Science 43 (23-24):7451-7456
19. Khan AS, Farrokh B, Takacs L (2008) Compressive properties of Cu with different grain sizes: sub-micron to nanometer realm. Journal of Materials Science 43 (9):3305-3313
20. Suryanarayanan Iyer R, Frey CA, Sastry S, Waller B, Buhro W (1999) Plastic deformation of nanocrystalline Cu and Cu–0.2 wt.% B. Materials Science and Engineering: A 264 (1):210-214
21. Haouaoui M, Karaman I, Harwig K, Maier H (2004) Microstructure evolution and mechanical behavior of bulk copper obtained by consolidation of micro-and nanopowders using equal-channel angular extrusion. Metallurgical and Materials Transactions A 35 (9):2935-2949
22. Jiang H, Zhu YT, Butt DP, Alexandrov IV, Lowe TC (2000) Microstructural evolution, microhardness and thermal stability of HPT-processed Cu. Materials Science and Engineering: A 290 (1):128-138
23. Sanders P, Eastman J, Weertman J (1997) Elastic and tensile behavior of nanocrystalline copper and palladium. Acta Materialia 45 (10):4019-4025
24. Youssef KM, Scattergood RO, Linga Murty K, Koch CC (2004) Ultratough nanocrystalline copper with a narrow grain size distribution. Applied Physics Letters 85 (6):929-931
25. Knapp J, Follstaedt D (2004) Hall–Petch relationship in pulsed-laser deposited nickel films. Journal of Materials Research 19 (01):218-227
26. Schuh C, Nieh T, Iwasaki H (2003) The effect of solid solution W additions on the mechanical properties of nanocrystalline Ni. Acta Materialia 51 (2):431-443
27. Mohamed FA, Yang H (2010) Deformation mechanisms in nanocrystalline

materials. Metallurgical and Materials Transactions A 41 (4):823-837
28. Yamakov V, Wolf D, Phillpot S, Mukherjee A, Gleiter H (2003) Deformation-mechanism map for nanocrystalline metals by molecular-dynamics simulation. Nature Materials 3 (1):43-47
29. Wolf D, Yamakov V, Phillpot S, Mukherjee A, Gleiter H (2005) Deformation of nanocrystalline materials by molecular-dynamics simulation: relationship to experiments? Acta Materialia 53 (1):1-40
30. Yamakov V, Wolf D, Phillpot S, Mukherjee A, Gleiter H (2003) Deformation mechanism crossover and mechanical behaviour in nanocrystalline materials. Philosophical Magazine Letters 83 (6):385-393
31. Van Swygenhoven H, Weertman JR (2006) Deformation in nanocrystalline metals. Materials Today 9 (5):24-31
32. Budrovic Z, Van Swygenhoven H, Derlet PM, Van Petegem S, Schmitt B (2004) Plastic deformation with reversible peak broadening in nanocrystalline nickel. Science 304 (5668):273-276
33. Kim H, Estrin Y, Bush M (2000) Plastic deformation behaviour of fine-grained materials. Acta Materialia 48 (2):493-504
34. Shan Z, Stach E, Wiezorek J, Knapp J, Follstaedt D, Mao S (2004) Grain boundary-mediated plasticity in nanocrystalline nickel. Science 305 (5684):654-657
35. Wang Y, Cheng S, Wei Q, Ma E, Nieh T, Hamza A (2004) Effects of annealing and impurities on tensile properties of electrodeposited nanocrystalline Ni. Scripta Materialia 51 (11):1023-1028
36. Zhang X, Fujita T, Pan D, Yu J, Sakurai T, Chen M (2010) Influences of grain size and grain boundary segregation on mechanical behavior of nanocrystalline Ni. Materials Science and Engineering: A 527 (9):2297-2304
37. Vo NQ, Averback RS, Bellon P, Caro A (2008) Limits of hardness at the nanoscale: Molecular dynamics simulations. Physical Review B 78 (24):241402
38. Rupert TJ, Trelewicz JR, Schuh CA (2012) Grain boundary relaxation strengthening of nanocrystalline Ni-W alloys. Journal of Materials Research 27 (9):1285-1294
39. Bringa EM, Caro A, Wang Y, Victoria M, McNaney JM, Remington BA, Smith RF, Torralva BR, Van Swygenhoven H (2005) Ultrahigh strength in nanocrystalline materials under shock loading. Science 309 (5742):1838-1841
40. Ozerinc S, Tai K, Vo NQ, Bellon P, Averback RS, King WP (2012) Grain boundary doping strengthens nanocrystalline copper alloys. Scripta Materialia 67 (7-8):720-723
41. Vo N, Schäfer J, Averback R, Albe K, Ashkenazy Y, Bellon P (2011) Reaching theoretical strengths in nanocrystalline Cu by grain boundary doping. Scripta Materialia 65 (8):660-663
42. Millett PC, Selvam RP, Saxena A (2006) Improving grain boundary sliding resistance with segregated dopants. Materials Science and Engineering: A 431 (1):92-99
43. Rajgarhia RK, Spearot DE, Saxena A (2010) Plastic deformation of nanocrystalline copper-antimony alloys. Journal of Materials Research 25

(03):411-421
44. Rajgarhia RK, Spearot DE, Saxena A (2010) Molecular Dynamics Simulations of Dislocation Activity in Single-Crystal and Nanocrystalline Copper Doped with Antimony. Metallurgical and Materials Transactions A 41 (4):854-860
45. Dobosz R, Lewandowska M, Kurzydlowski KJ (2012) FEM modelling of the combined effect of grain boundaries and second phase particles on the flow stress of nanocrystalline metals. Computational Materials Science 53 (1):286-293
46. Ozerinc S, Tai K, Vo NQ, Bellon P, Averback RS, King WP (2012) Grain boundary doping strengthens nanocrystalline copper alloys. Scripta materialia
47. Giga A, Kimoto Y, Takigawa Y, Higashi K (2006) Demonstration of an inverse Hall–Petch relationship in electrodeposited nanocrystalline Ni–W alloys through tensile testing. Scripta Materialia 55 (2):143-146
48. Matsui I, Takigawa Y, Uesugi T, Higashi K (2013) Effect of additives on tensile properties of bulk nanocrystalline Ni–W alloys electrodeposited from a sulfamate bath. Materials Letters 99:65-67
49. Youssef K, Sakaliyska M, Bahmanpour H, Scattergood R, Koch C (2011) Effect of stacking fault energy on mechanical behavior of bulk nanocrystalline Cu and Cu alloys. Acta Materialia 59 (14):5758-5764
50. Vinogradov A, Ishida T, Kitagawa K, Kopylov V (2005) Effect of strain path on structure and mechanical behavior of ultra-fine grain Cu–Cr alloy produced by equal-channel angular pressing. Acta Materialia 53 (8):2181-2192
51. Li H, Ebrahimi F, Choo H, Liaw PK (2006) Grain size dependence of tensile behavior in nanocrystalline Ni–Fe alloys. Journal of Materials Science 41 (22):7636-7642
52. Karimpoor A, Erb U, Aust K, Palumbo G (2003) High strength nanocrystalline cobalt with high tensile ductility. Scripta Materialia 49 (7):651-656
53. Gu C, Lian J, Jiang Z (2006) High Strength Nanocrystalline Ni–Co Alloy with Enhanced Tensile Ductility. Advanced Engineering Materials 8 (4):252-256
54. Tellkamp V, Lavernia EJ, Melmed A (2001) Mechanical behavior and microstructure of a thermally stable bulk nanostructured Al alloy. Metallurgical and Materials Transactions A 32 (9):2335-2343
55. Guduru RK, Darling KA, Scattergood RO, Koch CC, Murty K (2007) Mechanical properties of electrodeposited nanocrystalline copper using tensile and shear punch tests. Journal of Materials Science 42 (14):5581-5588
56. Ebrahimi F, Bourne G, Kelly MS, Matthews T (1999) Mechanical properties of nanocrystalline nickel produced by electrodeposition. Nanostructured Materials 11 (3):343-350
57. Yu C, Sun P, Kao P, Chang C (2005) Mechanical properties of submicron-grained aluminum. Scripta Materialia 52 (5):359-363
58. Legros M, Elliott B, Rittner M, Weertman J, Hemker K (2000) Microsample tensile testing of nanocrystalline metals. Philosophical magazine A 80 (4):1017-1026
59. Thein MA, Gupta M (2003) Microstructural, physical, and mechanical characteristics of bulk nanocrystalline copper synthesised using powder metallurgy. Materials Science and Technology 19 (11):1473-1477

60. Youssef K, Scattergood R, Murty K, Koch C (2006) Nanocrystalline Al–Mg alloy with ultrahigh strength and good ductility. Scripta Materialia 54 (2):251-256
61. Dalla Torre F, Van Swygenhoven H, Victoria M (2002) Nanocrystalline electrodeposited Ni: microstructure and tensile properties. Acta Materialia 50 (15):3957-3970
62. Pachla W, Kulczyk M, Sus-Ryszkowska M, Mazur A, Kurzydlowski KJ (2008) Nanocrystalline titanium produced by hydrostatic extrusion. Journal of Materials Processing Technology 205 (1):173-182
63. Stolyarov VV, Zhu YT, Alexandrov IV, Lowe TC, Valiev RZ (2001) Influence of ECAP routes on the microstructure and properties of pure Ti. Materials Science and Engineering: A 299 (1):59-67
64. Valiev R, Alexandrov I, Zhu Y, Lowe T (2002) Paradox of Strength and Ductility in Metals Processed Bysevere Plastic Deformation. Journal of Materials Research 17 (01):5-8
65. Mukai T, Suresh S, Kita K, Sasaki H, Kobayashi N, Higashi K, Inoue A (2003) Nanostructured Al–Fe alloys produced by e-beam deposition: static and dynamic tensile properties. Acta Materialia 51 (14):4197-4208
66. Zhang H, Jiang Z, Lian J, Jiang Q (2008) Strain rate dependence of tensile ductility in an electrodeposited Cu with ultrafine grain size. Materials Science and Engineering: A 479 (1):136-141
67. Wu X, Du L, Zhang H, Liu J, Zhou Y, Li Z, Xiong L, Bai Y (1999) Synthesis and tensile property of nanocrystalline metal copper. Nanostructured Materials 12 (1):221-224
68. Chen X, Lu J, Lu L, Lu K (2005) Tensile properties of a nanocrystalline 316L austenitic stainless steel. Scripta Materialia 52 (10):1039-1044
69. Cheng S, Ma E, Wang Y, Kecskes L, Youssef K, Koch C, Trociewitz U, Han K (2005) Tensile properties of in situ consolidated nanocrystalline Cu. Acta Materialia 53 (5):1521-1533
70. Merz M, Dahlgren S (1975) Tensile strength and work hardening of ultrafine-grained high-purity copper. Journal of Applied Physics 46 (8):3235-3237
71. Dobatkin S, Szpunar J, Zhilyaev A, Cho J-Y, Kuznetsov A (2007) Effect of the route and strain of equal-channel angular pressing on structure and properties of oxygen-free copper. Materials Science and Engineering: A 462 (1):132-138
72. Kulczyk M, Pachla W, Mazur A, Suś-Ryszkowska M, Krasilnikov N, Kurzydłowski K (2007) Producing bulk nanocrystalline materials by combined hydrostatic extrusion and equal-channel angular pressing. Materials Science 25 (4):991-999
73. Wen H, Zhao Y, Topping TD, Ashford D, Figueiredo RB, Xu C, Langdon TG, Lavernia EJ (2012) Influence of Pressing Temperature on Microstructure Evolution and Mechanical Behavior of Ultrafine-Grained Cu Processed by Equal-Channel Angular Pressing. Advanced Engineering Materials 14 (3):185-194
74. Dalla Torre F, Lapovok R, Sandlin J, Thomson P, Davies C, Pereloma E (2004) Microstructures and properties of copper processed by equal channel angular extrusion for 1–16 passes. Acta Materialia 52 (16):4819-4832

75. Koch CC (2002) Ductility in nanostructured and ultra fine-grained materials: Recent evidence for optimism. Journal of Metastable and Nanocrystalline Materials 18:9-20
76. Ma E (2006) Eight routes to improve the tensile ductility of bulk nanostructured metals and alloys. JOM 58 (4):49-53
77. Ovid'ko I, Langdon T (2012) Enhanced ductility of nanocrystalline and ultrafine-grained metals. Reviews on Advanced Materials Science 30 (2):103-111
78. Ma E (2005) Four approaches to improve the tensile ductility of high-strength nanocrystalline metals. Journal of Materials Engineering and Performance 14 (4):430-434
79. Wang Y, Ott R, Van Buuren T, Willey T, Biener M, Hamza A (2012) Controlling factors in tensile deformation of nanocrystalline cobalt and nickel. Physical Review B 85 (1):014101
80. Zhao Y, Zhu Y, Lavernia EJ (2010) Strategies for improving tensile ductility of bulk nanostructured materials. Advanced Engineering Materials 12 (8):769-778
81. Sharon JA, Padilla HAI, Boyce BL (2013) Interpreting the ductility of nanocrystalline metals. Journal of Materials Research 28 (12):1539-1552
82. Koch CC, Youssef KM, Scattergood RO, Murty KL (2005) Breakthroughs in optimization of mechanical properties of nanostructured metals and alloys. Advanced Engineering Materials 7 (9):787-794
83. Valiev RZ, Langdon TG (2006) Principles of equal-channel angular pressing as a processing tool for grain refinement. Progress in Materials Science 51 (7):881-981
84. Beyerlein IJ, Tóth LS (2009) Texture evolution in equal-channel angular extrusion. Progress in Materials Science 54 (4):427-510
85. Zhilyaev AP, Langdon TG (2008) Using high-pressure torsion for metal processing: Fundamentals and applications. Progress in Materials Science 53 (6):893-979
86. Wang Y, Chen M, Zhou F, Ma E (2002) High tensile ductility in a nanostructured metal. Nature 419 (6910):912-915
87. Hart E (1967) Theory of the tensile test. Acta Metallurgica 15 (2):351-355
88. Zhao Y, Topping T, Li Y, Lavernia EJ (2011) Strength and Ductility of Bi-Modal Cu. Advanced Engineering Materials 13 (9):865-871
89. Zhao Y, Topping T, Bingert JF, Thornton JJ, Dangelewicz AM, Li Y, Liu W, Zhu Y, Zhou Y, Lavernia EJ (2008) High tensile ductility and strength in bulk nanostructured nickel. Advanced Materials 20 (16):3028-3033
90. Horita Z, Ohashi K, Fujita T, Kaneko K, Langdon TG (2005) Achieving High Strength and High Ductility in Precipitation-Hardened Alloys. Advanced Materials 17 (13):1599-1602
91. Cheng S, Zhao Y, Zhu Y, Ma E (2007) Optimizing the strength and ductility of fine structured 2024 Al alloy by nano-precipitation. Acta Materialia 55 (17):5822-5832
92. Takata N, Ohtake Y, Kita K, Kitagawa K, Tsuji N (2009) Increasing the ductility of ultrafine-grained copper alloy by introducing fine precipitates. Scripta Materialia 60 (7):590-593

93. Hirosawa S, Hamaoka T, Horita Z, Lee S, Matsuda K, Terada D (2013) Methods for Designing Concurrently Strengthened Severely Deformed Age-Hardenable Aluminum Alloys by Ultrafine-Grained and Precipitation Hardenings. Metallurgical and Materials Transactions A:1-13
94. Zhao Y-H, Liao X-Z, Cheng S, Ma E, Zhu YT (2006) Simultaneously increasing the ductility and strength of nanostructured alloys. Advanced Materials 18 (17):2280-2283
95. Liu G, Zhang G, Jiang F, Ding X, Sun Y, Sun J, Ma E (2013) Nanostructured high-strength molybdenum alloys with unprecedented tensile ductility. Nature materials 12 (4):344-350
96. Zhao Y, Liao X, Horita Z, Langdon T, Zhu Y (2008) Determining the optimal stacking fault energy for achieving high ductility in ultrafine-grained Cu–Zn alloys. Materials Science and Engineering: A 493 (1):123-129
97. Zhao Y, Zhu Y, Liao X, Horita Z, Langdon T (2006) Tailoring stacking fault energy for high ductility and high strength in ultrafine grained Cu and its alloy. Applied Physics Letters 89 (12):121906
98. Lu L, Chen X, Huang X, Lu K (2009) Revealing the maximum strength in nanotwinned copper. Science 323 (5914):607-610
99. Lu K, Lu L, Suresh S (2009) Strengthening materials by engineering coherent internal boundaries at the nanoscale. Science 324 (5925):349-352
100. Hutchinson J, Neale K (1977) Influence of strain-rate sensitivity on necking under uniaxial tension. Acta Metallurgica 25 (8):839-846
101. Ghosh A (1977) Tensile instability and necking in materials with strain hardening and strain-rate hardening. Acta Metallurgica 25 (12):1413-1424
102. Wang Y, Ma E (2004) Three strategies to achieve uniform tensile deformation in a nanostructured metal. Acta Materialia 52 (6):1699-1709
103. Champion Y, Langlois C, Guérin-Mailly S, Langlois P, Bonnentien J-L, Hÿtch MJ (2003) Near-perfect elastoplasticity in pure nanocrystalline copper. Science 300 (5617):310-311
104. Humphreys FJ, Hatherly M (2004) Recrystallization and related annealing phenomena. 2 edn. Elseivier Ltd., UK
105. Krill C, Ehrhardt H, Birringer R (2005) Thermodynamic stabilization of nanocrystallinity. Zeitschrift für Metallkunde 96 (10):1134-1141
106. Weissmüller J (1994) Some basic notions on nanostructured solids. Materials Science and Engineering: A 179:102-107
107. Weissrmiller J (1994) Alloy thermodynamics in nanostructures. Journal of Materials Research 9 (1):4-7
108. Wynblatt P, Ku R (1977) Surface energy and solute strain energy effects in surface segregation. Surface Science 65 (2):511-531
109. Wynblatt P, Chatain D (2006) Anisotropy of segregation at grain boundaries and surfaces. Metallurgical and Materials Transactions A 37 (9):2595-2620
110. Darling K, VanLeeuwen B, Semones J, Koch C, Scattergood R, Kecskes L, Mathaudhu S (2011) Stabilized nanocrystalline iron-based alloys: Guiding efforts in alloy selection. Materials Science and Engineering: A 528 (13):4365-4371

111. Darling K, VanLeeuwen B, Koch C, Scattergood R (2010) Thermal stability of nanocrystalline Fe–Zr alloys. Materials Science and Engineering: A 527 (15):3572-3580
112. VanLeeuwen BK, Darling KA, Koch CC, Scattergood RO, Butler BG (2010) Thermal stability of nanocrystalline $Pd_{81}Zr_{19}$. Acta Materialia 58 (12):4292-4297
113. Murdoch HA, Schuh CA (2013) Stability of binary nanocrystalline alloys against grain growth and phase separation. Acta Materialia 61 (6):2121-2132
114. Murdoch HA, Schuh CA (2013) Estimation of grain boundary segregation enthalpy and its role in stable nanocrystalline alloy design. Journal of Materials Research 28(16):2154-2163
115. Koch CC, Scattergood RO, Saber M, Kotan H High temperature stabilization of nanocrystalline grain size: Thermodynamic versus kinetic strategies. Journal of Materials Research 28(13):1785-1791
116. Smith CS (1948) Grains, Phases, and Interfaces an Interpretation of Microstructure. Metals Technology 175: 15-51
117. Manohar P, Ferry M, Chandra T (1998) Five decades of the Zener equation. ISIJ International 38 (9):913-924
118. Manohar P, Ferry M (1999) Grain Growth in Particle-Containing Metastable Microstructures. Journal of Metastable and Nanocrystalline Materials 2:455-462
119. Razavi Tousi S, Rahaei M, Abdi M, Sadrnezhaad S (2010) Stabilization of nanostructured materials using fine inert ceramic particles. Ceramics International 36 (2):793-796
120. Bréchet Y, Militzer M (2005) A note on grain size dependent pinning. Scripta Materialia 52 (12):1299-1303
121. Botcharova E, Freudenberger J, Schultz L (2006) Mechanical and electrical properties of mechanically alloyed nanocrystalline Cu–Nb alloys. Acta Materialia 54 (12):3333-3341
122. Cao P, Lu L, Lai M (2001) Grain growth and kinetics for nanocrystalline magnesium alloy produced by mechanical alloying. Materials Research Bulletin 36 (5):981-988
123. Perez R, Huang B, Lavernia E (1996) Thermal stability of nanocrystalline Fe-10 wt.% Al produced by cryogenic mechanical alloying. Nanostructured Materials 7 (5):565-572
124. Groza J (1992) Heat-resistant dispersion-strengthened copper alloys. Journal of Materials Engineering and Performance 1 (1):113-121
125. Schroth JG, Franetovic MV (1989) Mechanical alloying for heat-resistant copper alloys. JOM 41 (1):37-39
126. Ghosh G, Miyake J, Fine M (1997) The systems-based design of high-strength, high-conductivity alloys. JOM 49 (3):56-60
127. Groza J, Gibeling J (1993) Principles of particle selection for dispersion-strengthened copper. Materials Science and Engineering: A 171 (1):115-125
128. Biselli C, Morris D, Randall N (1994) Mechanical alloying of high-strength copper alloys containing TiB_2 and Al_2O_3 dispersoid particles. Scripta Metallurgica 30

(10):1327-1332
129. Ďurišin J, Orolínová M, Ďurišinová K (2005) Nanocrystalline Cu-5vol.% γ-Al_2O_3 material. Powder Metallurgy Progress 5 (1):37-49
130. Hahn SI, Hwang SJ (2009) Estimate of the Hall-Petch and Orowan effects in the nanocrystalline Cu with Al_2O_3 dispersoid. Journal of Alloys and Compounds 483 (1):207-208
131. Hwang SJ (2011) Compressive yield strength of the nanocrystalline Cu with Al_2O_3 dispersoid. Journal of Alloys and Compounds 509 (5):2355-2359
132. Kudashov D, Baum H, Martin U, Heilmaier M, Oettel H (2004) Microstructure and room temperature hardening of ultra-fine-grained oxide-dispersion strengthened copper prepared by cryomilling. Materials Science and Engineering: A 387:768-771
133. Lee DW, Ha GH, Kim BK (2001) Synthesis of Cu-Al_2O_3 nanocomposite powder. Scripta Materialia 44 (8):2137-2140
134. Lee DW, Kim BK (2004) Nanostructured Cu-Al_2O_3 composite produced by thermochemical process for electrode application. Materials Letters 58 (3):378-383
135. Mukhtar A, Zhang D, Kong C, Munroe P (2010) Consolidation of ultrafine-grained Cu powder and nanostructured Cu-(2.5-10) vol% Al_2O_3 composite powders by powder compact forging. Journal of Materials Science 45 (17):4594-4605
136. Nachum S, Fleck NA, Ashby MF, Colella A, Matteazzi P (2010) The microstructural basis for the mechanical properties and electrical resistivity of nanocrystalline Cu-Al_2O_3. Materials Science and Engineering: A 527 (20):5065-5071
137. Need RF, Alexander DJ, Field RD, Livescu V, Papin P, Swenson CA, Mutnick D (2012) The effects of equal channel angular extrusion on the mechanical and electrical properties of alumina dispersion-strengthened copper alloys. Materials Science and Engineering: A 565:450-458
138. Stobrawa J, Rdzawski Z (2006) Deformation behaviour of dispersion hardened nanocrystalline copper. Journal of Achievements in Materials and Manufacturing Engineering 17(1-2):153-156
139. Stobrawa J, Rdzawski Z (2007) Dispersion–strengthened nanocrystalline copper. Journal of Achievements in Materials and Manufacturing Engineering 24 (2):35-42
140. Morris MA, Morris DG (1989) Microstructural refinement and associated strength of copper alloys obtained by mechanical alloying. Materials Science and Engineering: A 111:115-127
141. Schilling WF, Grant NJ (1970) Oxide dispersed copper alloys by surface oxidation. Metallurgical Transactions 1 (8):2205-2210
142. Anđić ZM, Korać M, Kamberović Z, Vujović AČ, Tasić M (2007)Analysis of the properties of a Cu-Al_2O_3 sintered system based on ultra fine and nanocomposite powders. Science of Sintering 39 (2):145-152
143. Sudharshan Phani P, Vishnukanthan V, Sundararajan G (2007) Effect of heat treatment on properties of cold sprayed nanocrystalline copper alumina coatings. Acta Materialia 55 (14):4741-4751
144. Morris DG, Morris MA (1991) Microstructure and strength of nanocrystalline copper alloy prepared by mechanical alloying. Acta Metallurgica 39 (8):1763-1770
145. Rajkovic V, Bozic D, Jovanovic MT (2008) Properties of copper matrix

reinforced with various size and amount of Al_2O_3 particles. Journal of Materials Processing Technology 200 (1):106-114
146. Ying D, Zhang D (2000) Processing of Cu–Al_2O_3 metal matrix nanocomposite materials by using high energy ball milling. Materials Science and Engineering: A 286 (1):152-156
147. Zhang DL, Richmond JJ (1999) Microstructural evolution during combustion reaction between CuO and Al induced by high energy ball milling. Journal of Materials Science 34 (4):701-706
148. Venugopal T, Prasad Rao K, Murty B (2007) Mechanical and electrical properties of Cu–Ta nanocomposites prepared by high-energy ball milling. Acta Materialia 55 (13):4439-4445
149. Darling KA, Roberts AJ, Mishin Y, Mathaudhu SN, Kecskes LJ (2013) Grain Size Stabilization of Nanocrystalline Copper at High Temperatures by Alloying with Tantalum. Journal of Alloys and Compounds 573:142-150
150. Botcharova E, Heilmaier M, Freudenberger J, Drew G, Kudashow D, Martin U, Schultz L (2003) Supersaturated solid solution of niobium in copper by mechanical alloying. Journal of Alloys and Compounds 351 (1):119-125
151. Yar MA, Wahlberg S, Bergqvist H, Salem HG, Johnsson M, Muhammed M (2011) Chemically produced nanostructured ODS–lanthanum oxide–tungsten composites sintered by spark plasma. Journal of Nuclear Materials 408 (2):129-135
152. Liu T, Shen HL, Zhang TW, Zhu M, Qin CG Effects of Consolidation Process on the Microstructure and Mechanical Properties of ODS Ferritic Alloy. In: Materials Science Forum, 2013. Transactions Technology Publication, pp 507-512
153. Dong S, Zhou Y, Chang B, Shi Y (2002) Formation of a TiB_2-reinforced copper-based composite by mechanical alloying and hot pressing. Metallurgical and Materials Transactions A 33 (4):1275-1280
154. Viswanathan V, Laha T, Balani K, Agarwal A, Seal S (2006) Challenges and advances in nanocomposite processing techniques. Materials Science and Engineering: R: Reports 54 (5):121-285
155. Marques MT, Correia JB, Vilar R (2008) Consolidation via hot extrusion of Cu-NbC nanocomposites. Reviews on Advanced Materials Science 18:403-407
156. Zhou DS, Zhang DL, Kong C, Munroe P (2013) Factors Controlling the Tensile Properties of Ultrafine Structured Cu-5vol.% Al_2O_3 Nanocomposite Prepared by High Energy Mechanical Milling and Powder Compact Extrusion. Materials Science and Engineering: A 584:67-72
157. Ukai S, Fujiwara M (2002) Perspective of ODS alloys application in nuclear environments. Journal of Nuclear Materials 307:749-757
158. Poirier D, Drew RA, Trudeau ML, Gauvin R (2010) Fabrication and properties of mechanically milled alumina/aluminum nanocomposites. Materials Science and Engineering: A 527 (29):7605-7614
159. Akbarpour M, Salahi E, Alikhani Hesari F, Kim H, Simchi A (2013) Effect of nanoparticle content on the microstructural and mechanical properties of nano-SiC dispersed bulk ultrafine-grained Cu matrix composites. Materials & Design 52:881-887

160. Kollo L, Bradbury C, Veinthal R, Jäggi C, Carreno-Morelli E, Leparoux M (2011) Nano-silicon carbide reinforced aluminium produced by high-energy milling and hot consolidation. Materials Science and Engineering: A 528 (21):6606-6615
161. Fuschillo N, Gimpl M (1971) Electrical Conductivity and Tensile Strength of Dispersion-Strengthened Copper. Journal of Applied Physics 42 (13):5513-5516

Chapter Two

Materials and Experimental Procedure

Outlined in this chapter are the materials and the experimental procedures used to prepare the nanostructured Cu-5vol.%Al_2O_3 composite powder samples and the consolidated bulk samples from the powder and the techniques employed for analyzing and characterizing the samples during this research work.

2.1 Starting Materials

As starting materials, a Cu powder (99.7% pure, particle sizes: 1~100 µm) and Al_2O_3 nanopowder (99.9% pure, average particle size: 50 nm) supplied by Sigma-Aldrich were used to produce the Cu-5vol.%Al_2O_3 composite powder particles by HEMM and bulk samples by a combination of HEMM and powder compaction extrusion.

2.2 Material Preparation

2.2.1 HEMM

A Retch PM100 planetary ball mill, as shown in Figure 2.1(a), was operated to mill a powder mixture of Cu powder and Al_2O_3 nanopowders at a speed of 400 rpm. A hardened steel vial, as shown in Figure 2.1(b), with a cylindrical cavity of 60 mm in depth and 100 mm in diameter and stainless steel balls with diameters of 12.5 mm and 25 mm (Figure 2.1(b)) were used for the milling operations. The vial which contained stainless steel balls and 100 g (in total) of the Cu powder and Al_2O_3 nanopowder with the nominal composition of Cu-5vol%Al_2O_3 were sealed in a glove box filled with high purity argon, as shown in Figure 2.1(c).

Figure 2.1: (a) Retsch PM100 planetary ball mill; (b) steel vial and stainless steel balls with diameters of 12.5 and 25 mm; (c) glove box.

Before milling, the Cu powder and Al_2O_3 nanopowder were mixed using 61 stainless steel balls of 12.5 mm in diameter for 12 hours with a speed of 100 rpm. Two different HEMM operations were used in this study. The milling step for the research work presented in Chapter 3, 5 and 6 comprised 24 hours (net time) of milling with a break of 30 minutes after every 30 minute interval of milling using 6 stainless steel balls of 25 mm in diameter and 13 stainless steel balls of 12.5 mm in diameter. However, for the research work presented in Chapter 4, the milling process consisted of two steps. In Step 1, the powder mixture was milled for 12 hours (net time) with a break of 30 minutes after every 30 minute interval of milling using 61 stainless steel balls with a diameter of 12.5 mm. In Step 2, the 12 hours milled powder was milled for a further 12 hours (net time) with a break of 30 minutes after every 30 minute interval of milling using 6 stainless steel balls of 25 mm in diameter and 13 stainless steel balls of 12.5 mm in diameter. Between Step 1 and Step 2, the balls were changed in the glove box filled with high purity argon. The ball-to-powder weight ratio was 5:1 for both mixing and milling steps in the different HEMM operations.

2.2.2 Heat Treatment

Heat treatment of the samples was conducted in a stainless steel vacuum tube furnace, as shown in Figure 2.2. The furnace was programmed to heat samples up at a heating rate of 10°C/min and cool samples down with the furnace cooling mode. The application temperature of the furnace is up to 1000°C. The as-milled and extruded bulk samples were annealed at different temperatures in the range of 300-600 and 500-1000°C, respectively for various times with a vacuum of ~10^{-6} mbar.

Figure 2.2: Stainless steel vacuum tube furnace.

2.2.3 Powder Consolidation

A 100-ton hydraulic press, as shown in Figure 2.3, was used to prepare powder compacts for extrusion and carry out the extrusion.

Figure 2.3: 100-ton hydraulic press and induction furnace.

In this study, two different compaction conditions were adopted to press two different milled powders into compacts for the extrusion of Cu-5vol.%Al_2O_3 composite bulk samples. In Chapter 4, the milled Cu-5vol.%Al_2O_3 composite powder particles were uniaxially hot compacted in a H13 steel die with a cylindrical cavity of 25 mm in

diameter at 350°C for 20 minutes under a pressure of 300 MPa. The die was lubricated with graphite gel. While the milled powder particles in Chapter 5 and 6 were compacted at room temperature with a pressure of ~2 GPa without any holding time. All Cu-5vol.%Al_2O_3 composite compacts were ground to remove the thin layer of graphite on the surface of the compact prior to performing the extrusion. The Cu-5vol.%Al_2O_3 composite compacts, having a shallow hole for a thermocouple to measure the temperature of the compact, were then enclosed in the hydraulic press chamber with argon atmosphere and heated from room temperature to extrusion temperature in the range of 300-900°C by using induction furnace, as shown in Figure 2.3. An extrusion ratio of 10:1 was used to produce Cu-5vol.%Al_2O_3 composite rods. A complete flow chart for the production of Cu-5vol.%Al_2O_3 composite bulk samples is presented in Figure 2.4.

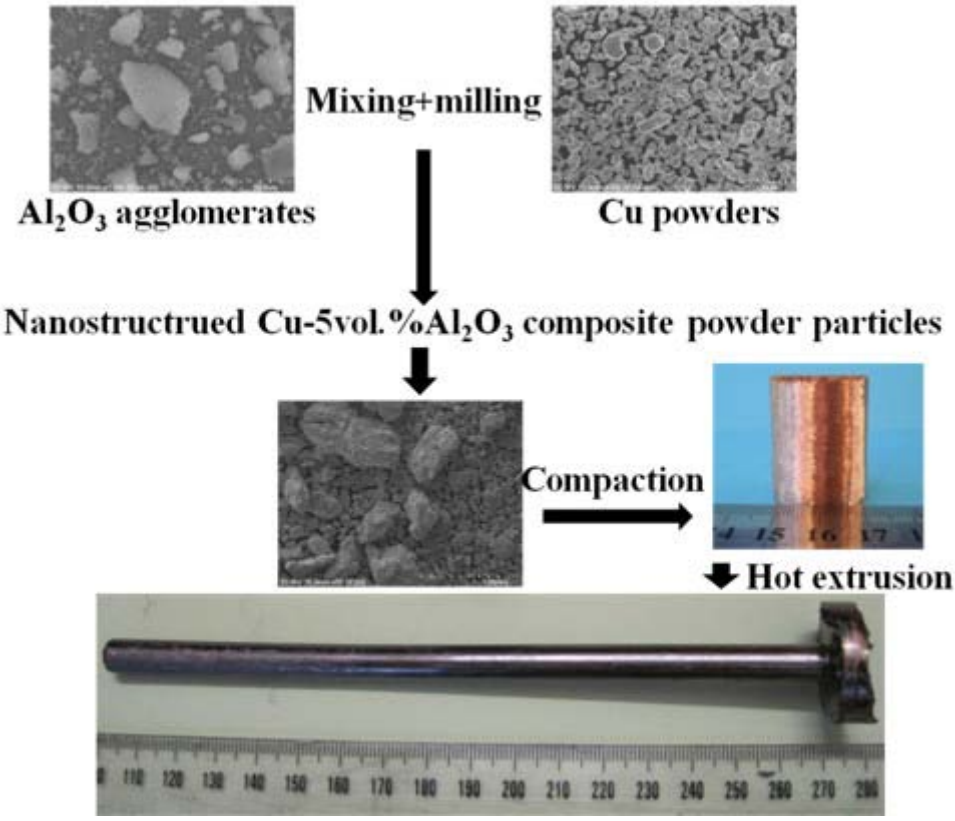

Figure 2.4: A flow chart of the preparation of Cu-5vol.%Al_2O_3 composite rods using milled composite powder particles.

2.3 Microstructural Characterization

2.3.1 Sample Preparation

The as-milled annealed powder particles, and as-extruded or annealed extruded bulk samples were cold mounted in epoxy resin and hardened for 24 hours. The resin cylinder was carefully ground using NO.600, 1000, 2000 and 4000 SiC paper with running tap water to reveal the cross section of the samples, followed by polishing using Al_2O_3 suspension with a particle size of 0.3 µm. The sample was thoroughly rinsed with distilled water to remove any Al_2O_3 particles from the suspension left on the surface. The polished "mirror" of each sample was made parallel to the bottom surface of the mount, so that an even height was made for the hardness measurement, X-ray diffraction (XRD) analysis and microscopy examination.

2.3.2 XRD

XRD characterization of powder particle and bulk samples was conducted using a Philips X-pert XRD system with Cu Kα radiation (λ=0.15406 nm) and a graphite monochromator. The working voltage and current of the XRD system were 40 kV and 40 mA, respectively. The XRD patterns of samples were obtained by scanning using a step size of 0.02^o and a time of 2s per step. The scanning range for the XRD patterns collected was $12\text{-}100^o$.

2.3.3 Scanning Electron Microscopy (SEM)

Microstructural characterization of as-milled and annealed Cu-5vol.%Al_2O_3 composite powder particles and as-extruded and annealed extruded samples was carried out using a Hitachi S4700 SEM with an operating voltage of 20 kV. In addition to secondary electron (SE) analysis, backscattered electron (BSE) analysis on samples was also performed.

2.3.4 Transmission Electron Microscopy (TEM) and Scanning Transmission Electron Microscopy (STEM)

Specimens for TEM analysis were made in a FEI Nova xT Nanolab 200 dual beam focused ion beam (FIB) microscope. Thin foils with a thickness of about 50 nm were cut from the mounted samples with a Ga ion beam operating at 30 kV, and were retrieved out of the vacuum chamber using a Kleindiek ex-situ nanomanipulator, and then deposited onto a standard 150 mesh Au grid covered with a carbon film. A Philips CM200 FEG TEM equipped with an energy dispersive X-ray spectroscopy (EDX) system operating at 200 kV was used for both microstructural and compositional analysis. A weak beam current was selected to stabilize the microstructure and avoid over heating the sensitive crystal structure. The TEM specimens were prepared and characterized in the Electron Microscopy Unit, University of New South Wales, Sydney, Australia.

2.3.5 Microhardness Measurements

The microhardness was measured using a digital Vickers microindentation tester, LECO LM700, with a load of 25/50 gf and a dwell time of 15 s for powder particle/bulk samples. Ten indents for each sample were made to produce an average microhardness measurement.

2.3.6 Tensile Testing

Tensile test specimens, as shown in Figure 2.5, were cut from the extruded Cu-5vol.%Al_2O_3 composite rods using electric discharge machining (EDM) wire cutter (DK77 series). The dog-bone shaped tensile test specimens had a gauge length of 20 mm and a rectangular cross-section of 2 mm in thickness and 2 mm in width. The tensile testing of specimens was carried out at room temperature using an Instron 4204 testing machine with a maximum load of 5 kN and at a crosshead speed of 0.12 mm/min which was equivalent to a strain rate of 1×10^{-4} /s. All reported tensile data presented in this research work was the average of three test results.

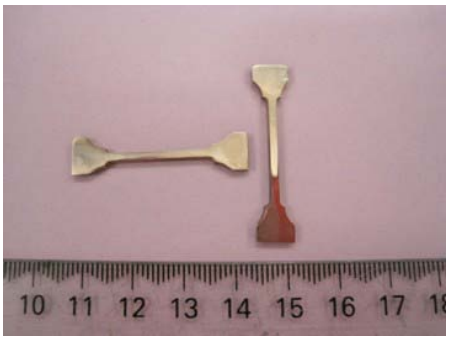

Figure 2.5: Tensile specimens cut from extruded Cu-5vol.%Al_2O_3 composite rods.

Chapter Three

Thermal Stability of the Nanostructure of Mechanically Milled Cu-5vol.%Al_2O_3 Nanocomposite Powder Particles

3.1 Introduction

It has been widely accepted that the consolidation of nanostructured powders is an effective way of synthesizing bulk nanostructured and ultrafine structured metallic materials and near-net shaped components [1]. For this approach to be used effectively, either or both of two conditions should be satisfied: (1) the time for keeping the nanostructured powder at relatively high temperature (above 0.6 T_m, where T_m is the melting temperature of the metal in Kelvin) during consolidation should be sufficiently short, being in the order of minutes rather than hours; and (2) the thermal stability of the nanostructure of the powder particles is sufficiently high to allow the nanostructure to coarsen by only a small amount at relatively high temperatures. The first condition can possibly be satisfied if the powder is consolidated using processes which involve pressure and/or a large amount of plastic flow. Such processes include in-situ consolidation of powder particles by high energy mechanical milling [2-3], powder compact forging [4], powder compact extrusion[5], and spark plasma sintering [6]. When such processes are not able to produce well consolidated materials or are not cost-effective, it is necessary to improve the thermal stability of the nanostructure of the powder particles.

As reviewed in Chapter One, many nanostructured materials stabilized by fine second phase particles have been reported, but a systematic investigation of the grain growth behavior and kinetics of such nanostructures is still missing. The present study is to contribute to this body of academic work by systematically investigating the grain

growth of the nanocrystalline Cu matrix and other microstructural changes that occur during annealing of Cu-5vol.%Al_2O_3 nanocomposite powder particles. It is hoped that an in-depth understanding of the thermal stability of the nanostructure of metal matrix nanocomposites can be achieved through the study.

3.2 Results

As shown in Figure 3.1, the Cu peaks of the XRD patterns of the as-milled and annealed Cu-5vol.%Al_2O_3 nanocomposite powders became narrower with increasing annealing temperature, suggesting that the Cu grains grew during annealing.

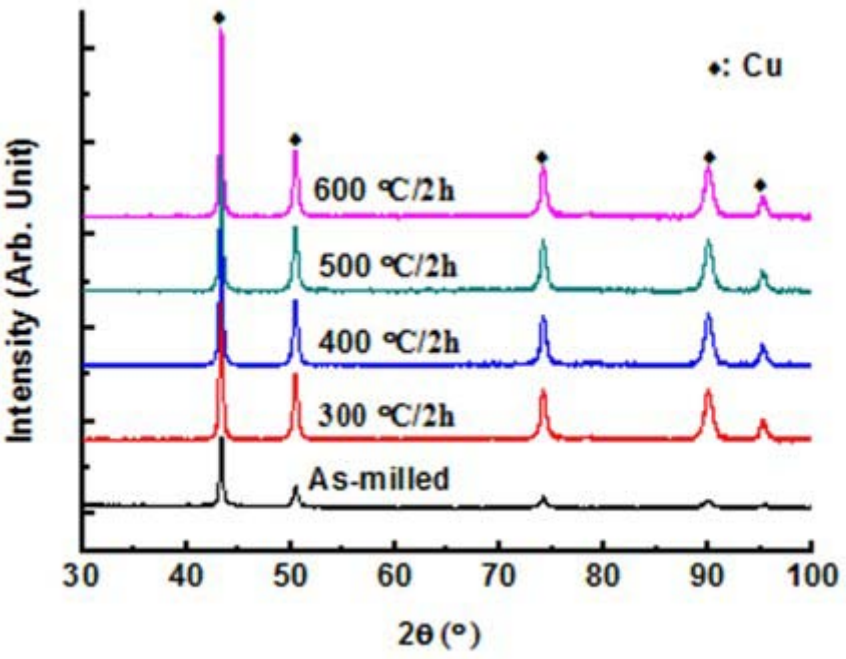

Figure 3.1: XRD patterns of as-milled and annealed nanostructured Cu-5vol.%Al_2O_3 composite powders.

The Cu peaks of the XRD patterns were analyzed to determine the average Cu grain sizes and dislocation densities of the as-milled and annealed powder particles. Prior to doing this, background and $K\alpha_2$ signals were removed from the XRD diffraction peaks, and instrumental broadening was corrected by producing an XRD pattern of the Cu powder annealed at 900°C for 1 h. The Scherrer equation, as given below [7-9],

was applied to the first peak of the XRD patterns to evaluate the average grain size of the powder particles:

$$D_{hkl} = K\lambda / (\beta_{hkl} \cos\theta) \tag{3-1}$$

where D_{hkl} is the mean grain size, K is a constant and normally taken to be 1, λ is the wavelength of the x-rays used to generate the XRD patterns, β_{hkl} is the integral breadth of the x-ray diffraction peak (in radians) of the planes with Miller indices of {hkl}, and θ is the Bragg angle of the peak used. The internal strain, ε_{hkl}, of the samples was derived from the following equation [10]:

$$\varepsilon_{hkl} = \beta_{hkl} / (4\tan\theta) \tag{3-2}$$

The dislocation density of samples, ρ, was evaluated by the formula given below [11-13]:

$$\rho = 2\sqrt{3}\left\langle \varepsilon_{hkl}^2 \right\rangle^{1/2} / (D_{hkl} b) \tag{3-3}$$

where b is the Burger's vector of pure Cu. In the dislocation density calculation, the first three peaks of XRD patterns were used to obtain the average dislocation densities of the samples.

Figures 3.2(a) and (b) show the average grain sizes as a function of annealing time at different annealing temperatures and a function of annealing temperature with different annealing times, respectively. Figures 3.2(a) and (b) demonstrate that the grain sizes almost remained unchanged with increasing annealing time for an annealing temperature of 400°C or lower, while when the annealing temperature is 500°C or higher, the grain sizes first increased at a rate which became higher with increasing annealing temperature, and then reached stagnation with prolonged annealing time.

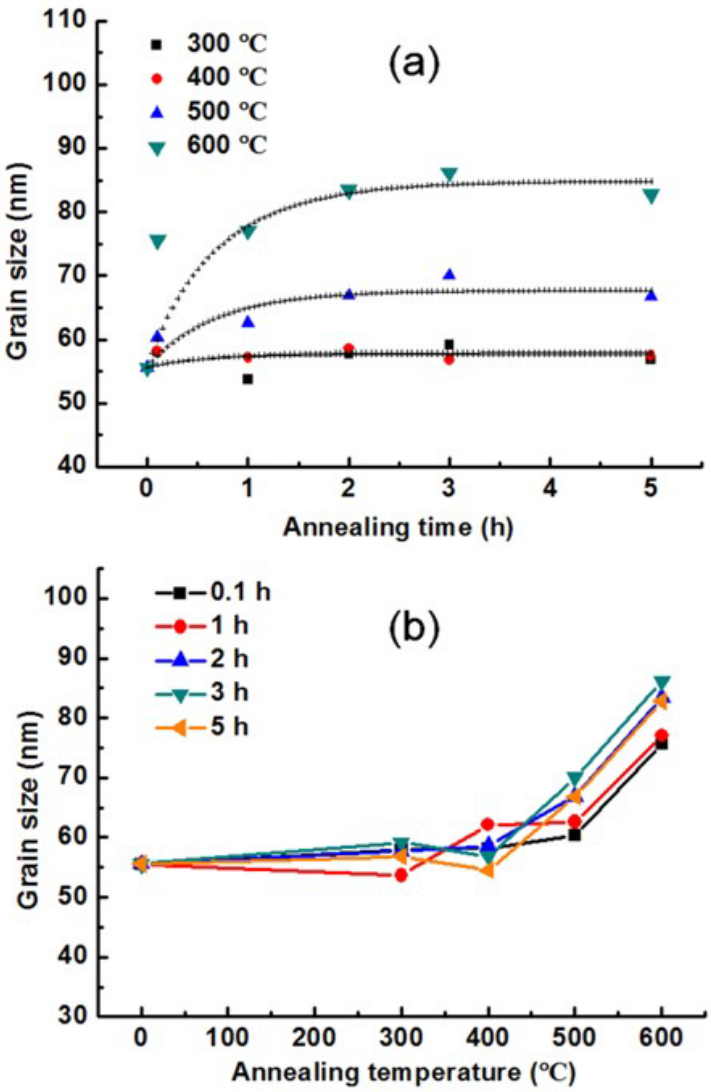

Figure 3.2: Changes of grain sizes of the nanocrystalline Cu matrix of Cu-5vol.%Al_2O_3 composite powder particles with annealing time at different annealing temperatures (a) and with annealing temperature for different annealing times (b).

The dislocation densities as a function of annealing time at different annealing temperatures and a function of annealing temperature with different annealing times are presented in Figures 3.3(a) and (b) respectively.

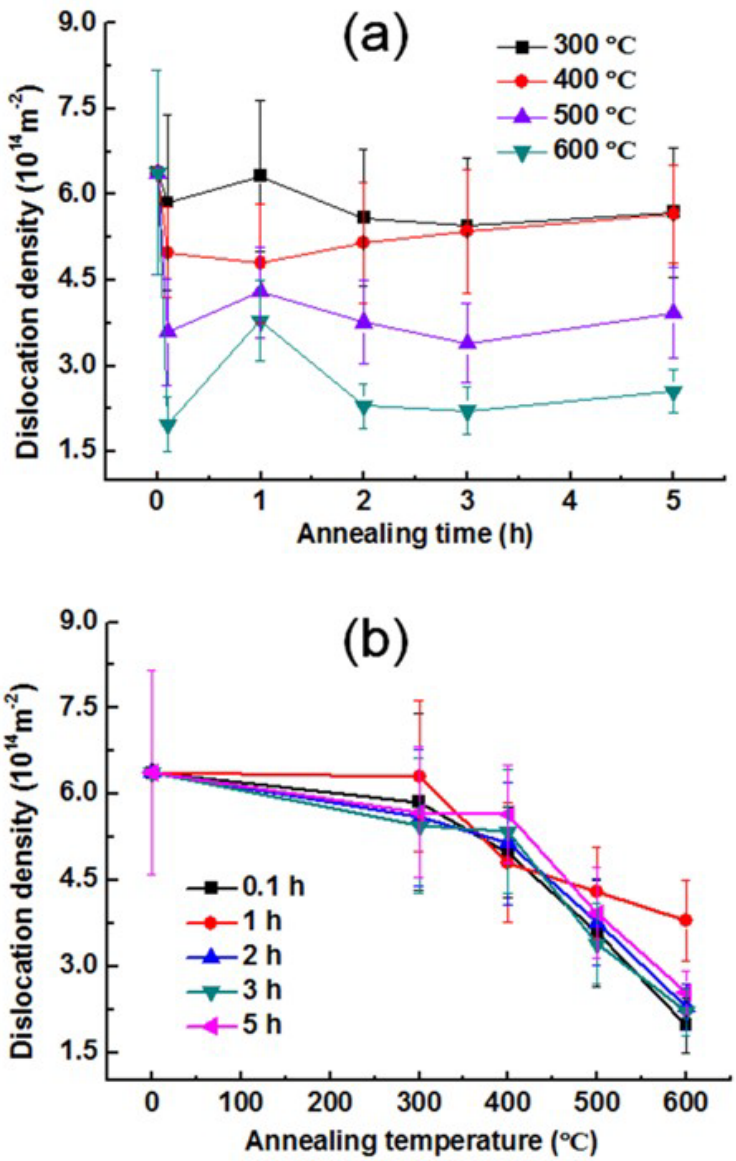

Figure 3.3: Variation of dislocation density of nanostructured Cu-5vol.%Al_2O_3 composite powder particles with annealing time at different annealing temperatures (a) and with annealing temperature for different annealing times (b).

As shown in Figure 3.3(a), at a given annealing temperature, the dislocation density dropped significantly within the first 0.1 h of annealing, then underwent fluctuation with increasing annealing time, and subsequently changed little with subsequent increased annealing time. As shown in Figure 3.3(b), the dislocation density of the annealed powder particles did not change significantly with increasing annealing temperature from room temperature to 300°C, and then showed a significant linear decrease with increasing annealing temperature from 300 to 600°C.

To check whether the average Cu grain sizes determined by analyzing the broadening of XRD peaks are reasonably accurate, the microstructure of as-milled powder particles and the powder particles annealed at 600°C for 5 hours was examined using TEM. As shown in Figure 3.4, the Cu grain sizes of the as-milled powder particles were in the range of 17-120 nm, while the majority of Cu grains in the powder particles annealed for 5 hours at 600°C were in the range of 20-200 nm. Some large Cu grains with sizes in the range of 200-300 nm and surrounded by nanometer sized Cu grains were also found in the microstructure of the powder particles annealed for 5 hours at 600°C, as shown in Figure 3.4(b), indicating that abnormal grain growth occurred during annealing at 600°C. Based on the Cu grain size distributions determined by measuring the sizes of 188 and 247 Cu grains in the microstructures of as-milled powder particles and the powder particles annealed at 600°C for 5 hours, respectively (Figures 3.4(c) and (d)), the average grain sizes were determined to be 50±20 and 91±47 nm, respectively. This shows that the average grain size values obtained from analyzing the broadening of XRD peaks are reasonably accurate, and thus can be used in the subsequent analysis of the kinetics of grain growth.

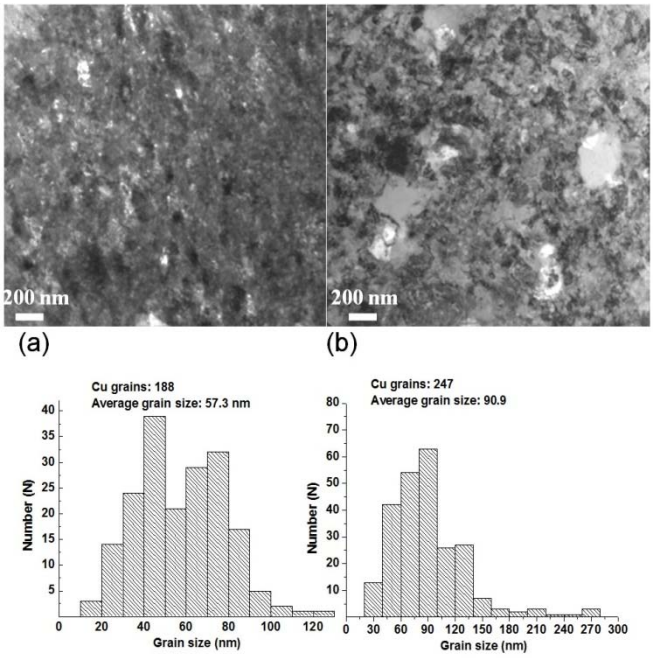

Figure 3.4:TEM bright field micrographs of (a) as-milled nanostructured Cu-5vol.%Al_2O_3 composite powder particles and (b) powder particles annealed at

600°C for 5 h and (c) and (d) their corresponding grain size distributions respectively.

As shown by the selected area electron diffraction patterns (SADPs) shown in Figures 3.5(a) and (b), annealing as-milled powder particles at 600°C for 5 hours generated a group of weak diffraction spots corresponding to Al_2O_3\{311\} (Figure 3.5(b)), which were absent from the SADP of the as-milled powder particle (Figure 3.5(a)). This implies that the growth of Al_2O_3 nanoparticles occurred during annealing at 600°C.

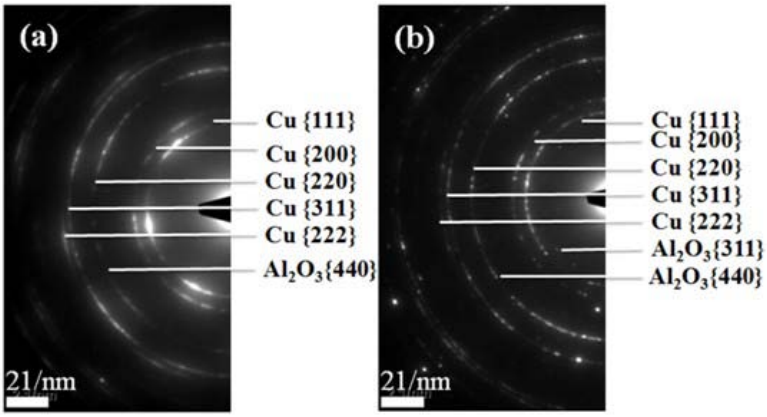

Figure 3.5: Selected area electron diffraction patterns corresponding to the TEM micrographs shown in Figs. 3.4(a) and (b), respectively.

As shown by the SEM backscattered electron images, STEM images and EDX Al elemental maps shown in Figures 3.6 and 3.7, a fraction of Al_2O_3 nanoparticles were dissolved during milling, and relatively large Al_2O_3 nanoparticles survived in the microstructure of the as-milled powder. With the subsequent annealing, the Al^{3+} and O^{2-} ions re-precipitated out to either form new Al_2O_3 nanoparticles or to cause the growth of pre-existing Al_2O_3 nanoparticles, as shown in Figures 3.6(b)-(d) and 3.7(c) and 3.7(d). This is in agreement with the appearance of the Al_2O_3 {311} diffraction spots in the SADP of the powder particle annealed at 600°C and for 5 hours shown in Figure 3.5.

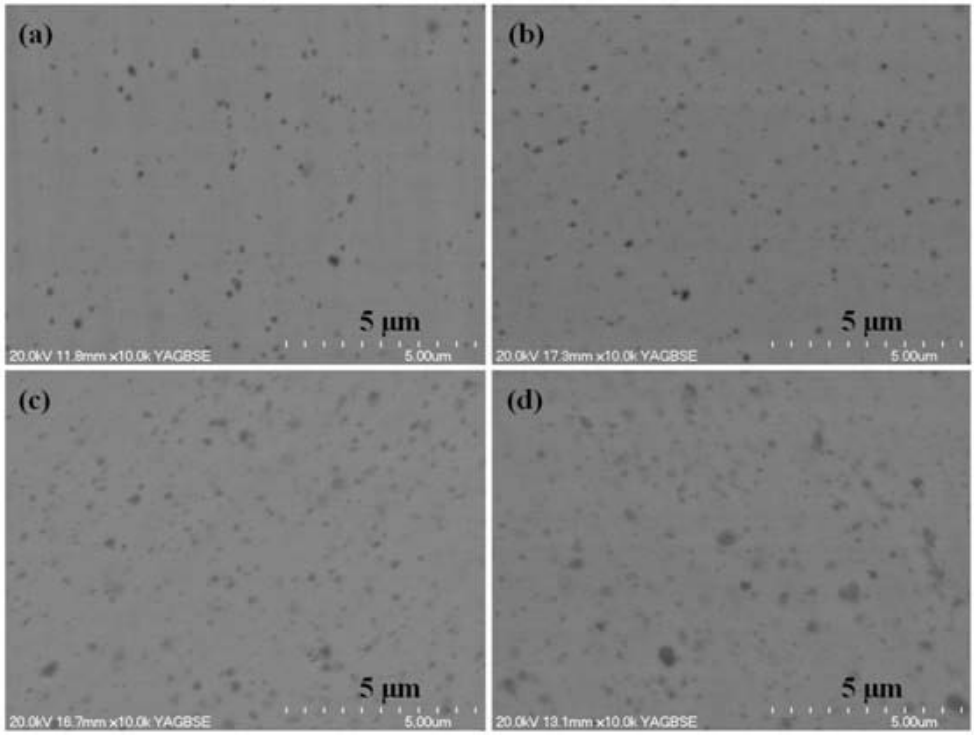

Figure 3.6: Backscattered electron micrographs showing coalescence of Al_2O_3 nanoparticles in the nanostructured Cu-5vol.%Al_2O_3 composite powder particles with annealing. (a) as-milled; (b) annealed at 400°C for 5 h; (c) annealed at 500°C for 5 h; (d) annealed at 600°C for 5 h.

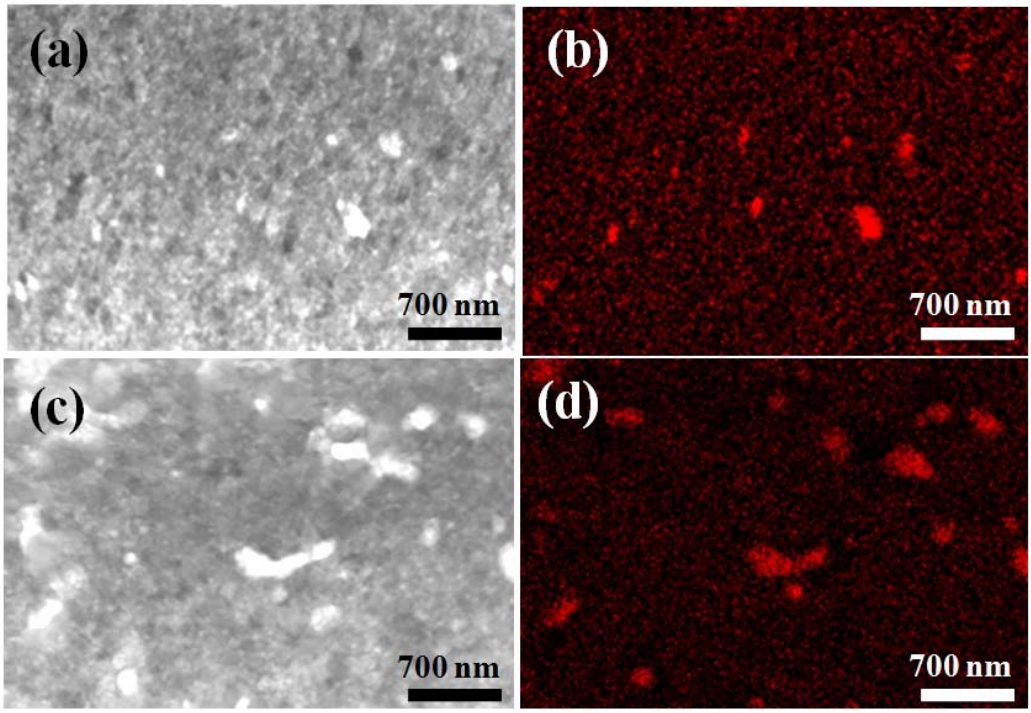

Figure 3.7: STEM images of (a) as-milled nanostructured Cu-5vol.%Al_2O_3 composite powder particles and (c) powder particles annealed at 600°C for 5 h, and (b) and (d) their corresponding EDX Al elemental maps respectively.

Figure 3.8 displays the change of the microhardness of the Cu-5vol.%Al_2O_3 nanocomposite powder particles with increasing annealing time at different annealing temperatures. It shows that the value of the microhardness of the Cu-5vol.%Al_2O_3 nanocomposite powder particles annealed at a given temperature decreased with increasing annealing time within the first 2 h annealing and then reached a plateau with further increases in annealing time. Moreover, the microhardness of the annealed Cu-5vol.%Al_2O_3 nanocomposite powder particles decreased from 2.59 to 1.68 GPa with increasing annealing temperature from room temperature to 600°C. Such changes in the microhardness of the powder particles with the annealing condition clearly reflects the Cu grain growth behavior and the decrease of the dislocation density of the powder particles with increasing annealing time and annealing temperature noted previously.

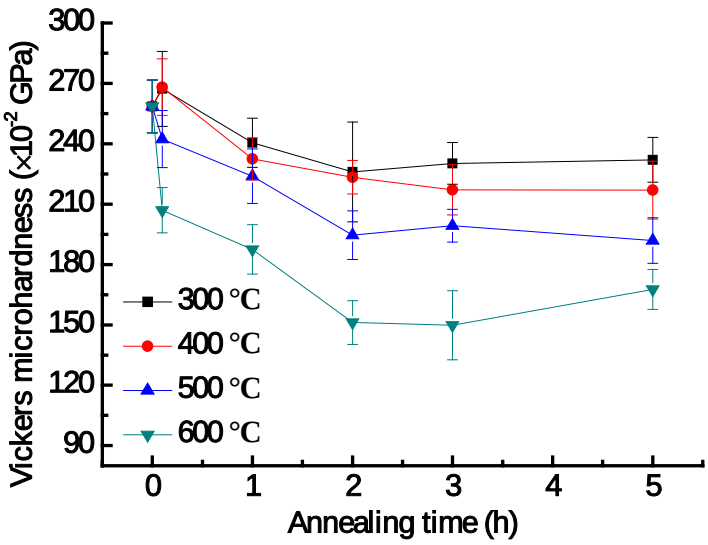

Figure 3.8: Vickers microhardness of the nanostructured Cu-5vol.%Al_2O_3 composite powder particles as a function of annealing time at different annealing temperatures.

3.3 Discussion

3.3.1 Microstructural Evolution during Annealing

As shown in Figures 3.2 and 3.3, when the as-milled powder particles are annealed at temperatures ≤400°C, the average Cu grain size remains nearly unchanged, while those powder particles annealed at temperatures ≥500°C exhibit clear grain growth (Figure 3.2). This observation is similar to the finding obtained by Čížek et al. [14] that no visible grain growth or recrystallization of the nanocrystalline Cu matrix occurs during annealing of Cu-0.5wt.%Al_2O_3 nanocomposite at temperatures below 400°C. In contrast, the dislocation density of the as-milled powder particles decreases continuously with increasing the annealing temperature from 300 to 600°C (Figure 3.3). Abnormal grain growth occurs during annealing at 600°C, as shown in Figure 3.4(b). This might be caused by the coalescence of fine Al_2O_3 particles, leaving some regions having a relatively lower density of Al_2O_3 nanoparticles. As shown in Figures 3.6, 3.7 and 3.9, it has also been observed that a fraction of the Al_2O_3 particles of the as-milled powder particles coarsen and their sizes reach a level larger than 100 nm after annealing at 600°C for 5 hours. These large Al_2O_3 particles are less effective in dragging the migration of grain boundaries and thus allow faster grain growth than Al_2O_3 nanoparticles smaller than 50 nm [15]. As a result, some grains adjacent to large Al_2O_3 particles grew abnormally, as shown in Figure 3.4(b).

3.3.2 The Kinetics of Grain Growth of the Nanocrystalline Cu Matrix

Based on the consideration that the grain growth of a polycrystalline material is driven by the grain boundary curvature, the grain size, D, as a function of annealing time, t, can be described by using a power law equation [16-17]:

$$D^n - D_0^{\ n} = kt \qquad (3\text{-}4),$$

where n is a constant, D_0 is the initial grain size at time t=0, and k is a temperature-dependent grain growth rate constant. If the material is a pure single phase material, n = 2. However, during grain growth, many factors such as second

phase particles [18], impurities [19-20], solute atoms [21], strain release [22], pores and grain boundary triple junctions [23-24] can affect the kinetics of grain growth and lead to n>2 [25]. In this study, we assume that the curvature-driven grain growth mechanism is still operative and Equation (3-4) can be used to quantify the grain growth. Considering the influence of Al_2O_3 nanoparticles on the grain growth of nanocrystalline Cu matrix, we take n=3, thus Equation (3-4) can be rewritten as:

$$D^3 - D_0^{\ 3} = kt \qquad (3\text{-}5).$$

The values of k at different annealing temperatures were obtained by fitting Equation (3-5) with the grain size data obtained from the isothermal annealing experiments shown in Figure 3.2(a). k changes with temperature according to the Arrhenius relationship [16]:

$$k = k_0 \exp\left[-\frac{E}{RT}\right] \qquad (3\text{-}6),$$

where R is the ideal gas constant, T the absolute temperature, E the apparent activation energy for grain growth and k_0 a constant. Based on Equation (3-6), the value of the grain growth activation energy, E, can be obtained from the slope of the line of ln(k) vs 1/RT. By producing a line which best fits the data points of (1/RT, k) at three different temperatures (400, 500 and 600°C) as shown in Figure 3.10 and determining the slope of this line, the value of the activation energy of grain growth of the nanocrystalline Cu matrix of the as-milled nanocomposite powder particles was determined to be 63.4 kJ/mol.

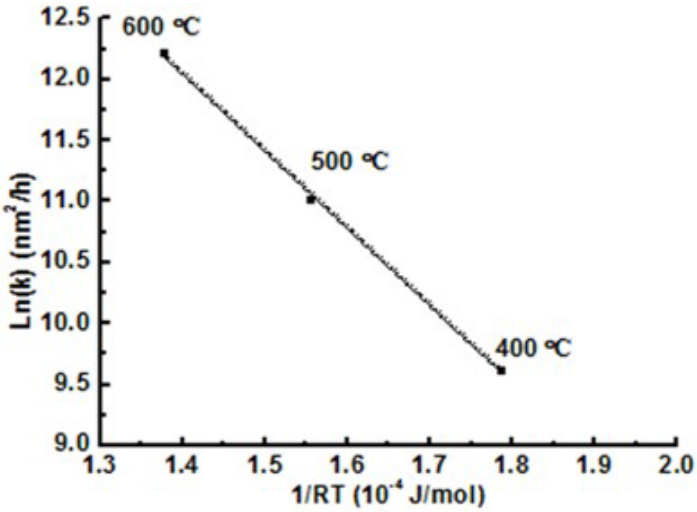

Figure 3.9: Arrhenius plot of the grain growth rate constant.

For comparison, the values of the apparent activation energy of grain growth of monolithic nanocrystalline Cu collected from published literature [26,22,27-30] along with the value obtained in this study are summarized in Table 3.1. It can be seen that the reported apparent activation energy of grain growth of monolithic nanocrystalline Cu is in the range of 30-83 kJ/mol, which is much smaller than that for the grain growth of microcrystalline Cu (211 kJ/mol) [31], indicating that the grain growth behavior of nanocrystalline Cu is quite different from the lattice diffusion controlled grain growth of microcrystalline Cu and is determined by grain boundary diffusion. The value of the apparent activation energy of grain growth of the nanocrystalline Cu matrix of the Cu-5vol.%Al_2O_3 nanocomposite (63.4 kJ/mol) falls well within the range of reported values of the apparent activation energy of grain growth of monolithic nanocrystalline Cu shown in Table 3.1. This shows that the grain growth kinetics of the nanocrystalline Cu matrix of the Cu-5vol.%Al_2O_3 nanocomposite powder particles prepared by HEMM are also controlled by grain boundary diffusion.

Table 3.1 Values of apparent activation energy for grain growth of monolithic nanocrystalline Cu published in the literature and that of the nanocrystalline Cu matrix of the nanostructured Cu-5vol.%Al_2O_3 composite obtained in this study (IKA: Isothermal Kinetics Analysis).

Preparation method	Materials	Temperature range (K)	Study method	Activation energy (kJ/mol)	Reference
Inert gas condensation +compaction	Nanocrystalline Cu (99.95% pure)	283-425	Tracer or nuclear magnetic relaxation	61.56 or 66.37	[27, 29]
DC magnetron sputtering	Nanocrystalline Cu	573-773	IKA (n=2)	38.7	[30]
DC magnetron sputtering	Nanocrystalline Cu	373-773	IKA (n=3)	35±11	[26]
Sliding wear	Nanocrystalline Cu (99.2% pure)	575-675	IKA (n=4)	30±9	[28]
Electrodeposition	Nanocrystalline Cu (99.983% pure)	373-423	IKA (n=4)	83±13	[22]
HEMM	Nanocrystalline Cu Matrix	573-873	IKA (n=3)	63.4±2	This study

3.3.3 The Effect of Al_2O_3 Nanoparticles on the Grain Growth of Nanocrystalline Cu Matrix

Fine second phase particles located at grain boundaries exert a retarding force to the grain boundaries so that their migration becomes more difficult. Such an effect can result in a much lower rate of grain growth for a nanocrystalline metal matrix dispersed with fine second phase particles compared with its monolithic nanocrystalline counterpart. Indeed, although the apparent activation energy for grain growth of the nanocrystalline Cu matrix of the Cu-5vol.%Al_2O_3 nanocomposite (Figure 3.2(a)) is very close to that of monolithic nanocrystalline Cu, the growth rate of the former during annealing at elevated temperatures in the range of 400-600°C is far lower than that of the latter in the same temperature range. For instance, after 5 hours annealing at 500°C, the average grain size of monolithic nanocrystalline Cu increases from 50 to 280 nm [26], while the average grain size of the nanocrystalline Cu matrix of the Cu-5vol.%Al_2O_3 nanocomposite only increases from 56 to 65 nm.

According to Zener pinning [16], a balance between the pinning force exerted on a grain boundary by fine second phase particles and the driving force for grain growth can be established in a material dispersed with the second phase particles. This suggests that the grain sizes and grain boundaries with a homogeneous distribution of a small amount of fine second phase particles are able to reach a metastable state with increasing annealing time, and in such a state the grain growth would virtually stop with a further increase of annealing time.

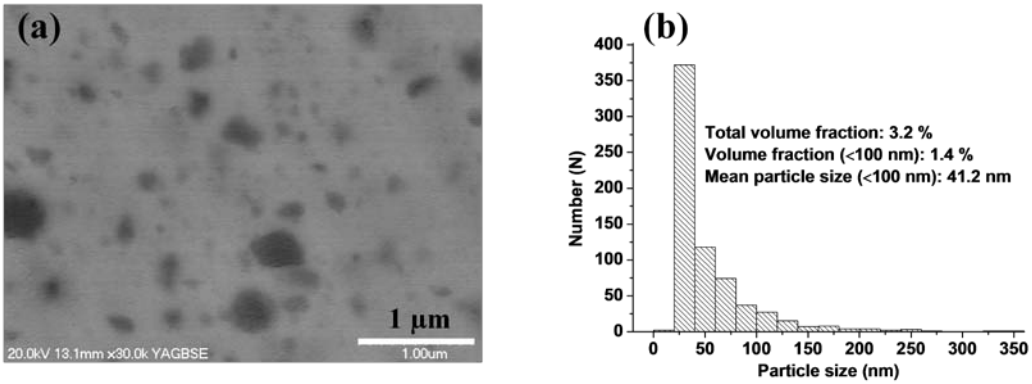

Figure 3.10: (a) Backscattered electron image of the Cu-5vol.%Al_2O_3 nanocomposite powder particle annealed at 600°C for 5 h; (b) particle size distribution of the Al_2O_3 nanoparticles.

Based on the particle pinning theory [32], the relationship between the particle parameters (i.e. volume fraction, f, and size, d, of the particles) and grain size D can be empirically described by the following equation:

$$\frac{D}{d} = \frac{4}{3f} \qquad (3\text{-}7).$$

The powder particles annealed at 600°C for 5 h was taken as a model to analyze the effect of Al_2O_3 nanoparticles on the grain growth of nanocrystalline Cu matrix of the Cu-5vol.%Al_2O_3 nanocomposite. In this analysis, Al_2O_3 particles with sizes larger than 100 nm are not taken into account because of their negligible effect on the thermal stability of the nanocrystalline Cu matrix. By substituting d=41.19 nm and f=1.36% presented in Figure 3.9(b) into Equation (3-7), we get D=4038 nm, which

means that the metastable grain size of the Cu matrix should reach around 4 μm. This value of mean grain size is much larger than the actual mean grain size of the Cu-5vol.% Al_2O_3 nanocomposite annealed at 600 ^oC for 5 hours which is 91 nm, as determined by both TEM examination and X-ray analysis. The data shown in Figure 3.9(b) show that the total volume fraction of Al_2O_3 nanoparticles accounted for in the measurement is 3.23vol.%, indicating that there is still ~1.77vol.%Al_2O_3 left in the matrix and which may be in the form of Al^{3+}/O^{2-} clusters, being too small to be resolved clearly by SEM and TEM. If we assume that the Al^{3+}/O^{2-} clusters have a mean size of 5 nm and then do the calculation using Equation (3-7) again, the calculation generates a D value of 376 nm, which is still 4 times higher than the actual average grain size of 91 nm. This means that the high thermal stability of as-milled powder particles observed may not be entirely provided by the pinning effect of Al_2O_3 nanoparticles and Al^{3+}/O^{2-} clusters, and other stabilization factors may be involved.

In nanostructured materials fabricated by HEMM, the impurities coming from the ambient environment and/or milling tools can strongly influence the thermal stability of the materials produced and such impurities may play an important role in enhancing the stability of the nanostructure of the powder particles [18,20,19,33]. After 24 h milling, the chemical composition of the milled powder examined by XRF includes 0.175wt.%Fe. Fe has very limited solubility in a Cu lattice at temperatures lower than 600^oC. This implies that the Fe atoms in the nanostructured Cu-5vol.%Al_2O_3 nanocomposite are very likely segregated at the grain boundary during annealing at 600^oC. The segr/egated Fe atoms at the grain boundaries of the Cu matrix may impose a retarding force against the motion of the grain boundary via the solute drag effect. Therefore, both the Zener drag and the solute drag contribute to the high thermal stability of the milled Cu-5vol.%Al_2O_3 nanocomposite powder particles.

3.4 Summary

A systematic investigation of the microstructural changes that occur during isothermal annealing of a nanostructured Cu-5vol.%Al_2O_3 nanocomposite powder prepared by high energy mechanical milling has been performed. The results show that annealing at 300 or 400°C only causes a reduction of the dislocation density of the powder particles, while annealing at 500 or 600°C causes reduction of dislocation density, abnormal grain growth of the nanocrystalline Cu matrix and coarsening of Al_2O_3 nanoparticles. Analysis of the grain growth kinetics of the nanocrystalline Cu matrix of the Cu-5vol.%Al_2O_3 nanocomposite shows that the apparent activation energy for the grain growth in the temperature range of 400-600°C is 63.4 kJ/mol, being very similar to that of monolithic nanocrystalline Cu in the same temperature range and showing both are grain boundary diffusion controlled. However, the microstructure of the nanostructured Cu matrix of the nanocomposite exhibits a far higher thermal stability than that of monolithic nanocrystalline Cu, with most of the Cu grains being still in the nanometer scale after annealing at 600°C for 5 hours. This high thermal stability of the nanocrystalline Cu matrix of the nanocomposite can be attributed to the drag effects of finely distributed Al_2O_3 nanoparticles, Al^{3+}/O^{2-} clusters and impurity Fe atoms on the grain boundary motion.

3.5 References

1. Han BQ, Ye J, Newbery AP, Zhu YT, Schoenung JM, Lavernia EJ (2009) Bulk Nanostructured Metals from Ball Milling and Consolidation. In: Zehetbauer MJ, Zhu YT (eds) Bulk Nanostructured Materials, Wiley, Weinheim, pp 273-291
2. Zhang DL, Raynova S, Koch CC, Scattergood RO, Youssef KM (2005) Consolidation of a Cu-2.5 vol.% Al_2O_3 powder using high energy mechanical milling. Materials Science and Engineering: A 410:375-380
3. Cheng S, Ma E, Wang YM, Kecskes LJ, Youssef KM, Koch CC, Trociewitz UP, Han K (2005) Tensile properties of in situ consolidated nanocrystalline Cu. Acta Materialia 53 (5):1521-1533
4. He L, Ma E (1996) Processing and microhardness of bulk Cu-Fe nanocomposites. Nanostructured Materials 7 (3):327-339

5. Langlois C, Hytch MJ, Lartigue-Korinek S, Champion Y, Langlois P (2005) Synthesis and microstructure of bulk nanocrystalline copper. Metallurgical and Materials Transactions A 36 (12):3451-3460

6. Pozuelo M, Melnyk C, Kao WH, Yang J-M (2011) Cryomilling and spark plasma sintering of nanocrystalline magnesium-based alloy. Journal of Materials Research 26 (07):904-911

7. Scherrer P (1918) Determination of size and structure of colloidal particles by x-ray diffraction. Göttingen Nachrichten 2:98

8. Holzwarth U, Gibson N (2011) The Scherrer equation versus the 'Debye-Scherrer equation'. Nature Nanotechnology 6 (9):534

9. Langford JI, Wilson AJC (1978) Scherrer after sixty years: a survey and some new results in the determination of crystallite size. Journal of Applied Crystallography 11 (2):102-113

10. Stokes AR, Wilson AJC (1944) The diffraction of X rays by distorted crystal aggregates-I. Proceedings of the Physical Society 56 (3):174-181

11. Williamson GK, Smallman RE (1956) III. Dislocation densities in some annealed and cold-worked metals from measurements on the X-ray debye-scherrer spectrum. Philosophical Magazine 1 (1):34-46

12. Zhao YH, Lu K, Zhang K (2002) Microstructure evolution and thermal properties in nanocrystalline Cu during mechanical attrition. Physical Review B 66 (8):085404

13. Ni S, Wang YB, Liao XZ, Alhajeri SN, Li HQ, Zhao YH, Lavernia EJ, Ringer SP, Langdon TG, Zhu YT (2011) Grain growth and dislocation density evolution in a nanocrystalline Ni–Fe alloy induced by high-pressure torsion. Scripta Materialia 64 (4):327-330

14. Čížek J, Procházka I, Cieslar M, Kužel R, Matěj Z, Cherkaska V, Islamgaliev RK, Kulyasova O (2007) Influence of ceramic nanoparticles on grain growth in ultra fine grained copper prepared by high pressure torsion. Physica Status Solidi (C) 4 (10):3587-3590

15. Ďurišin J, Ďurišinová K, Orolínová M, Saksl K (2004) Effect of the MgO particles on the nanocrystalline copper grain stability. Materials Letters 58 (29):3796-3801

16. Burke JE (1949) Some factors affecting the rate of grain growth in metals. AIME 180:73-91

17. Atkinson HV (1988) Overview no. 65: Theories of normal grain growth in pure single phase systems. Acta Metallurgica 36 (3):469-491

18. Zhou F, Lee J, Lavernia EJ (2001) Grain growth kinetics of a mechanically milled nanocrystalline Al. Scripta Materialia 44 (8-9):2013-2018

19. Liu KW, Mücklich F (2001) Thermal stability of nano-RuAl produced by mechanical alloying. Acta Materialia 49 (3):395-403

20. Malow TR, Koch CC (1997) Grain growth in nanocrystalline iron prepared by mechanical attrition. Acta Materialia 45 (5):2177-2186

21. Michels A, Krill CE, Ehrhardt H, Birringer R, Wu DT (1999) Modelling the influence of grain-size-dependent solute drag on the kinetics of grain growth in nanocrystalline materials. Acta Materialia 47 (7):2143-2152

22. Lu L, Tao NR, Wang LB, Ding BZ, Lu K (2001) Grain growth and strain release

in nanocrystalline copper. Journal of Applied Physics 89 (11):6408-6414

23. Gottstein G, Shvindlerman LS, Zhao B (2010) Thermodynamics and kinetics of grain boundary triple junctions in metals: Recent developments. Scripta Materialia 62 (12):914-917

24. Shvindlerman LS, Gottstein G (2004) Efficiency of drag mechanisms for inhibition of grain growth in nanocrystalline materials. Zeitschrift für Metallkunde 95 (4):239-241

25. Humphreys FJ, Hatherly M (2004) Recrystallization and related annealing phenomena. 2 nd edn. Elsevier Science Ltd., UK, pp364-409

26. Simões S, Calinas R, Vieira MT, Vieira MF, Ferreira PJ (2010) In situ TEM study of grain growth in nanocrystalline copper thin films. Nanotechnology 21 (14):145701

27. Horvath J, Birringer R, Gleiter H (1987) Diffusion in nanocrystalline material. Solid State Communications 62 (5):319-322

28. Ganapathi SK, Owen DM, Chokshi AH (1991) The kinetics of grain growth in nanocrystalline copper. Scripta Metallurgica 25 (12):2699-2704

29. Dickenscheid W, Birringer R, Gleiter H, Kanert O, Michel B, Günther B (1991) Investigation of self-diffusion in nanocrystalline copper by NMR. Solid State Communications 79 (8):683-686

30. Cao ZH, Wang F, Wang L, Meng XK (2010) Coupling effect of the electric and temperature fields on the growth of nanocrystalline copper films. Physical Review B 81 (11):113405

31. Mehrer H (2007) Diffusion in solids: fundamentals, methods, materials, diffusion-controlled processes. 1 st edn. Springer-Verlag, Berlin, pp304

32. Smith CS (1948) Grains, phases,and interfaces: as interpretation of microstructure. Metals Technology 15 (4):1-37

33. Hashemi-Sadraei L, Mousavi SE, Vogt R, Li Y, Zhang Z, Lavernia EJ, Schoenung JM (2012) Influence of Nitrogen Content on Thermal Stability and Grain Growth Kinetics of Cryomilled Al Nanocomposites. Metallurgical and Materials Transactions A 43 (2):747-756

Chapter Four

Tensile Properties of Ultrafine Structured Cu-5vol.%Al_2O_3 Nanocomposites Prepared by High Energy Mechanical Milling and Powder Compact Extrusion

4.1 Introduction

Metal matrix nanocomposites (MMNCs) reinforced by a dispersion of nanometer sized ceramic particles (diameter<100 nm) have been extensively investigated [1-10]. In comparison with metal matrix composites (MMCs) reinforced with micrometer sized ceramic particles which have also been widely studied, the advantages of using nanometer sized ceramic particles to reinforce the metal matrix are twofold: stronger strengthening effects through the Orowan mechanism due to much smaller interparticle distances [11-12] and prevention of particle cracking during deformation [13-14]. When the ceramic nanoparticles in the MMNCs are oxide nanoparticles and their volume fraction is not higher than 5%, such materials are also called oxide dispersion strengthened (ODS) alloys.

Among MMNCs which have been studied, copper based MMNCs have been most popular due to their potential of offering high strength, high electrical conductivity and high microstructural stability at elevated temperatures which are highly desirable for applications as resistance welding electrodes, electrical contact and connect materials [12,11,3-5,15,9,16,10,17]. Recently, attention has been paid to combining grain boundary strengthening of the metal matrix and nanoparticle strengthening to raise the strength of MMNCs with a given volume fraction of ceramic nanoparticles to a higher level [5-7,10]. To achieve significant grain boundary strengthening, the grain size of the metal matrix needs to be reduced to less than 500 nm [18]. Such

MMNCs are called ultrafine structured MMNCs. The most widely used materials processing route for synthesizing ultrafine structured MMNCs is high energy mechanical milling (HEMM) of a mixture of starting powders to produce nanostructured powder particles with or without nanometer sized ceramic particles dispersed in them followed by powder consolidation. If the nanoparticles in the final microstructure are not dispersed inside the powder particles through HEMM, they may be produced through reactions such as internal oxidation of powders (e.g. internal oxidation of Cu-Al alloy to form dispersed Al_2O_3 nanoparticles) or internal reactions during heat treatment of the milled powders or powder consolidation. As an excellent example, Nachum et al. [5] recently reported that the ultrafine structured Cu-(1 and 5)vol.%Al_2O_3 nanocomposites made by a combination of HEMM, powder oxidation and powder consolidation exhibited high tensile yield strength of up to 460 and 620 MPa, respectively, and a good ductility reflected by an elongation to fracture of 10%. To reinforce the achievement of this work, our study demonstrates that ultrafine structured Cu-5vol.%Al_2O_3 nanocomposite samples with a combination of high strength and good ductility can also be produced by a combination of HEMM of a mixture of Cu powder and Al_2O_3 nanoparticles and powder compact extrusion. We also discovered that dissolution of Al_2O_3 nanoparticles during heating and extrusion had a significantly beneficial effect on the mechanical properties of the ultrafine structured Cu-5vol.%Al_2O_3 nanocomposite.

4.2 Results

From the bright and dark field TEM images and STEM images as shown in Figures 4.1 and 4.2, it can be seen that the sample consolidated at 750°C had a microstructure consisting of equiaxed Cu grains with sizes in the range of 100-500 nm, and increasing the extrusion temperature to 900°C did not change the grain sizes significantly. The XRD patterns of the consolidated samples shown in Figure 4.1(e) only exhibited diffraction peaks of Cu. The absence of Al_2O_3 peaks in the XRD

patterns may be due to low crystallinity and small sizes of gamma Al_2O_3 nanoparticles. The mean grain size and internal strain of the two consolidated samples were estimated based on the XRD line broadening analysis of Cu peaks through the modified Williamson-Hall and classic Williamson-Hall methods [19-20]. The background and $K_{\alpha 2}$ signal were removed and careful correction for instrumental broadening was done prior to carrying out the analysis. The calculated values of the mean grain size and the square root of the mean square of the internal strain were 272 nm and 1.24×10^{-7} for the sample extruded at 750°C, and 237 nm and 6.4×10^{-7} for the sample extruded at 900°C. By using the following equation [21-22]:

$$\rho = \frac{2\sqrt{3}}{Db}\sqrt{\langle \varepsilon^2 \rangle} \tag{4-1}$$

where ρ, D, b and $<\varepsilon^2>$ are the dislocation density, mean grain size, Burgers vector and mean square of the internal strain of the sample extruded, the dislocation densities of samples extruded at 750 and 900°C were calculated to be 1.75×10^{13} and 3.98×10^{13} m^{-2} respectively.

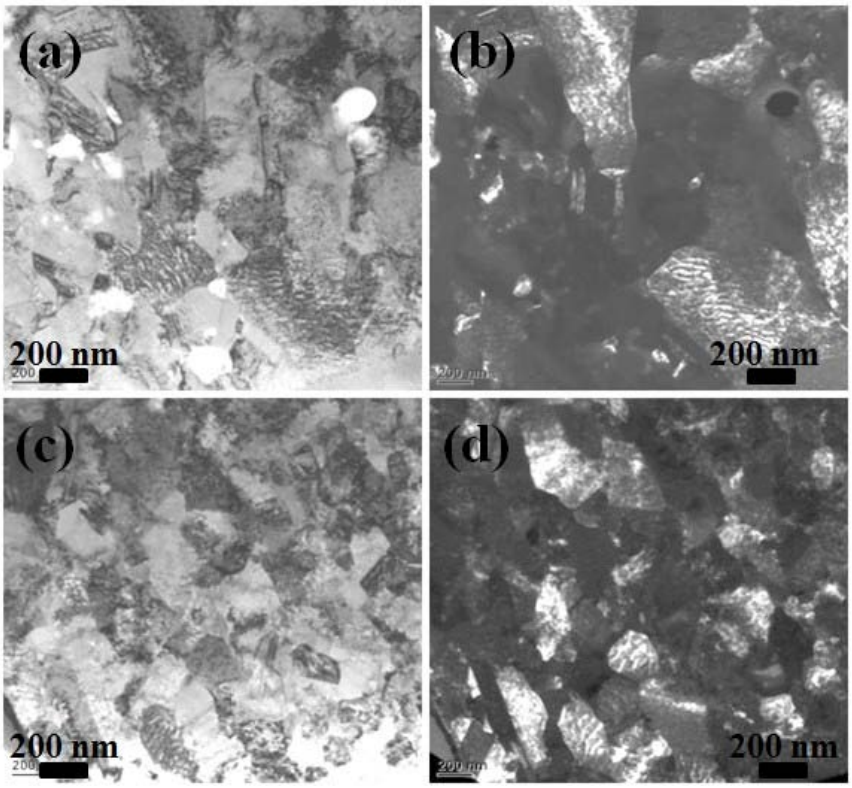

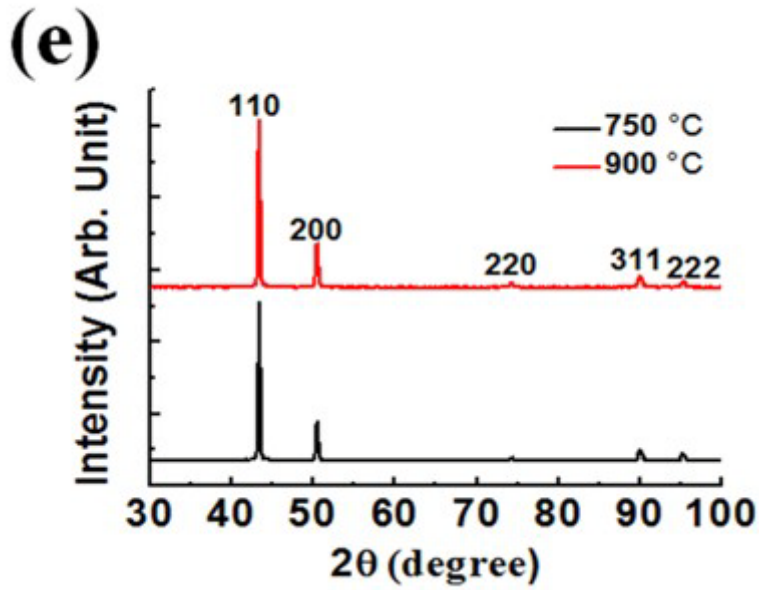

Figure 4.1: The bright field ((a) and (c)) and dark field ((b) and (d)) TEM micrographs and XRD patterns ((e)) of Cu-5vol.%Al_2O_3 samples extruded at 750 and 900°C, respectively.

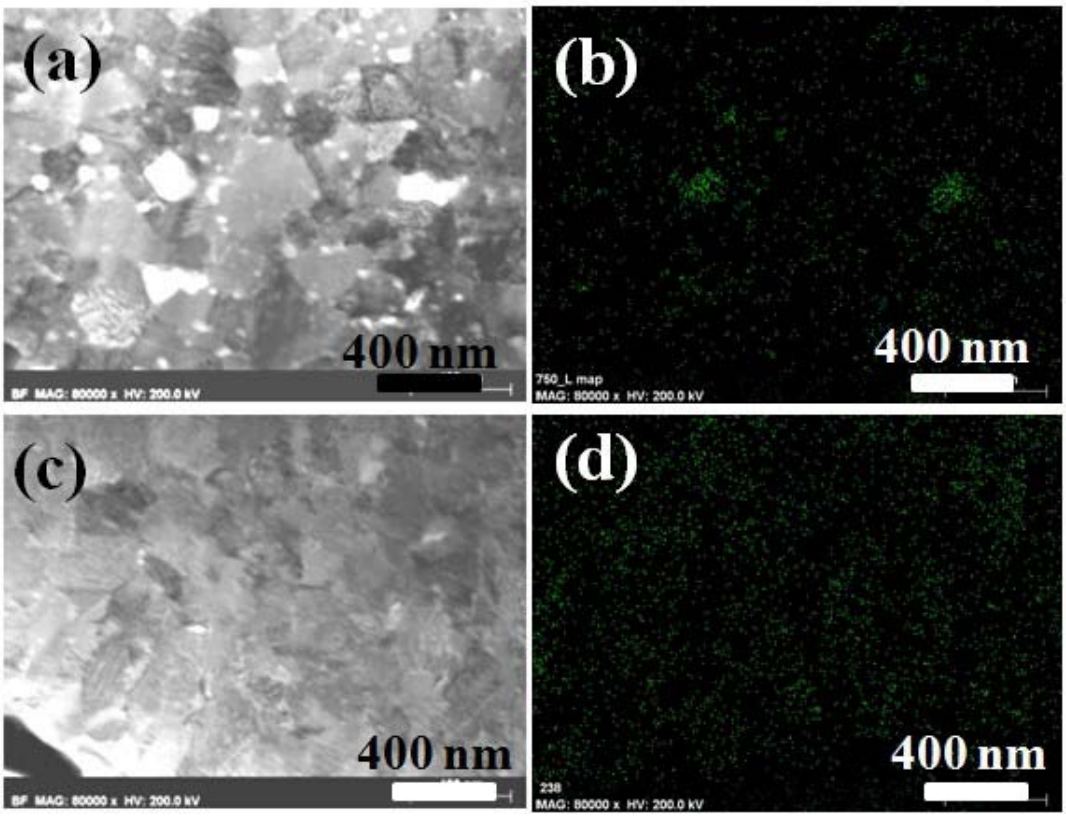

Figure 4.2: The STEM images ((a) and (c)) and corresponding EDX Al elemental maps ((b) and (d)) of Cu-5vol.%Al_2O_3 samples extruded at 750 and 900°C, respectively.

Based on the TEM bright field images, STEM images, EDX elemental mapping and SEM backscattered electron images shown in Figures 4.1-4.3, we can see that the microstructure of the samples extruded at 750°C had a dispersion of Al_2O_3 nanoparticles with sizes in the range of 20-345 nm. Based on the SEM backscattered electron images, the volume fraction of the Al_2O_3 nanoparticles and nanoparticle clusters was estimated to be around 5vol.%, showing that the amount of Al_2O_3 being dissolved in the matrix was insignificant. As clearly shown in Figures 4.1(a) and 4.2(a), the Al_2O_3 nanoparticles/nanoparticle clusters are mostly distributed along the grain boundaries. With increasing the extrusion temperature from 750 to 900°C, the sizes of Al_2O_3 nanoparticles/nanoparticle clusters clearly increased to the range of 20-450 nm, and the number density of the Al_2O_3 nanoparticles/nanoparticle clusters in the microstructure clearly decreased. Based on the SEM backscattered electron images of the sample extruded at 900°C, the volume fraction of the Al_2O_3 nanoparticles/nanoparticle clusters was estimated to be about 1.38vol.%, showing that 3.62vol.% of Al_2O_3 nanoparticles being dissolved during heating the powder compact to 900°C and extrusion. The size distributions of Al_2O_3 nanoparticles/nanoparticle clusters in the two consolidated samples were also determined and they are shown in Figures 4.3(a) and (b).

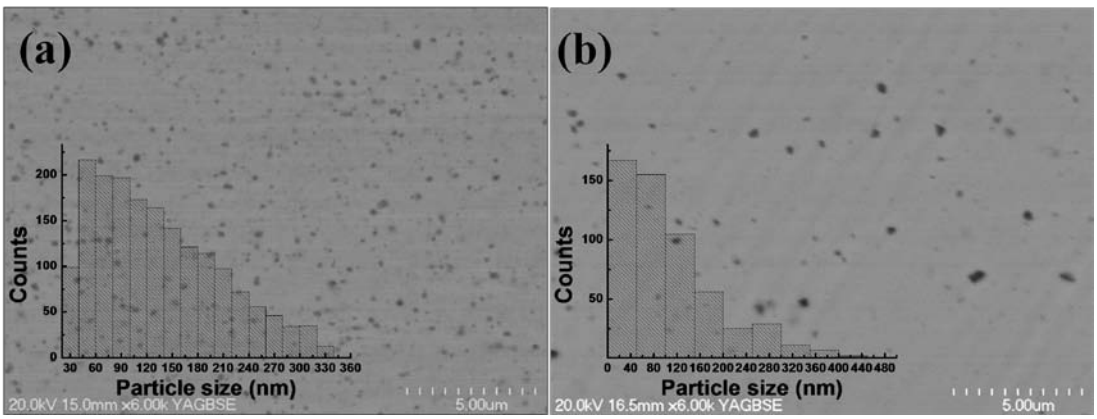

Figure 4.3: SEM backscattered electron images of Cu-5vol.%Al_2O_3 samples extruded at different temperatures: (a) 750°C and (b) 900°C. Insets in (a) and (b) are their corresponding Al_2O_3 particle size distributions.

As seen from the tensile engineering stress-strain curves shown in Figure 4.4 and the

values listed in Table 4.1, the samples consolidated at 750 and 900°C had an average yield strength (YS) of 414 and 566 MPa, an average ultimate tensile strength (UTS) of 478 and 630 MPa and an average elongation to fracture of 5.65% and 7.6%, respectively.

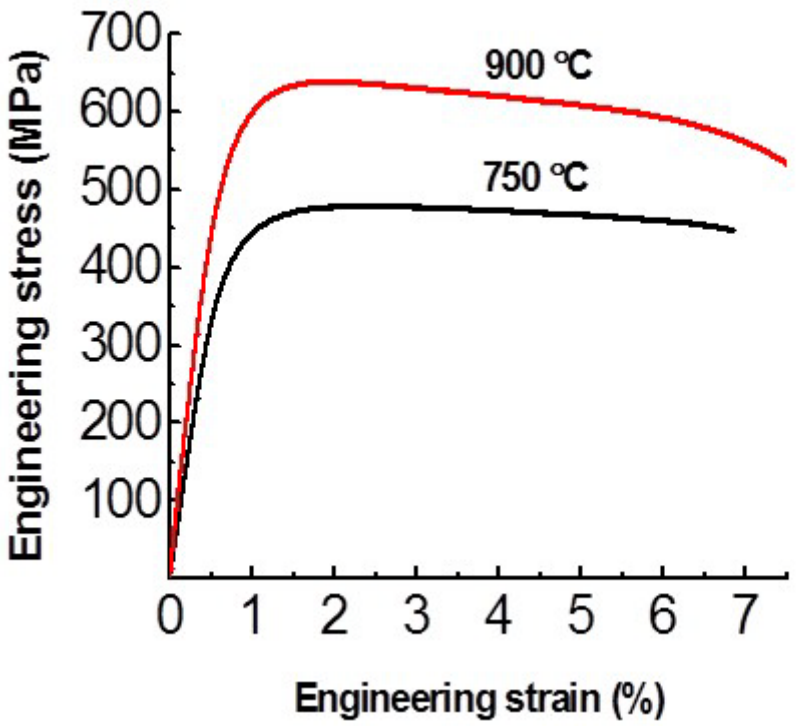

Figure 4.4: The tensile engineering stress-engineering strain curves of Cu-5vol.%Al_2O_3 samples extruded at 750 and 900°C, respectively.

Table 4.1: The average tensile yield strength (YS), ultimate tensile strength (UTS) and elongation to fracture (ε_f) of the Cu-5vol.%Al_2O_3 samples extruded at 750 and 900°C, respectively.

ET (°C)	YS (MPa)	UTS (MPa)	ε_f(%)
750	414 ± 46.4	478 ± 1.7	5.65 ± 2.26
900	566.5 ± 10.4	630 ± 6.2	7.54 ± 2.67

ET: Extrusion temperature.

As shown by the tensile stress-strain curves, the samples exhibited nearly ideal (or nearly perfect) plastic deformation in tension, being lack of both significant strain hardening and necking before fracturing. This observation is consistent with similar observations made on tensile mechanical response of ultrafine structured Cu-(1 and

5)vol.%Al_2O_3 nanocomposites [5] and nanocrystalline pure Cu [23]. As shown in Figure 4.5(a), the fracture surfaces of the tensile test specimens cut from the sample extruded at 750°C showed a large number of rounded dimples which are indicators of cavities formed through Al_2O_3 nanoparticle/Cu matrix decohesion and perhaps also debonding at prior interparticle boundaries during plastic deformation. On the other hand, as shown in Figure 4.5(b), the fracture surfaces of the tensile test specimens cut from the sample extruded at 900°C showed a much smaller number of rounded dimples. Instead, much larger and deeper dimples formed by intergranular fracture and smaller and shallower dimples formed through transgranular fracture were observed.

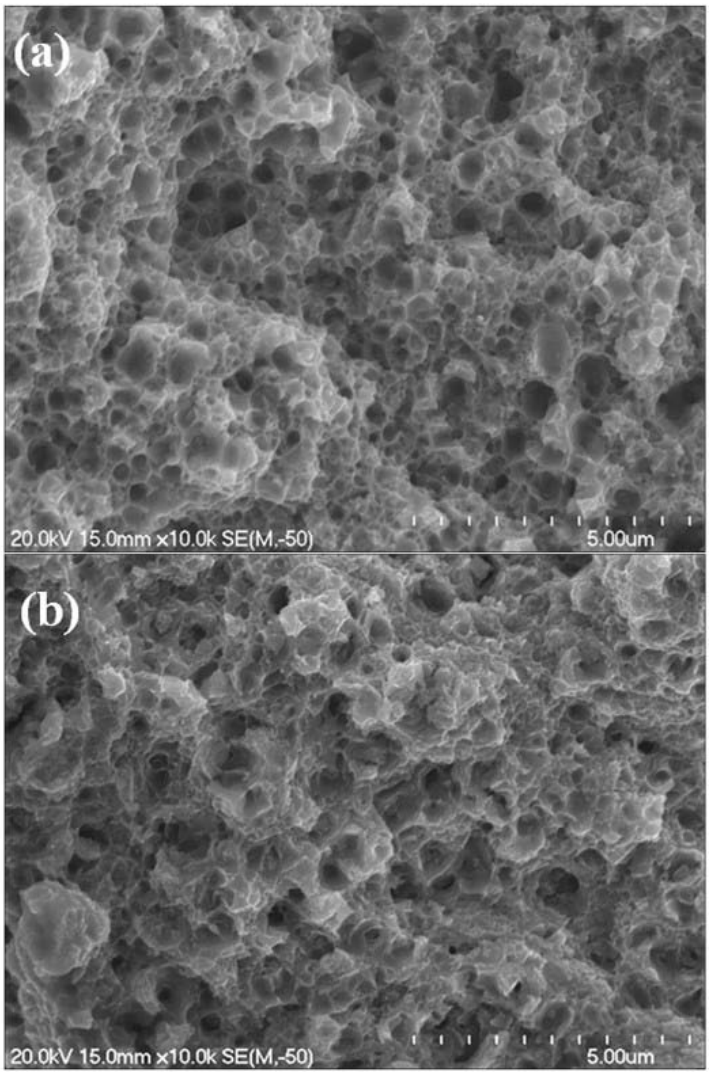

Figure 4.5: The fracture surfaces of Cu-5vol.%Al_2O_3 samples extruded at 750 and 900°C, respectively.

4.3 Discussion

It can be envisaged that the yield strength of the Cu-5vol.%Al_2O_3 nanocomposite samples, σ_y, is the sum of the basic strength of copper associated with lattice friction of dislocations, σ_0, the strength increase caused by grain boundary strengthening, $\Delta\sigma_{gb}$, nanoparticle strengthening, $\Delta\sigma_{np}$ and dislocation strengthening, $\Delta\sigma_\rho$. Thus, we have the following equation:

$$\sigma_y = \sigma_0 + \Delta\sigma_{gb} + \Delta\sigma_{np} + \Delta\sigma_\rho \qquad (4\text{-}2).$$

For copper, σ_0 is quite small, being in the order of 5 MPa [24]. $\Delta\sigma_{gb}$ can be estimated by using the Hall-Petch relationship which is expressed by the following equation:

$$\Delta\sigma_{gb} = k_{HP} D^{-1/2} \qquad (4\text{-}3),$$

where k_{HP} is the Hall-Petch coefficient. Based on previous work on the relationship between the strength of copper and its mean grain size [25], we can take k = 0.142 MPa $m^{1/2}$. As mentioned above, the mean grain sizes of samples extruded at 750 and 900°C are 272 and 237 nm, respectively. By using Equation (4-3), it can be estimated that $\Delta\sigma_{gb}$ is 272 and 291 MPa for the samples extruded at 750 and 900°C, respectively. Based on the Orowan mechanism of nanoparticle strengthening which considers the interaction between dislocations and non-shearable nanoparticles leading to the formation of Orowan loops [26], $\Delta\sigma_{np}$ can be estimated using the following equation:

$$\Delta\sigma_{np} = 0.13\frac{Gb}{\lambda}\ln\left(\frac{r_p}{b}\right) \qquad (4\text{-}4),$$

where G is the shear modulus, b is the Burgers vector, r_p is the mean radius of the nanoparticles and $\lambda = r_p\sqrt{\frac{2\pi}{3f}}$ [27] is the interparticle spacing (f is the volume fraction of the nanoparticles). For copper, we can take G = 47.7 GPa and b = 0.256

nm [28,24]. For the sample extruded at 750°C, the nanoparticle clusters with sizes greater than 200 nm are disregarded in the consideration, since they are too large to be effective in causing strengthening through forming dislocation loops. For particles with sizes smaller than 200 nm, based on Figure 4.3(a), the volume fraction and mean radius size of Al_2O_3 nanoparticles are 2.43% and 52.5 nm and thus λ = 487.3 nm. The same consideration is also used for the sample extruded at 900°C, based on Figure 4.3(b), the volume fraction and mean radius of Al_2O_3 nanoparticles smaller than 200 nm are 0.5% and 41.3 nm and from which we can get λ = 845.1 nm. Using this information and Equation (4-3), it can be estimated that $\Delta\sigma_{np}$ = 17.3 and 10 MPa for the samples extruded at 750 and 900°C, respectively.

The dislocation strengthening, $\Delta\sigma_\rho$, can be estimated based on the Taylor equation [26]:

$$\Delta\sigma_\rho = M\alpha Gb\sqrt{\rho} \qquad (4\text{-}5),$$

where M and α are the Taylor coefficient and strength coefficient of the dislocation network which can be taken to be 3.06 and 0.2 [17]. As mentioned above, the dislocation densities are 1.75×10^{13} and 3.98×10^{13} m^{-2} for the samples extruded at 750 and 900°C, respectively. Using this information and Equation (4-4), $\Delta\sigma_\rho$ can be estimated to be 31 and 47 MPa for the samples extruded at 750 and 900°C, respectively.

The sums of $\sigma_0 + \Delta\sigma_{gb} + \Delta\sigma_{np} + \Delta\sigma_\rho$ are 335 and 353 MPa for samples extruded at 750 and 900°C, respectively. Referring to Table 4.1, it can be seen that these sums are about 79 and 214 MPa lower than the actual yield strength of the samples consolidated at 750 and 900°C, respectively. For the sample consolidated at 750°C, this significant discrepancy may be caused by the disregard of the synergy between grain boundary strengthening, which is the basis of the Hall-Petch relationship between strength increase and grain size, and nanoparticle strengthening in

calculating the contributions of different strengthening mechanisms. As has been well shown, Equation (4-3) [26] does not make any consideration of the effect of presence of hard nanoparticles on grain boundary strengthening. Similarly, Equation (4-4) was derived based on the consideration that Orowan loops form around hard nanoparticles without the interference of grain boundaries. This is certainly not true for ultrafine structured metal matrix nanocomposites where the grain sizes are very similar to the distances between nanoparticles. More theoretical work is needed to quantify the synergy between grain boundary strengthening and nanoparticle strengthening in ultrafine structured MMNCs.

For the sample extruded at 900°C, the discrepancy is even larger. The very small volume fraction of particles (0.5%) present in the microstructure of this sample would not be sufficient to induce a large enough synergistic effect of nanoparticle strengthening and grain boundary strengthening to account for the approximate 250 MPa discrepancy. It is clear that the main possible reason for this discrepancy is the disregard of the strengthening effect of Al^{3+} and O^{2-} ions and Al^{3+}/O^{2-} clusters in the Cu matrix FCC lattice formed by the dissolution of Al_2O_3 nanoparticles. At this point of research, it is not clear in which form the Al^{3+} and O^{2-} ions exist in FCC Cu lattice. Since Al^{3+} and O^{2-} ions are highly charged, it is very likely that they form electrically neutral Al^{3+}/O^{2-} clusters. The fact that the dissolution of 3.62vol.%Al_2O_3 nanoparticles did not cause any change of the lattice parameter of the Cu lattice (as confirmed by XRD analysis shown above) strongly suggest that all or most of the Al^{3+} and O^{2-} ions exist in the form of nanometer sized and electrically neutral Al^{3+}/O^{2-} clusters. It can be envisaged that the very strong electrostatic attraction within the clusters would not allow the dislocations to cut through, and the dislocations would have to bypass the clusters by forming Orowan loops. This means that we can estimate the contribution of the strengthening effect of Al^{3+}/O^{2-} clusters based on the Orowan looping mechanism. If we take r_p = 5 nm and f = 3.62vol.%, we get λ = 38 nm. Substituting this data into Equation (4-3) and doing the calculation would give $\Delta\sigma_p(Al^{3+}/O^{2-})$ =

125.3 MPa. This value is still not sufficient to account for the 214 MPa discrepancy. However, if we take r_p = 3 nm and f = 3.62vol.%, we can get λ = 22.81 nm. Substituting this into Equation (4-3), we get $\Delta\sigma_{np}(Al^{3+}/O^{2-})$ = 208.7 MPa. This value is very close to the 214 MPa discrepancy. This strongly suggests that the dissolution of Al_2O_3 nanoparticles lead to the formation of Al^{3+}/O^{2-} clusters with sizes around 3 nm.

4.4 Summary

Ultrafine structured Cu-5vol.%Al_2O_3 metal matrix nanocomposite samples prepared by a combination of high energy mechanical milling of a mixture of Cu powder and Al_2O_3 nanopowder and powder compact extrusion exhibit different microstructures due to the use of different extrusion temperatures (750 and 900°C). Increasing the extrusion temperature from 750 to 900°C causes a large fraction of the Al_2O_3 nanoparticles to dissolve, and the dissolution of Al_2O_3 nanoparticles brings a dramatic beneficial effect: significant increase of the strength and clear increase of tensile ductility. It appears that this beneficial effect is caused by the strengthening effect of nanometer sized (possibly around 3 nm) Al^{3+}/O^{2-} clusters formed as a result of the dissolution of Al_2O_3 nanoparticles.

4.5 References

1. Zhang Z, Topping T, Li Y, Vogt R, Zhou Y, Haines C, Paras J, Kapoor D, Schoenung JM, Lavernia EJ (2011) Mechanical behavior of ultrafine-grained Al composites reinforced with B_4C nanoparticles. Scripta Materialia 65 (8):652-655
2. Qu NS, Zhu D, Chan KC (2006) Fabrication of Ni–CeO_2 nanocomposite by electrodeposition. Scripta Materialia 54 (7):1421-1425
3. Naser J, Riehemann W, Ferkel H (1997) Dispersion hardening of metals by nanoscaled ceramic powders. Materials Science and Engineering: A 234:467-469
4. Naser J, Ferkel H, Riehemann W (1997) Grain stabilisation of copper with nanoscaled Al_2O_3 powder. Materials Science and Engineering: A 234:470-473
5. Nachum S, Fleck NA, Ashby MF, Colella A, Matteazzi P (2010) The microstructural basis for the mechanical properties and electrical resistivity of

nanocrystalline Cu–Al_2O_3. Materials Science and Engineering: A 527 (20):5065-5071
6. Mukhtar A, Zhang DL, Kong C, Munroe P (2010) Consolidation of ultrafine-grained Cu powder and nanostructured Cu–(2.5–10) vol% Al_2O_3 composite powders by powder compact forging. Journal of Materials Science 45 (17):4594-4605
7. Kudashov D, Baum H, Martin U, Heilmaier M, Oettel H (2004) Microstructure and room temperature hardening of ultra-fine-grained oxide-dispersion strengthened copper prepared by cryomilling. Materials Science and Engineering: A 387:768-771
8. Guduru RK, Scattergood RO, Koch CC, Murty KL, Guruswamy S, McCarter MK (2006) Mechanical properties of nanocrystalline Fe–Pb and Fe–Al_2O_3. Scripta Materialia 54 (11):1879-1883
9. Grant N, Zwilsky K (1961) Dispersion strengthening in the copper-alumina system. AIME 221 (2):371-377
10. Biselli C, Morris DG, Randall N (1994) Mechanical alloying of high-strength copper alloys containing TiB_2 and Al_2O_3 dispersoid particles. Scripta Metallurgica 30 (10):1327-1332
11. Rajkovic V, Bozic D, Jovanovic MT (2010) Effects of copper and Al_2O_3 particles on characteristics of Cu–Al_2O_3 composites. Materials & Design 31 (4):1962-1970
12. Srivatsan TS, Narendra N, Troxell JD (2000) Tensile deformation and fracture behavior of an oxide dispersion strengthened copper alloy. Materials & Design 21 (3):191-198
13. Lloyd DJ (1994) Particle reinforced aluminium and magnesium matrix composites. International Materials Reviews 39 (1):1-23
14. Lloyd DJ (1991) Aspects of fracture in particulate reinforced metal matrix composites. Acta Metallurgica 39 (1):59-71
15. Groza J (1992) Heat-resistant dispersion-strengthened copper alloys. Journal of Materials Engineering and Performance 1 (1):113-121
16. Ďurišin J, Ďurišinová K, Orolínová M, Saksl K (2004) Effect of the MgO particles on the nanocrystalline copper grain stability. Materials Letters 58 (29):3796-3801
17. Besterci M (1994) Structure analysis of dispersion strengthening. Scripta Metallurgica 30 (9):1145-1149
18. Koch C (2003) Optimization of strength and ductility in nanocrystalline and ultrafine grained metals. Scripta Materialia 49 (7):657-662
19. Ungár T, Dragomir I, Révész Á, Borbély A (1999) The contrast factors of dislocations in cubic crystals: the dislocation model of strain anisotropy in practice. Journal of Applied Crystallography 32 (5):992-1002
20. Williamson GK, Hall WH (1953) X-ray line broadening from filed aluminium and wolfram. Acta Metallurgica 1 (1):22-31
21. Zhao YH, Lu K, Zhang K (2002) Microstructure evolution and thermal properties in nanocrystalline Cu during mechanical attrition. Physical Review B 66 (8):085404
22. Williamson G, Smallman R (1956) III. Dislocation densities in some annealed and cold-worked metals from measurements on the X-ray debye-scherrer spectrum. Philosophical Magazine 1 (1):34-46
23. Champion Y, Langlois C, Guérin-Mailly S, Langlois P, Bonnentien JL, Hÿtch MJ (2003) Near-perfect elastoplasticity in pure nanocrystalline copper. Science 300

(5617):310-311

24. Hansen N, Ralph B (1982) The strain and grain size dependence of the flow stress of copper. Acta Metallurgica 30 (2):411-417

25. Benson DJ, Fu HH, Meyers MA (2001) On the effect of grain size on yield stress: extension into nanocrystalline domain. Materials Science and Engineering: A 319:854-861

26. Dieter GE (1976). Mechanical Metallurgy, McGraw-Hill, New York:pp.219-231

27. Nadkarni AV (1984). Dispersion strengthened copper: properties and applications, SCM Metal Products, Cleveland, Ohio:pp.77-101

28. Balogh L, Ungár T, Zhao Y, Zhu YT, Horita Z, Xu C, Langdon TG (2008) Influence of stacking-fault energy on microstructural characteristics of ultrafine-grain copper and copper–zinc alloys. Acta Materialia 56 (4):809-820

Chapter Five

Microstructures and Tensile Properties of Ultrafine Structured Cu-5vol.%Al2O3 Nanocomposite Synthesized by Powder Compact Extrusion at Different Temperatures

5.1 Introduction

Bulk ultrafine structured metal matrix nanocomposites (MMNCs) combine grain boundary strengthening, ceramic nanoparticles strengthening, as well as other strengthening mechanisms applicable to conventional metals such as solution hardening, strain hardening and precipitate hardening, and thus have the potential of offering high strength while retaining good ductility. The established favorable effect of ceramic nanoparticles on stabilizing the microstructures of ultrafine grained metal matrix [1-7] through the Zener pinning of grain boundaries allow these materials to be processed and used at elevated temperatures without totally losing the ultrafine structures which are critical to maintaining the grain boundary strengthening effect. When ultrafine structured MMNCs are fabricated by thermomechanical consolidation of nanostructured MMNC powders, there is an additional microstructural factor which can play a critical role in determining the mechanical properties of the bulk solid materials. This factor is the interparticle atomic bonding.

Powder compact extrusion is one of the thermomechanical powder consolidation techniques which has been widely used in fabricating bulk ultrafine structured MMNCs from nanostructured MMNC powders which are often produced by high energy mechanical milling of a mixture of metal powder and ceramic nanopowder. It has been well established that one of the key process parameters, the extrusion temperature, can have a significant effect on the matrix microstructure such as grain

sizes, the nanoparticle size, and the level of interparticle atomic bonding, all of which can lead to changes to mechanical properties of the materials reflected by strength and ductility. By changing the extrusion temperature, ultrafine structured MMNC samples with different matrix microstructures, different sizes of ceramic nanoparticles and different levels of interparticle atomic bonding can be fabricated. Studying the microstructures and mechanical properties of these samples systematically can allow us to get important outcomes for research on ultrafine structured MMNCs. One outcome is that it can elucidate the effect of extrusion temperature on the microstructure, level of interparticle bonding and mechanical properties of the ultrafine structured MMNCs, and thus can give an indication of the optimum range of extrusion temperatures for fabricating ultrafine structured MMNCs with desirable mechanical properties. The other outcome is that this study allows correlation of microstructure, level of interparticle atomic bonding and mechanical properties which in turn reflects the underlying linkage between the microstructure, level of atomic bonding and mechanical properties.

A number of studies on ultrafine structured MMNCs made by consolidation of nanostructured MMNC powders have shown that ceramic nanoparticles can substantially enhance the strength and thermal stability of materials by interacting with dislocations and inhibiting the migration of grain boundaries [8-11]. For example, an ultrafine structured Mo-0.6wt.% La_2O_3 nanocomposite with La_2O_3 nanoparticles uniformly distributed within ultrafine Mo grains had a yield strength value of 813 MPa, which is 418 MPa higher than that of conventional monolithic Mo [8]. The microstructure and hardness of oxide dispersion strengthened (ODS) ultrafine structured ferritic steel annealed in the temperature range 650-1350°C for 1h was found to remain stable at temperatures up to 1250°C [10]. In this study, bulk ultrafine structured MMNC samples with different microstructures, different sizes and volume fractions of Al_2O_3 nanoparticles and different levels of interparticle atomic bonding were fabricated by consolidating a nanostructured Cu-5vol.%Al_2O_3 MMNC powder by powder compact extrusion at temperatures ranging from 300 to 900°C.

Subsequently, the microstructure and mechanical properties of these samples were investigated in detail to determine the influence of extrusion temperature on their microstructures and room temperature tensile properties and establish the correlation between the matrix microstructure, Al_2O_3 nanoparticle size and volume fraction, interparticle atomic bonding and mechanical properties. The contributions of different strengthening mechanisms to the strength of the ultrafine structured MMNCs, different superposition models of basic strengthening mechanisms to the prediction of the strength of samples and the influence of the key microstructural and interparticle atomic bonding factors on the tensile ductility of the material are discussed.

5.2 Results

5.2.1 Microstructure

TEM bright field and STEM micrographs shown in Figures 5.1 and 5.2 illustrate the microstructures of the Cu matrix of the ultrafine structured Cu-5vol.%Al_2O_3 nanocomposite samples extruded at four temperatures ranging from 300-900°C. It can be seen clearly that the microstructure of the ultrafine structured Cu matrix becomes coarser as the extrusion temperature increases. The ultrafine structured Cu-5vol.%Al_2O_3 nanocomposite samples had a high density of dislocations in the Cu grains as indicated by their heavy contrast in the TEM bright field images (Figure 5.1).

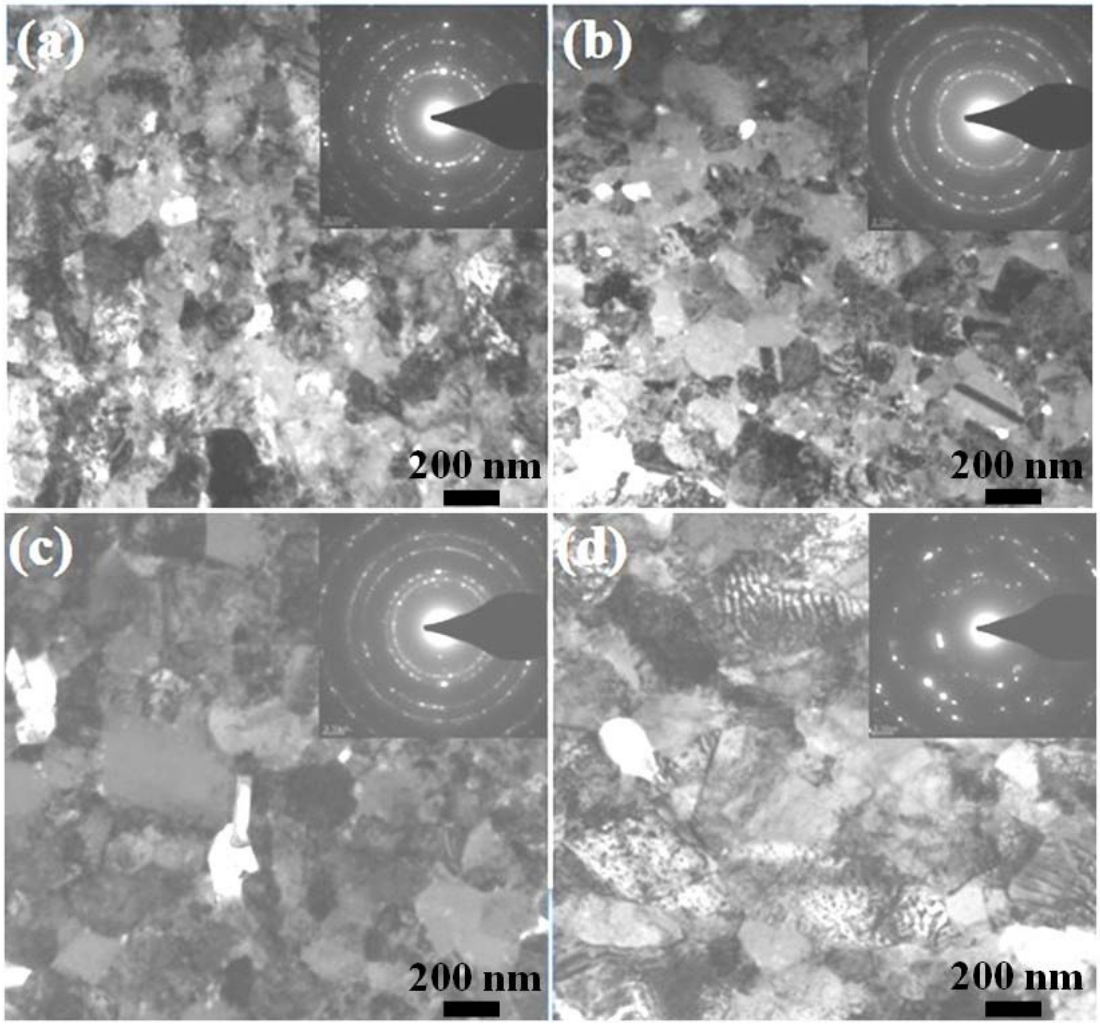

Figure 5.1: TEM bright field micrographs and corresponding SAED patterns (insets) of the ultrafine structured Cu-5vol.%Al_2O_3 nanocomposite samples extruded at different temperatures: (a) 300°C, (b) 500°C, (c) 700°C and (d) 900°C.

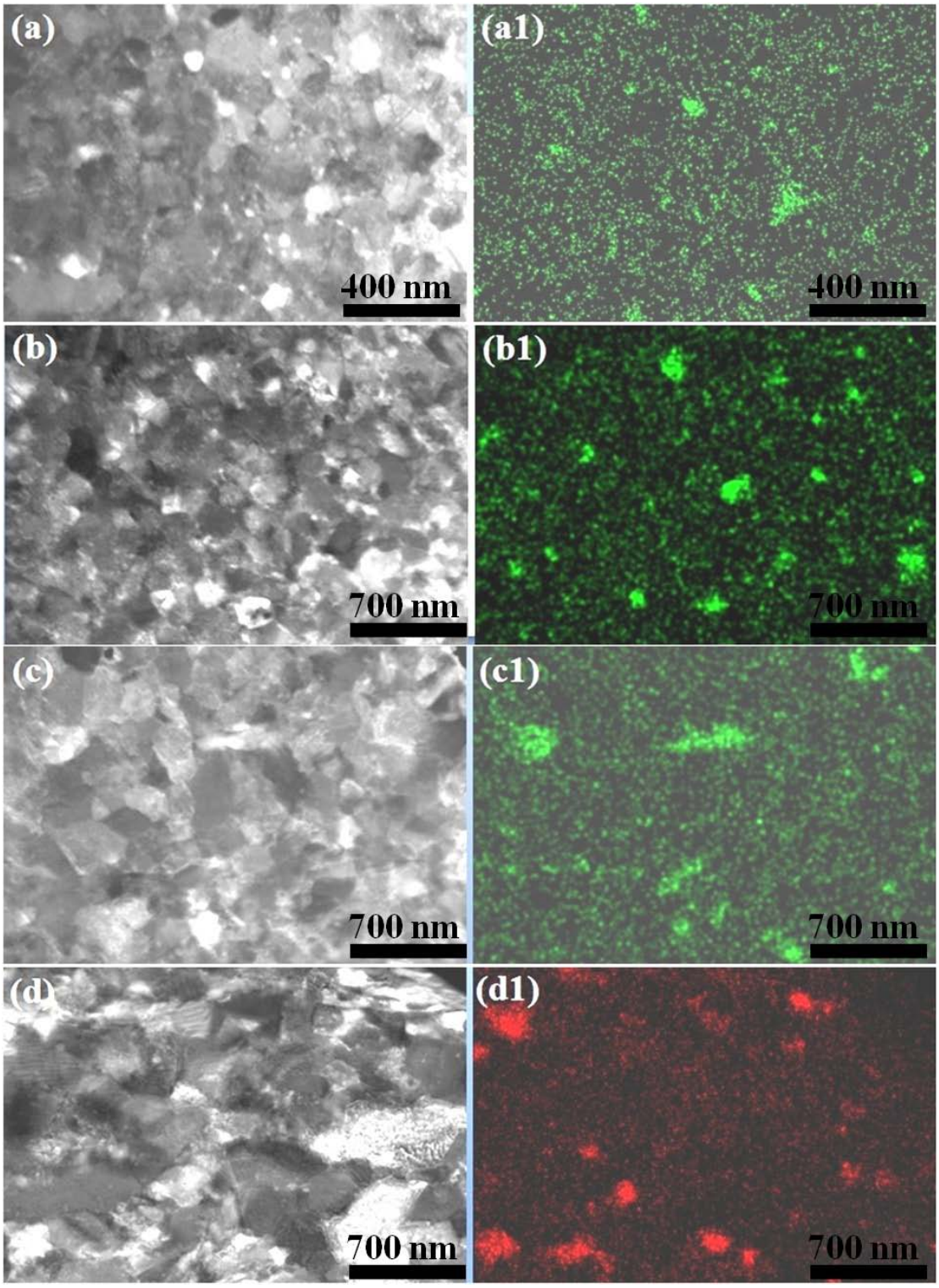

Figure 5.2: STEM micrographs ((a)-(d)) and EDX Al elemental maps ((a1)-(d1) of the ultrafine structured Cu-5vol.%Al_2O_3 nanocomposite samples extruded at different temperatures: (a) and (a1) 300°C; (b) and (b1) 500°C; (c) and (c1) 700°C and (d) and (d1) 900°C.

The Cu grain size distributions of the ultrafine structured Cu-5vol.%Al_2O_3 nanocomposite samples extruded at 300, 500, 700 and 900°C, shown in Figure 5.3,

demonstrate that the extruded samples have a wide range of grain sizes ranging from nanometer scale to submicrometer scale, and the sizes of the majority of Cu grains in the extruded samples are in the range 100-500 nm. Figure 5.3 also shows that the volume fraction of the nanometer sized Cu grains in the extruded sample decreases when the extrusion temperature increases, suggesting that grain growth occurs during the heating and extrusion of the powder compacts.

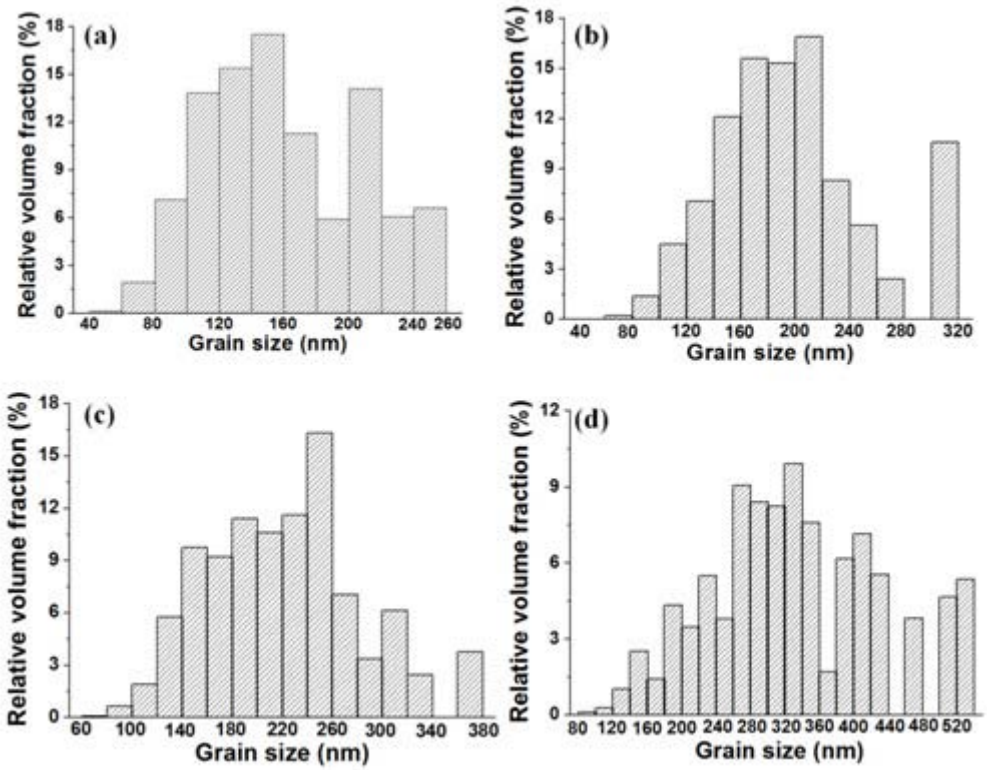

Figure 5.3: Cu grain size distributions of the ultrafine structured Cu-5vol.%Al_2O_3 nanocomposite samples extruded at (a) 300°C, (b) 500°C, (c) 700°C and (d) 900°C, respectively.

Figure 5.4 shows the mean grain size of Cu matrix of the ultrafine structured Cu-5vol.%Al_2O_3 nanocomposite samples as a function of extrusion temperature from 300 to 900°C. It shows clearly that the mean grain size of the Cu matrix increases with increasing extrusion temperature, and there is a critical temperature of 800°C below which the grain growth of Cu is limited, with the mean grain size of Cu increasing slowly from 132 and 204 nm between extrusion temperatures of 300 to 800°C. However, increasing the extrusion temperature from 800 to 900°C, the mean

grain size of the Cu matrix increases dramatically 204 to 263 nm.

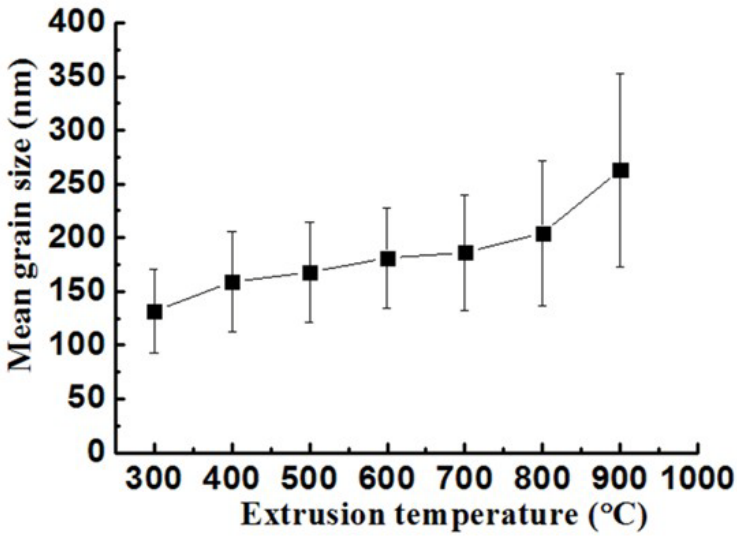

Figure 5.4: The mean grain sizes of the Cu matrix of the ultrafine structured Cu-5vol.%Al_2O_3 nanocomposite samples as a function of extrusion temperature.

As shown in Figures 5.2(a1-d1), the EDX Al elemental maps show that Al_2O_3 nanoparticles coarsen and their volume fraction increases with increasing the extrusion temperature. Such coarsening results in a clear increase of the relative volume fraction of Al_2O_3 nanoparticles with sizes larger than 100 nm from 7.7 to 82.9% with the increase of the extrusion temperature from 300 to 900°C, as shown in Figures 5.5-5.7. Furthermore, the volume fraction of Al_2O_3 nanoparticles in the ultrafine structured Cu-5vol.%Al_2O_3 nanocomposite samples increases progressively from 0.75 to 4% with increasing the extrusion temperature from 300 to 900°C. The fact that the measured volume fractions of Al_2O_3 nanoparticles in all ultrafine structured Cu-5vol.%Al_2O_3 nanocomposite samples are below the nominal value of 5vol.% indicates that there is still a fraction of Al_2O_3 nanoparticles being dissolved in the ultrafine structured Cu matrix after extrusion. The volume fraction of dissolved Al_2O_3 in the sample extruded at 300°C was 4.25%, suggesting that the majority of Al_2O_3 nanoparticles added to the initial powder mixture were dissolved during high energy mechanical milling (HEMM). The decrease of the volume fraction of dissolved Al_2O_3 from 4.25 to 1% with increasing the extrusion temperature from 300 to 900°C

suggests that the dissolved Al_2O_3 precipitates out during the induction heating and extrusion, and the amount of Al_2O_3 precipitating out increases significantly with increasing the extrusion temperature.

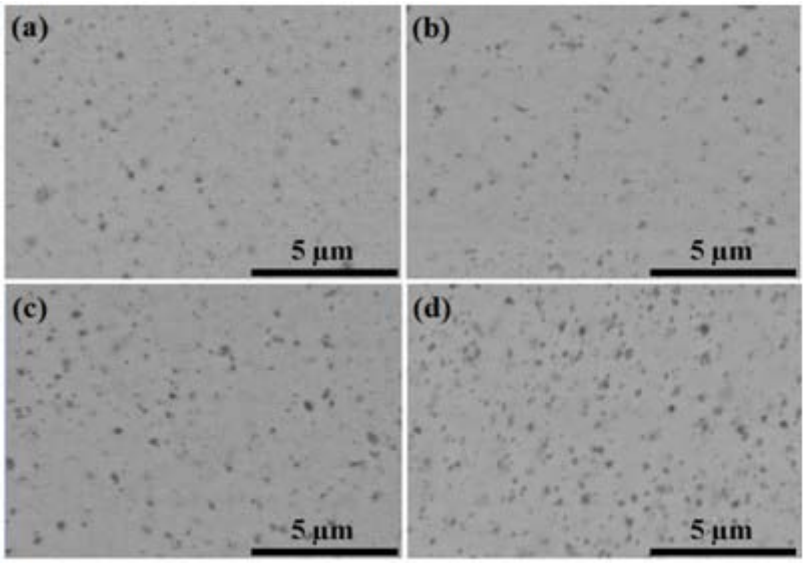

Figure 5.5: SEM backscattered electron images showing the Al_2O_3 nanoparticles in the ultrafine structured Cu-5vol.%Al_2O_3 nanocomposite samples extruded at different temperatures: (a) 300°C; (b) 500°C; (c) 700°C and (d) 900°C.

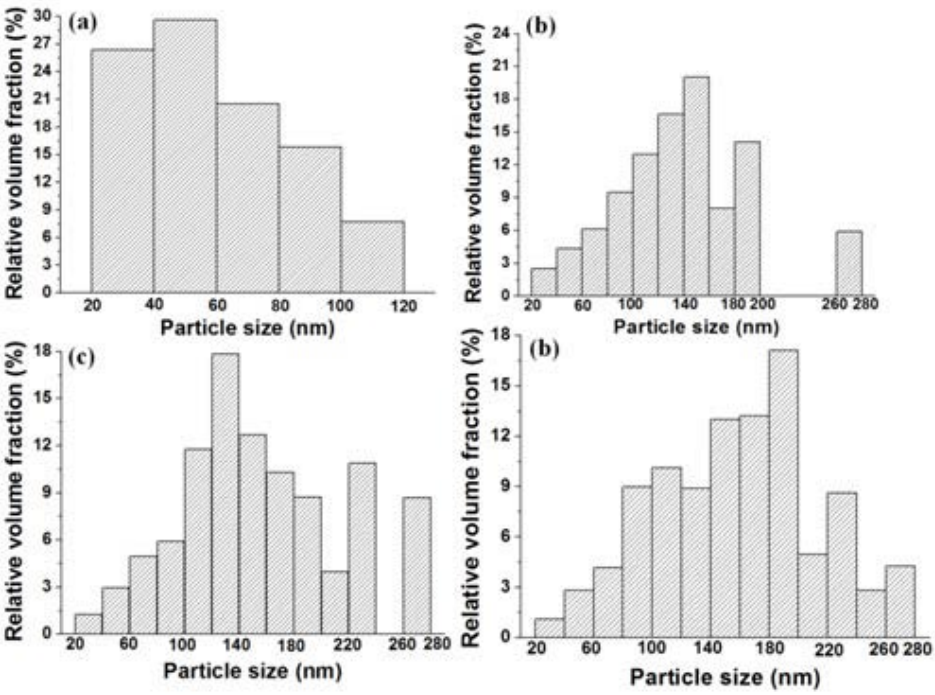

Figure 5.6: The size distributions of the Al_2O_3 nanoparticles in the ultrafine structured Cu-5vol.%Al_2O_3 nanocomposite samples extruded at (a) 300°C, (b) 500°C, (c) 700°C

and (d) 900°C, respectively.

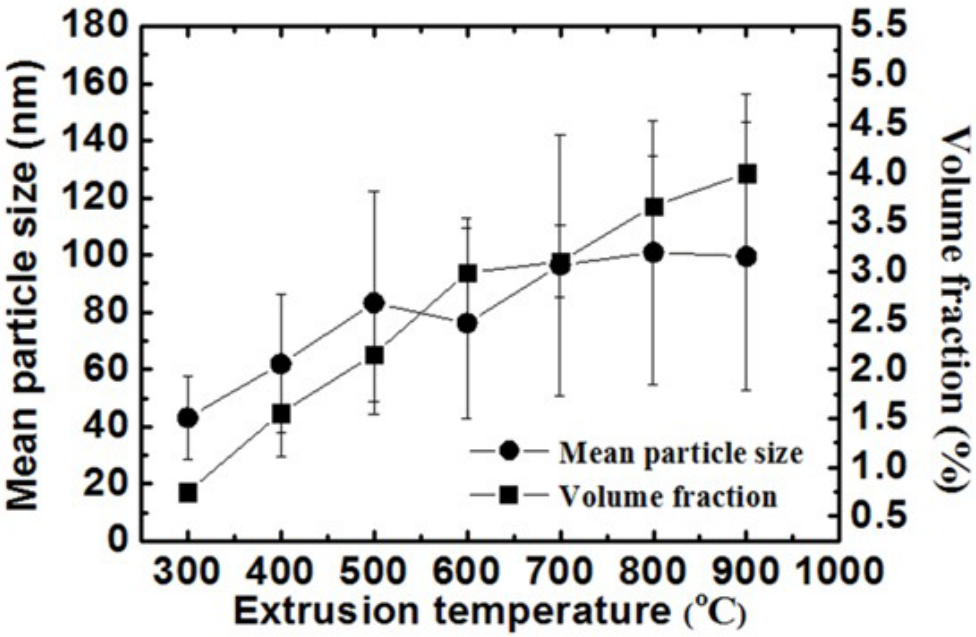

Figure 5.7: The mean particle size and volume fraction of the Al_2O_3 nanoparticles in the ultrafine structured Cu-5vol.%Al_2O_3 nanocomposite samples as functions of extrusion temperature.

The XRD patterns of the extruded samples shown in Figure 5.8 show that the lattice parameter of the Cu matrix is not affected by the difference in the volume fraction of the Al_2O_3 nanoparticles dissolved in the Cu matrix. This indicates that the vast majority of the Al_2O_3 in nanostructured Cu matrix of Cu-5vol.%Al_2O_3 nanocomposite powder particles produced by HEMM may exist in Al^{3+}/O^{2-} clusters which are too small to be resolved by TEM, STEM and SEM. This speculation is in agreement with the experimental observations made by Dai et al. [12] and Toualbi et al. [13] which show the Y_2O_3 from dissolution of initially added Y_2O_3 nanoparticles in the ferritic matrix after 48 or 100 h of HEMM exist in the form of clusters of very small sizes. It appears that the Al_2O_3 nanoparticles in the extruded samples tend to be distributed at the grain boundaries of the Cu matrix, as indicated by white dots shown in TEM and STEM images (Figures 5.1 and 5.2).

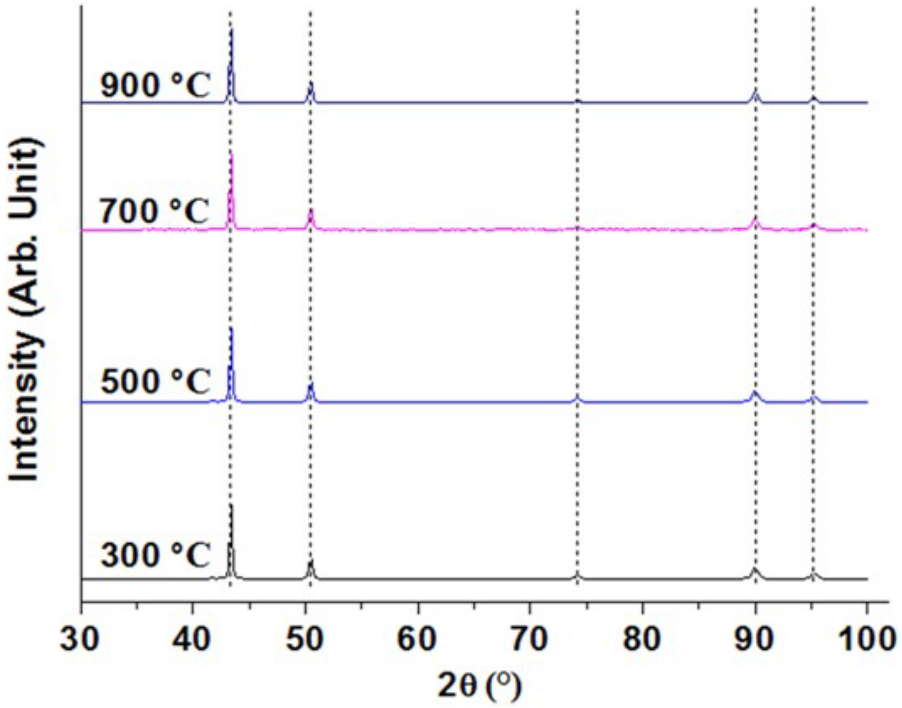

Figure 5.8: XRD patterns of the ultrafine structured Cu-5vol.%Al_2O_3 nanocomposite samples extruded at 300, 500, 700 and 900°C, respectively.

5.2.2 Effect of the Extrusion Temperature on Mechanical Properties

As shown in Figure 5.9, the Vickers microhardness of ultrafine structured Cu-5vol.%Al_2O_3 nanocomposite samples decreases almost linearly from 2.1 to 1.8 GPa as the extrusion temperature increases from 300 to 900°C.

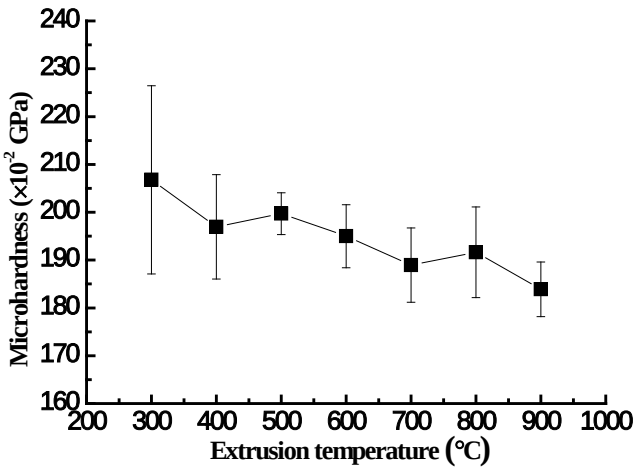

Figure 5.9: The microhardness of the ultrafine structured Cu-5vol.%Al_2O_3 nanocomposite samples as a function of extrusion temperature.

As shown by the engineering tensile stress-strain curves and the images of the tensile test specimens shown in Figure 5.10(a), the tensile specimens cut from the samples extruded at 500°C or lower fractured prematurely before reaching their UTS and the fracture occurred at the corners of the specimens. On the other hand, the specimens cut from the samples extruded at temperatures of 700°C or higher fractured after reaching the UTS and the fracture occurred well within the gauge length of the tensile test specimens. It is apparent that the tensile test specimens cut from samples extruded at higher temperatures have a greater plastic strain to fracture with slightly decreased values of strength, as shown in Figure 5.10(a). Figure 5.10(b) shows the averaged tensile test results of the samples as functions of extrusion temperature in the range of 300-900°C. The samples extruded at temperatures ≤400°C failed prematurely before reaching their YS. Hence, the YS shown in Figure 5.10(b) are only for those samples extruded at T≥500°C. As shown in Figure 5.10(b), the YS of the samples extruded first decreased from 517 to 466 MPa with increasing the extrusion temperature from 500 to 800°C, and then increase slightly from 466 to 472 MPa when the extrusion temperature is increased to 900°C. It is noted that the samples extruded at temperatures ≤500°C do not have UTS due to early fracture and only have fracture strength (FS). For the samples extruded at temperatures ≥600°C, the value of the UTS changed little with increasing the extrusion temperature from 600 to 900°C and thus had a small range of 546-564 MPa. On the other hand, the plastic strain to fracture of the extruded samples increased almost linearly from 0.76 to 2.48% when the extrusion temperature increased from 500 to 800°C and then increased rapidly to 5.82% with increasing the extrusion temperature from 800 to 900°C, as shown in Figures 5.10(a) and (b).

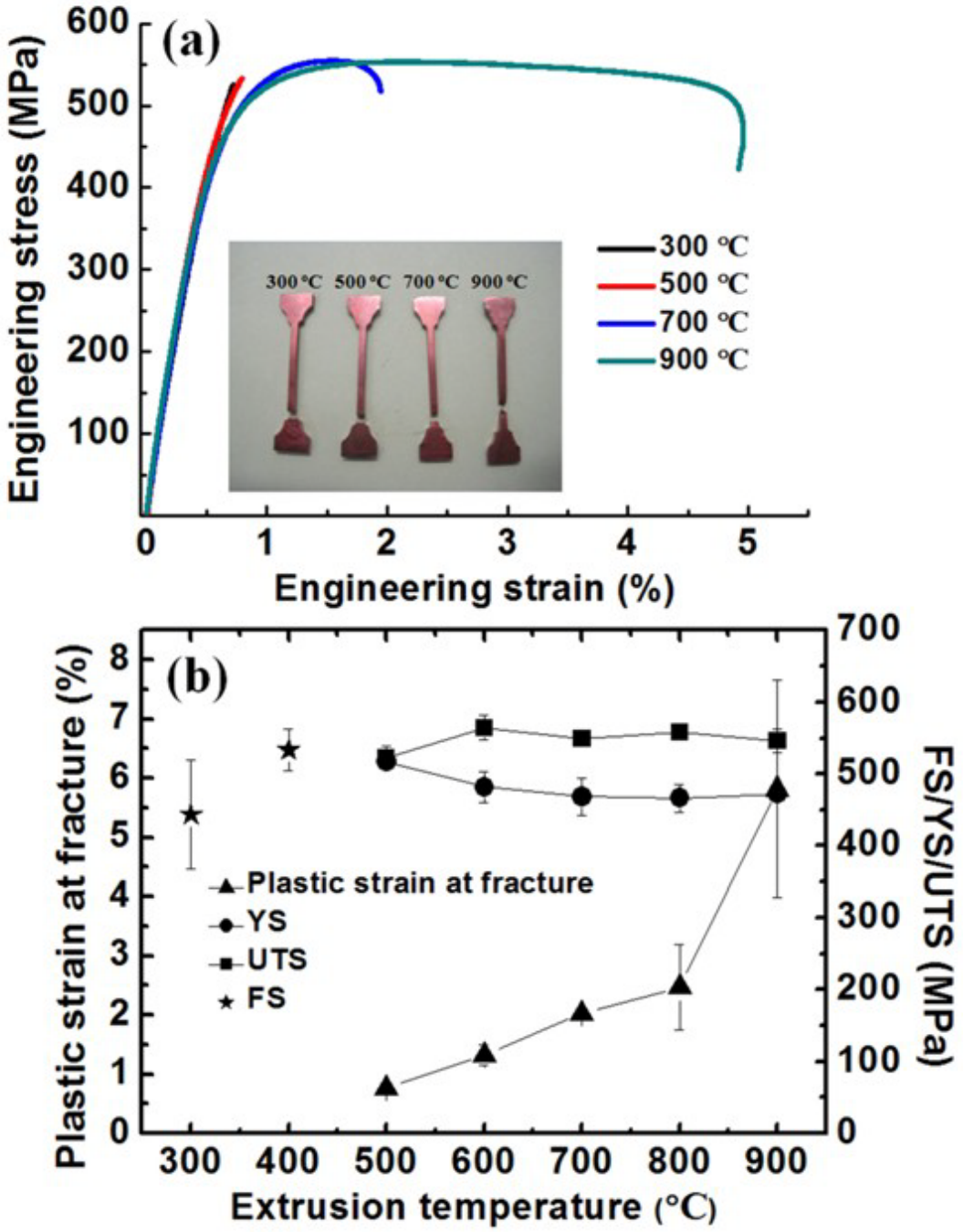

Figure 5.10: (a) Engineering tensile stress-strain curves of the ultrafine structured Cu-5vol.%Al_2O_3 nanocomposite samples extruded at 300, 500, 700 and 900°C, (the examples of fractured specimens cut from different extruded samples are shown in the inset); (b) FS, YS, UTS and plastic strain to fracture of the ultrafine structured Cu-5vol.%Al_2O_3 nanocomposite samples as functions of extrusion temperature.

As shown by the images of the tensile test specimens in Figure 5.10(a), the fracture of the specimens cut from samples extruded at 300 and 500°C occurred near the corners where the width of the specimen changes, while the tensile test specimens cut from samples extruded at 700 and 900°C occurred at locations well within the gauge length of the specimens. This indicates that the former fractures through cracks nucleated from surface corners where stress concentration occurs, while the latter fractures through formation of cavities inside the specimens. Indeed the top view of the fractured specimens (Figure 5.11) shows clearly that the fracture of the tensile test specimens cut from the samples extruded at 300 and 500°C initiated from the side surfaces of the specimens, while the fracture of the tensile test specimens cut from the samples extruded at 700 and 900°C initiated from cavities formed inside the specimens.

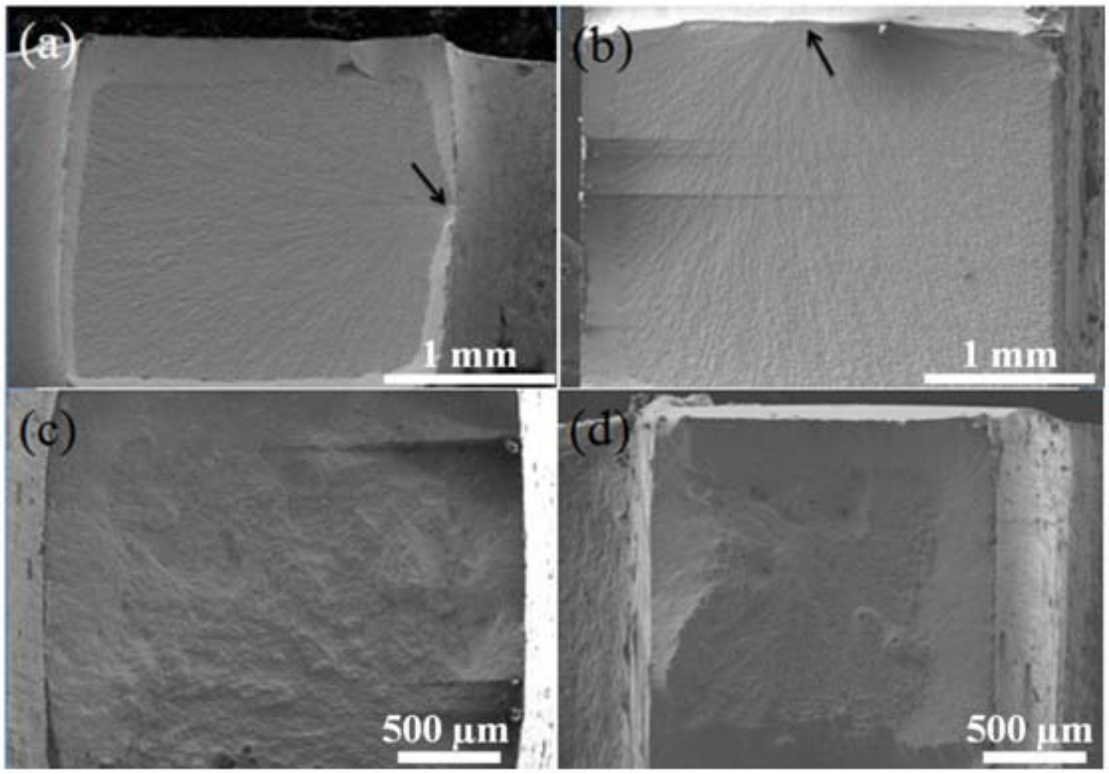

Figure 5.11: Top views of the fractured tensile test specimens cut from the ultrafine structured Cu-5vol.%Al_2O_3 nanocomposite samples extruded at (a) 300, (b) 500, (c) 700 and (d) 900°C, respectively.

The low magnification SEM images of the fracture surfaces of the tensile test

specimens (Figure 5.12) show that the fracture surfaces of the tensile test specimens cut from samples extruded at 300 and 500°C are fairly smooth and lack large sized dimples, while the fracture surfaces of the tensile test specimens cut from samples extruded at 700 and 900°C are fairly rough, and contain large sized dimples and secondary cracks (indicated by arrows in Figures 5.12(a) and (b)). On the other hand, high magnification SEM images of the fracture surfaces of the tensile test specimens (Figure 5.13) show that the fracture surfaces of the tensile test specimens cut from samples extruded at 300 and 500°C are fairly rough, consisting of micrometer sized dimples and submicrometer sized features of intergranular fracture, while the fracture surfaces of the tensile test specimens cut from samples extruded at 700 and 900°C are fairly smooth, only consisting of submicrometer sized features of intergranular fracture.

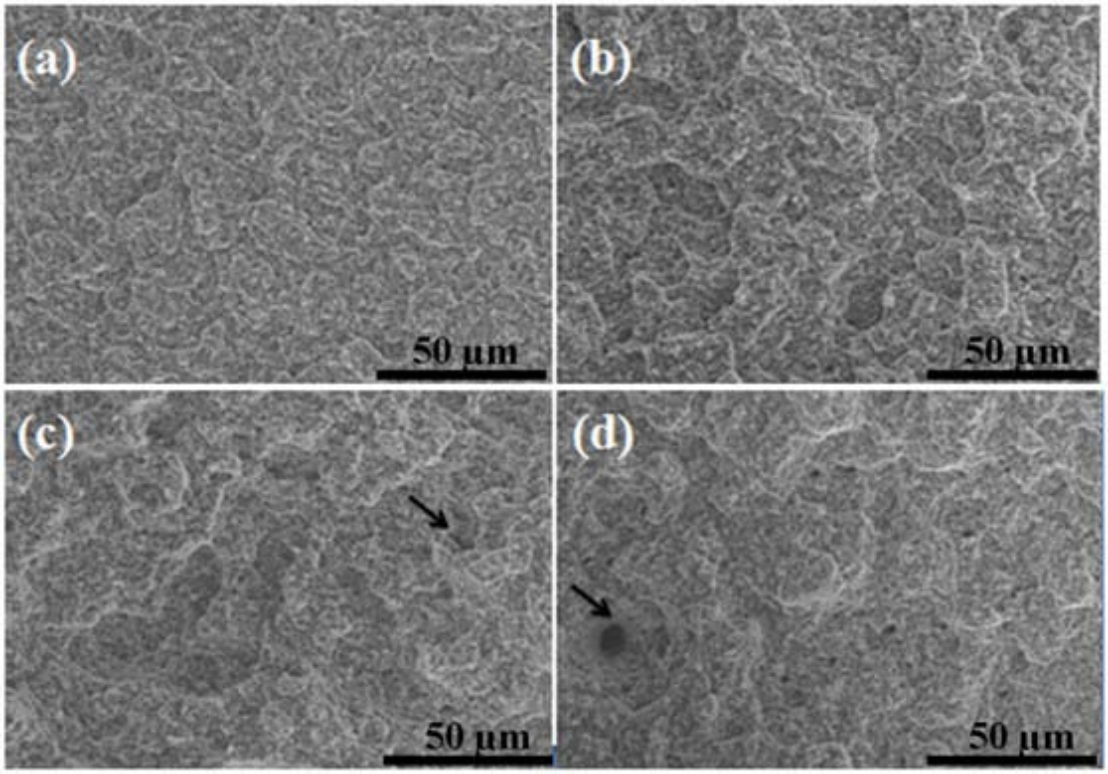

Figure 5.12: Low magnification SEM images of fracture surfaces of the tensile test specimens cut from the ultrafine structured Cu-5vol.%Al_2O_3 nanocomposite samples extruded at (a) 300°C, (b) 500°C, (c) 700°C and (d) 900°C, respectively.

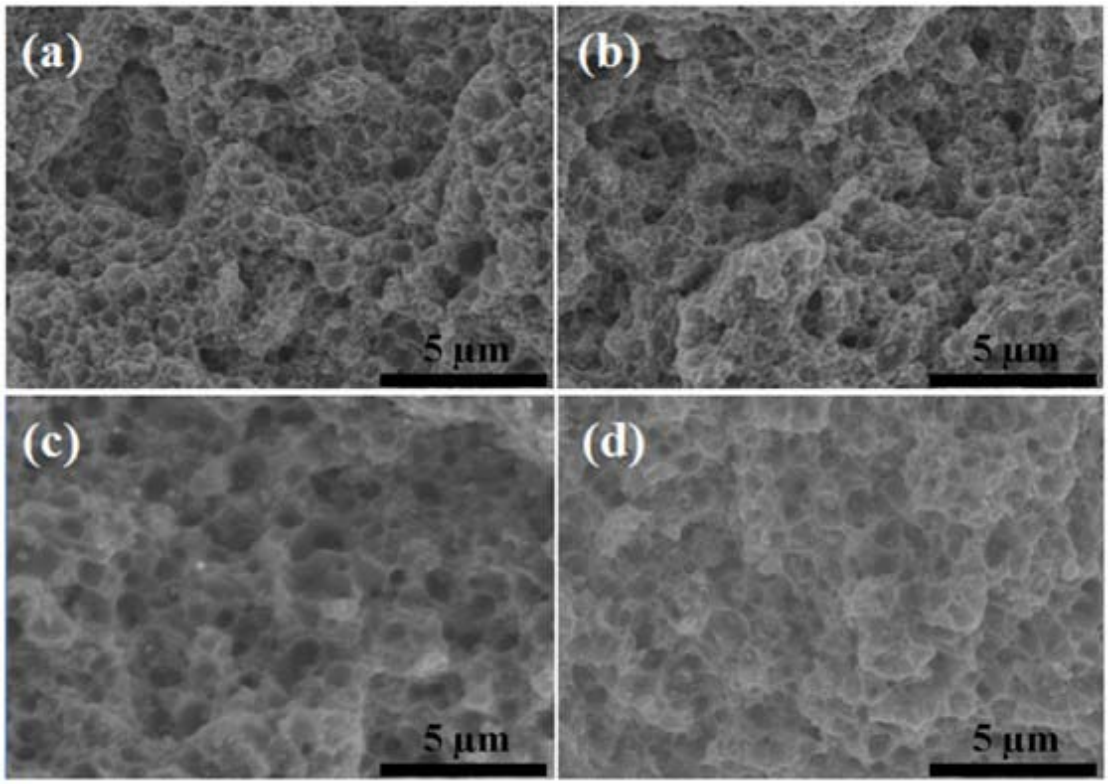

Figure 5.13: High magnification SEM images of the fracture surfaces of the tensile test specimens cut from the ultrafine structured Cu-5vol.%Al_2O_3 nanocomposite samples extruded at (a) 300°C, (b) 500°C, (c) 700°C and (d) 900°C, respectively.

SEM examination of the longitudinal sections of the tensile test specimens near their fracture surfaces (Figure 5.14) failed to reveal any cavities formed by separation of the powder particles under tensile stress. However, two distinct crack paths were observed for the tensile test specimens. The tensile test specimens cut from the samples extruded at 300 and 500°C had fairly straight crack paths, whereas the crack paths were curved for the tensile test specimens cut from the samples extruded at 700 and 900°C and the secondary cracks were also found. Here, the relatively straight crack path means that the specimen has a low resistance to crack propagation, leading to a low fracture toughness. On the other hand, the relatively curved crack path with the secondary cracks could offer a high resistance to crack propagation, leading to a high fracture toughness.

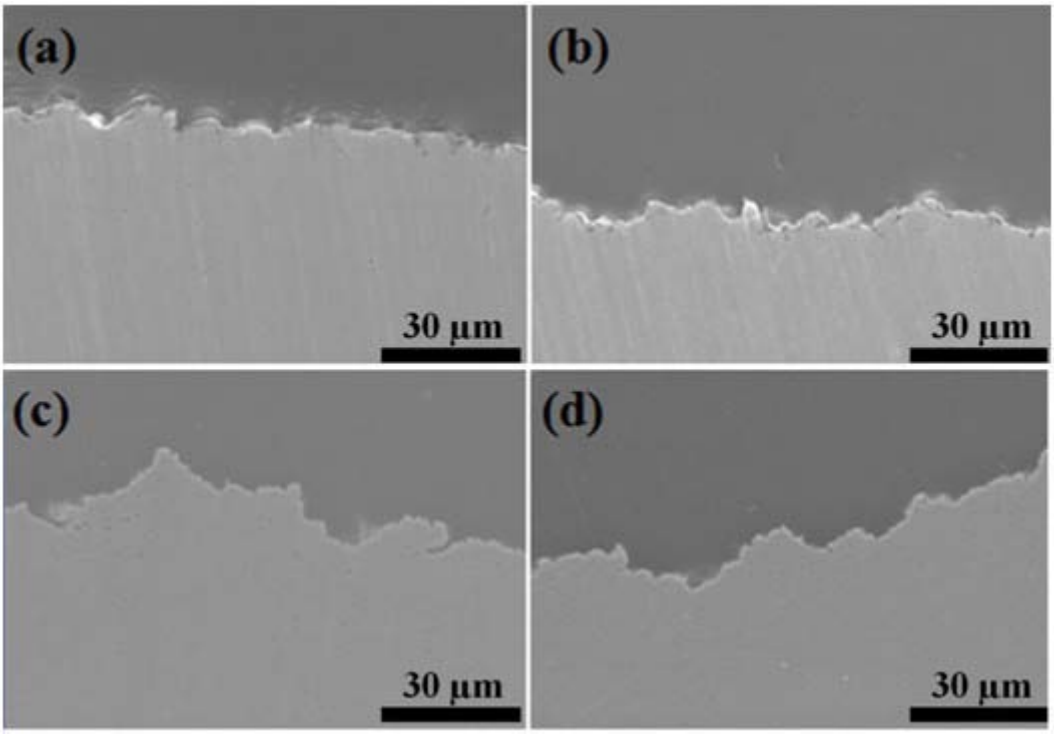

Figure 5.14: Longitudinal sections of the fractured tensile test specimens cut from the ultrafine structured Cu-5vol.%Al_2O_3 nanocomposite samples extruded at (a) 300°C, (b) 500°C, (c) 700°C and (d) 900°C, respectively.

5.3 Discussion

5.3.1 Contributions of Different Strengthening Mechanisms

Based on the published literature [14-16], the value of the yield strength, σ_y, of an ultrafine structured metal strengthened with homogeneously distributed second phase nanoparticles mainly depends on grain boundary strengthening, $\Delta\sigma_{gb}$, nanoparticle strengthening, $\Delta\sigma_{Or}$, and strain hardening, $\Delta\sigma_{\rho}$. In this study, the yield strength of the ultrafine structured Cu-5vol.%Al_2O_3 nanocomposite samples is mostly determined by these three strengthening contributions as the basic strength of copper associated with lattice friction of dislocations, σ_0, is quite small being in the order of 5 MPa [17]. $\Delta\sigma_{gb}$ can be evaluated by using the Hall-Petch relationship which is expressed by the following equation [18-19]:

$$\Delta\sigma_{gb} = k_{HP} D^{-1/2} \quad (5\text{-}1),$$

where k_{HP} is the Hall-Petch coefficient being taken to be 0.112 MPa $m^{/2}$ [20] and D is mean grain size. Orowan strengthening ($\Delta\sigma_{Or}$) originates from the interaction of mobile dislocations with non-shearable nanoparticles resulting in the formation of Orowan loops [21] and can be evaluated by the equation as given below:

$$\Delta\sigma_{Or} = 0.13\frac{Gb}{\lambda}\ln\left(\frac{r}{b}\right) \quad (5\text{-}2),$$

where G is the shear modulus, b is the Burgers vector, λ is the inter-nanoparticle spacing and equal to $r\cdot\left(\frac{2\pi}{3f}\right)^{\frac{1}{2}}$ [22] (f is the volume fraction of nanoparticles and r is the mean radius of the nanoparticles). For Cu, G and b are 47.7 GPa and 0.256 nm [17], respectively. It is worth pointing out that only Al_2O_3 nanoparticles which can be resolved by SEM were considered to evaluate the strength increase caused by the Orowan mechanism. The strain hardening, $\Delta\sigma_{\rho}$, is from the interaction of sliding dislocations with the configurations of dislocations and can be estimated based on the Taylor equation [21]:

$$\Delta\sigma_{\rho} = M\alpha Gb\sqrt{\rho} \quad (5\text{-}3),$$

where M is the Taylor factor and 3.06 for copper [17], α is the strength coefficient of the dislocation network which can be taken to be 0.2 [14] and ρ is the dislocation density of the material prepared. The calculation procedure of the dislocation density was given in Chapter Three. Substitution of corresponding parameters and experimental data into the grain boundary strengthening, nanoparticle strengthening and strain hardening models allows us to obtain the contributions of different strengthening mechanisms of the ultrafine structured Cu-5vol.%Al_2O_3 nanocomposite samples as a function of extrusion temperature (Figure 5.15(a)). Clearly, the grain boundary strengthening is the most effective way in strengthening the ultrafine structured Cu-5vol.%Al_2O_3 nanocomposite sample compared with nanoparticle strengthening and strain hardening.

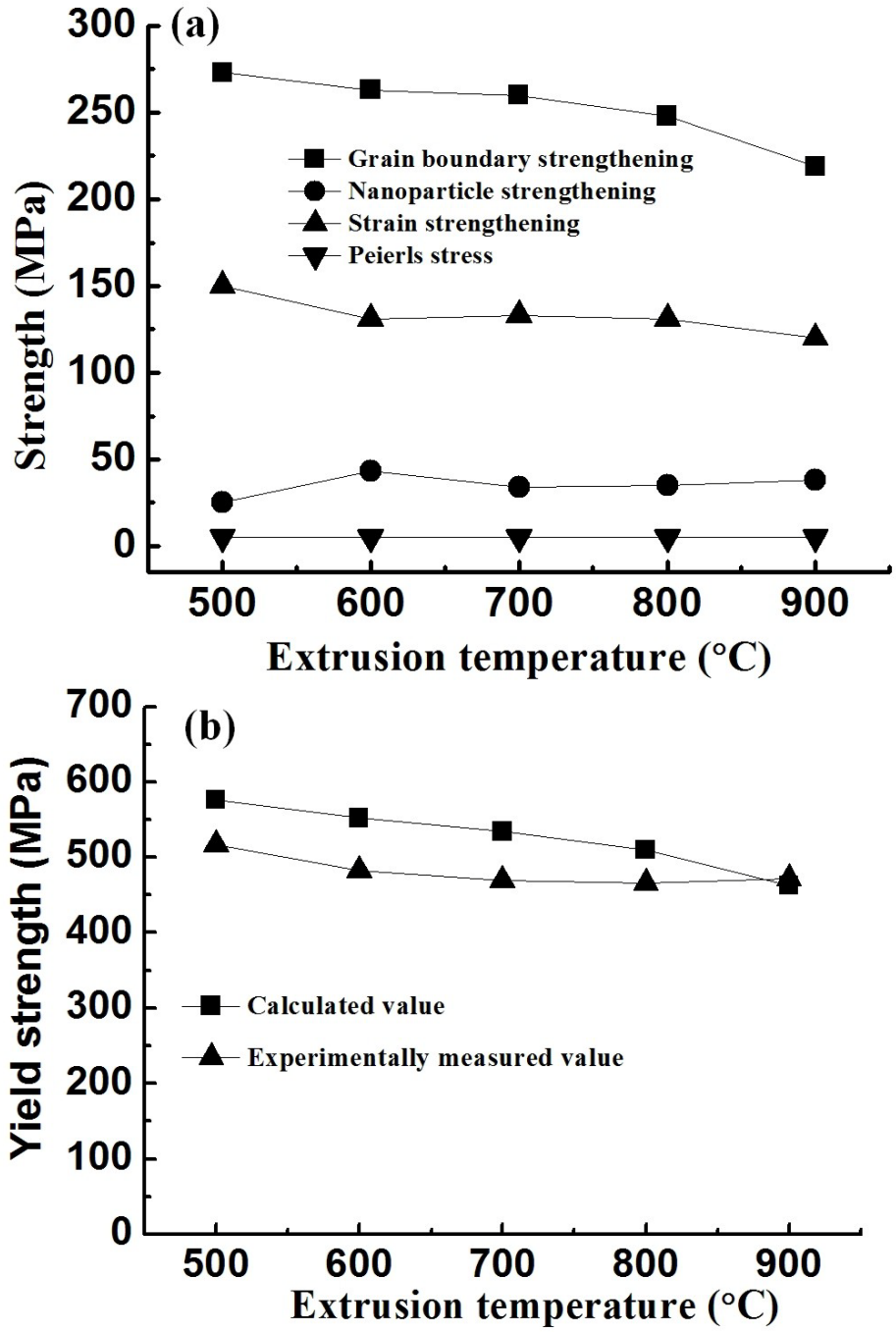

Figure 5.15: (a) Contributions of the three strengthening mechanisms of the ultrafine structured Cu-5vol.%Al_2O_3 nanocomposite samples as a function of extrusion temperature; (b) Calculated and experimentally measured values of yield strength of the extruded samples as a function of extrusion temperature.

The grain boundary strengthening, nanoparticle strengthening and strain hardening models are used to construct an equation to predict the yield strength of the ultrafine structured Cu-5vol.%Al_2O_3 nanocomposite samples. The constructed equation has the

following expression [23-25]:

$$\sigma_y = \sigma_0 + (\sigma_{gb}^k + \sigma_{np}^k + \sigma_\rho^k)^{1/k} \quad (5\text{-}4),$$

where k is an adjustable parameter depending on the strengthening mechanisms involved and normally within the range of 1-2. If there is no interaction between the involved strengthening mechanisms, a linear superposition of different strengthening mechanisms can be assumed to be valid, i.e., k=1 in Equation (5-4).

The yield strength calculation demonstrated that the calculated values are below experimentally measured values with a discrepancy being less than 90 MPa for the extruded samples (Figure 5.15(b)). It should be realized that those Al_2O_3 nanoparticles dissolved in the Cu matrix which cannot be resolved by SEM were not taken into account in the calculation of the Orowan strengthening contribution. The dissolved Al_2O_3 may exist as Al^{3+}/O^{2-} clusters. The fraction of the dissolved Al_2O_3 nanoparticles must interact with dislocations to further strengthen the matrix. Within clusters there is an extremely strong electric field which could generate a very large electrostatic force to inhibit dislocations cutting through. This effect would force a dislocation to bow out and leave a loop behind after passing through Al^{3+}/O^{2-} clusters. Consequently, it can be assumed that the dissolved Al_2O_3 nanoparticles which have a mean particle size of 10 nm interact with dislocations through the Orowan mechanism. The strengthening contribution from the dissolved Al_2O_3 nanoparticles to the overall strength of the extruded sample was estimated by using Equation (5-2) for each studied extrusion temperature and is presented in Table 5.1. As seen in Table 5.1, the sums of various strengthening contributions of the extruded ultrafine structured Cu-5vol.%Al_2O_3 nanocomposite samples show reasonable agreements with their experimental results. The agreement between the calculated strength and experimentally measured one reveals that the analysis on the contributions of different strengthening mechanisms plays a very significant role in linking the strength of an ultrafine structured metal matrix nanocomposite to its microstructural features and understanding its dominant strengthening contributions. Such information can be used

as a reference to tailor an ultrafine structured metal matrix nanocomposite with superior mechanical property.

Table 5.1 The values of different strengthening contributions, total calculated strength and the measured strength of ultrafine structured Cu-5vol.%Al_2O_3 nanocomposites extruded at T≥500°C.

Extrusion temperature (^{o}C)	Peierls force (MPa)	Dislocation contribution (MPa)	Resolved Al_2O_3 nanoparticles contribution (MPa)	Dissolved Al_2O_3 nanoparticles contribution (MPa)	Grain boundary contribution (MPa)	Total calculated Strength (MPa)	Measured strength (MPa)
500	5	150	25	123	273	576	517
600	5	131	43	110	263	552	482
700	5	133	34	102	260	534	469
800	5	131	35	91	248	510	466
900	5	120	38	80	219	462	472

5.3.2 Effect of Extrusion Temperature

It is known that the ductility of a bulk material consolidated from powders is associated with its densification level and interparticle bonding. In general, a full density and complete chemical bonding between powder particles can be achieved by the combination of large plastic flow and high temperature during consolidation. Previous studies [26-27] have shown that when the consolidation temperature is relatively low the ductility of the consolidated material increases with the increase of the consolidation temperature. The authors attributed this to the improvement of the interparticle bonding level. In this study, the tensile elongation at failure of ultrafine structured Cu-5vol.%Al_2O_3 nanocomposite samples increased with the increase of the extrusion temperature from 300 to 900°C (Figure 5.10). Due to poor interparticle bonding formed under 500°C, the samples extruded at temperatures ≤500°C fracture prematurely before the macroscopic yielding starts. The samples extruded in the

temperature range 600-800°C have comparable mean Cu grain sizes (Figure 5.4); however, their interparticle bonding is believed to be enhanced with the increase of the extrusion temperature. Accordingly, the enhancement of the interparticle bonding accounts for the increase of the elongation to fracture with the increase of the extrusion temperature for the samples extruded in the temperature range of 600-800°C. A rapid increase of the elongation to fracture was observed for the sample extruded at 900°C. For this sample, Al_2O_3 nanoparticles had very little effect in the dislocation storage during tensile testing as most of them resided on Cu grain boundaries. On the other hand, its Cu grains underwent significant coarsening which offer more room to accommodate plastic deformation. Furthermore, the level of the interparticle bonding of the extruded sample was expected to be further improved when the extrusion temperature is high up to 900°C. Hence, the substantial increase in ductility observed for the sample extruded at 900°C mainly comes from the grain growth of the Cu matrix (Figures 5.1, 5.2, 5.3 and 5.4) and improved interparticle bonding.

The fracture surfaces of the tensile test specimens cut from the extruded samples have irregular-shaped pits with sizes ranging from several to tens of micrometers comparable to the sizes of milled nanocomposite powder particles (Figure 2.4). Similar fracture features were also observed on the fracture surface of the cryomilled Al-10Ti-2Cu (in wt.%) alloy by Hayes et al. [28]. Such characteristics of the fracture surface support the speculation that the fracture path of materials produced under tensile stress is related to their interparticle bonding. According to the characteristic of powder particle boundaries regarding the interparticle bonding strength, two different fracture mechanisms which are illustrated by schematics shown in Figure 5.16 are proposed to describe the fracture behavior of ultrafine structured Cu-5vol.%Al_2O_3 nanocomposite samples extruded at different temperatures. Mechanism I illustrated in Figure 5.16(a) is applicable to the samples extruded at T≤500°C. For these samples, the powder particle boundaries have not transformed into grain boundaries through extrusion and the interparticle bonding strength is weak so that a fatal crack can be initiated by a surface flaw of the tensile test specimen due to lack of sufficient plastic

deformation to resist the crack formation. The presence of the crack results in the nucleation and growth of cavities at its tip and then the linkage of cavities ahead of the crack tip leads to the propagation of the crack and cause the failure of the samples. Mechanism II illustrated in Figure 5.16(b) is applicable to those samples extruded at temperatures ≥700°C where the surface defect is not able to act as a crack nucleation site because a complete transformation of powder particle boundaries into grain boundaries has been achieved, and the sample has a sufficiently high tolerance to the surface flaws. In this case, cavities first nucleate at grain boundary junctions and/or the matrix-particle interfaces where stress concentration occurs, and then grow, coalesce, and finally cause the fracture of the tensile test specimen.

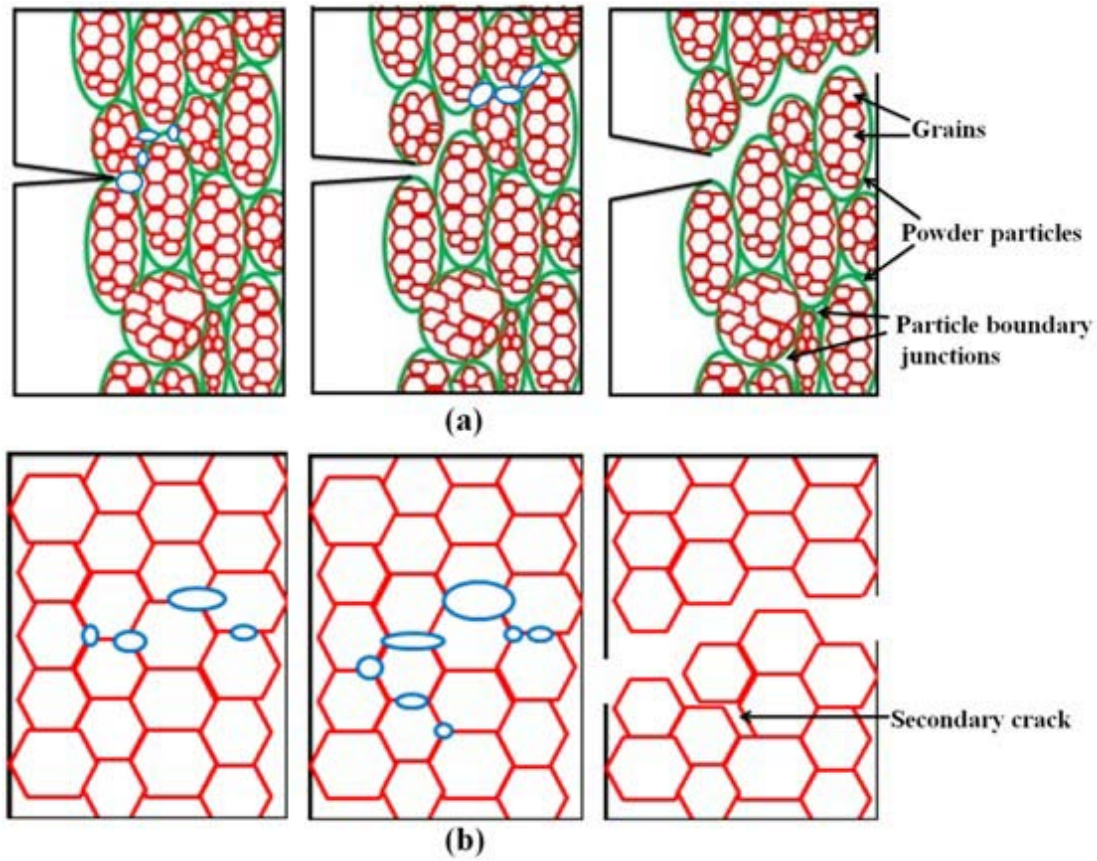

Figure 5.16: Schematics of the fracture mechanism of the tensile test specimens cut from the extruded ultrafine structured Cu-5vol.%Al_2O_3 nanocomposite samples. (a): the fracture mode of the samples extruded at T≤500°C; (b): the fracture mode of the samples extruded at T≥700°C.

5.4 Summary

The microstructures and tensile properties of ultrafine structured Cu-5vol.%Al_2O_3 nanocomposite samples extruded at temperatures in the range 300-900°C were systematically investigated in the present study and the following conclusions can be drawn:

(1) Cu grains, the sizes and volume fractions of Al_2O_3 nanoparticles and the levels of interparticle atomic bonding of ultrafine structured Cu-5vol.%Al_2O_3 nanocomposites increase with increasing extrusion temperature from 300 to 900°C;

(2) Grain boundary strengthening has the largest contribution to the strength of the extruded samples relative to the nanoparticle strengthening and strain hardening. The yield strength of the extruded samples calculated by using the linear model of $\sigma_y = \sigma_0 + \sigma_{gb} + \sigma_{np} + \sigma_\rho$ shows an appropriate agreement with the experimentally measured value;

(3) The tensile ductility of the samples is proportional to the extrusion temperature and associated with the interparticle atomic bonding and the microstructure of the Cu matrix. The ductility of the extruded samples is primarily determined by the interparticle bonding when T≤800°C; when T=900°C it is controlled by both the interparticle bonding and the microstructure of the Cu matrix.

5.5 References

1. Morris DG, Morris MA (1991) Microstructure and strength of nanocrystalline copper alloy prepared by mechanical alloying. Acta Metallurgica 39 (8):1763-1770
2. Schroth JG, Franetovic MV (1989) Mechanical alloying for heat-resistant copper alloys. Journal of the Minerals Metals & Materials Society (JOM) 41 (1):37-39
3. Nachum S, Fleck NA, Ashby MF, Colella A, Matteazzi P (2010) The microstructural basis for the mechanical properties and electrical resistivity of nanocrystalline Cu–Al_2O_3. Materials Science and Engineering: A 527 (20):5065-5071
4. Biselli C, Morris DG, Randall N (1994) Mechanical alloying of high-strength copper alloys containing TiB_2 and Al_2O_3 dispersoid particles. Scripta Metallurgica 30

(10):1327-1332
5. Marques MT, Livramento V, Correia JB, Almeida A, Vilar R (2005) Production of copper–niobium carbide nanocomposite powders via mechanical alloying. Materials Science and Engineering: A 399 (1):382-386
6. Lebedev AB, Pulnev SA, Kopylov VI, Burenkov YA, Vetrov VV, Vylegzhanin OV (1996) Thermal stability of submicrocrystalline copper and Cu-ZrO_2 composite. Scripta Materialia 35 (9):1077-1081
7. Lebedev AB, Pul'nev SA, Vetrov VV, Burenkov YA, Kopylov VI, Betekhtin KV (1998) Thermal stability of submicrocrystalline copper strengthened with HfO_2 nanoparticles in the temperature range 20–500 ^{o}C. Physics of the Solid State 40 (7):1155-1157
8. Liu G, Zhang GJ, Jiang F, Ding XD, Sun YJ, Sun J, Ma E (2013) Nanostructured high-strength molybdenum alloys with unprecedented tensile ductility. Nature Materials 12 (4):344-350
9. Zhang Z, Topping T, Li Y, Vogt R, Zhou Y, Haines C, Paras J, Kapoor D, Schoenung JM, Lavernia EJ (2011) Mechanical behavior of ultrafine-grained Al composites reinforced with B_4C nanoparticles. Scripta Materialia 65 (8):652-655
10. Oksiuta Z, Kozikowski P, Lewandowska M, Ohnuma M, Suresh K, Kurzydlowski KJ (2013) Microstructural changes upon annealing in ODS-strengthened ultrafine grained ferritic steel. Journal of Materials Science 48 (13):4620-4625
11. Garcia Oca C, Muñoz-Morris MA, Morris DG (2003) High temperature structural coarsening of an ODS FeAl intermetallic. Intermetallics 11 (5):425-434
12. Dai L, Liu Y, Dong Z (2012) Size and structure evolution of yttria in ODS ferritic alloy powder during mechanical milling and subsequent annealing. Powder Technology 217:281-287
13. Toualbi L, Ratti M, André G, Onimus F, De Carlan Y (2011) Use of neutron and X-ray diffraction to study the precipitation mechanisms of oxides in ODS materials. Journal of Nuclear Materials 417 (1):225-228
14. Besterci M (1994) Structure analysis of dispersion strengthening. Scripta Metallurgica 30(9):1145-1150
15. Hansen N, Ralph B (1986) Additive strengthening mechanisms in dispersion hardened polycrystals. Acta Metallurgica 34 (10):1955-1962
16. Smith CS (1948) Grains, phases, and interfaces: as interpretation of microstructure. Metal Technology 15 (4):1-37
17. Hansen N, Ralph B (1982) The strain and grain size dependence of the flow stress of copper. Acta Metallurgica 30 (2):411-417
18. Hall EO (1951) The deformation and ageing of mild steel: III discussion of results. Proceedings of the Physical Society Section B 64 (9):747
19. Petch NJ (1953) The cleavage strength of polycrystals. Journal of Iron Steel Institute 174:25-28
20. Fu HH, Benson DJ, Meyers MA (2001) Analytical and computational description of effect of grain size on yield stress of metals. Acta Materialia 49 (13):2567-2582
21. Dieter GE (1976) Mechanical Metallurgy, McGraw-Hill, New York:pp.219-231.
22. Nadkarni AV (1984) Dispersion strengthened copper: properties and applications.

In: Ling E, Taubenblat P W: High conductivity copper and aluminum alloys, AIME:pp.77-101.

23. Ebeling R, Ashby MF (1966) Dispersion hardening of copper single crystals. Philosophical Magazine 13 (124):805-834

24. Lagerpusch U, Mohles V, Baither D, Anczykowski B, Nembach E (2000) Double strengthening of copper by dissolved gold-atoms and by incoherent SiO_2 particles: how do the two strengthening contributions superimpose? Acta Materialia 48 (14):3647-3656

25. Nembach E (1992) Synergetic effects in the superposition of strengthening mechanisms. Acta Metallurgica 40 (12):3325-3330

26. Jorge Jr AM, Peres MM, Fogagnolo JB, Kiminami CS, Bolfarini C, Botta WJ (2009) Hot Extrusion of Nanostructured Al-Powder Alloys: Grain Growth Control and the Effect of Process Parameters on Their Microstructure and Mechanical Properties. Metallurgical and Materials Transactions A 40 (13):3314-3321

27. Hu L, Li Z, Wang E (1999) Influence of extrusion ratio and temperature on microstructure and mechanical properties of 2024 aluminium alloy consolidated from nanocrystalline alloy powders via hot hydrostatic extrusion. Powder Metallurgy 42 (2):153-156

28. Hayes RW, Rodriguez R, Lavernia EJ (2001) The mechanical behavior of a cryomilled Al–10Ti–2Cu alloy. Acta Materialia 49 (19):4055-4068

Chapter Six

Effect of Annealing Temperature on Microstructure and Microhardness of an Ultrafine Structured Cu-5vol.%Al_2O_3 Nanocomposite

6.1 Introduction

Annealing plays a very important role in determining the thermal stability and optimizing the mechanical properties of materials. By annealing bulk ultrafine structured MMNCs consolidated by powder compact extrusion at different temperatures, different matrix microstructures, nanoparticle sizes and different strengths, reflected by microhardness values, can be produced. This microstructural and mechanical property data obtained through annealing can be further used to judge the thermal stability of the material and as input parameters to optimize the materials property. It has been shown by previous studies that the microstructural stability and associated stable mechanical properties, of bulk ultrafine structured MMNCs consolidated is largely controlled by the resistance of nanoparticles to coarsening [1-3].

In the present study, a bulk ultrafine structured Cu-5vol.%Al_2O_3 nanocomposite sample extruded at 900°C was annealed at temperatures ranging from 500 to 900°C for 1 hour to establish the relationship between the microstructure and mechanical property of the sample annealed and to further understand the role of ceramic nanoparticles on the thermal stability of bulk ultrafine structured MMNCs materials.

6.2 Results

6.2.1 The effect of annealing on microstructure

Figure 6.1 presents the TEM bright field images of the microstructures of the Cu-5vol.%Al_2O_3 nanocomposite sample before and after annealing at different temperatures. As shown in Figure 6.1(a), the microstructure of as-extruded sample consisted of ultrafine Cu grains which contained considerable dislocations. The sizes of the Cu grains increased with increasing the annealing temperature from 500 to 900°C, as shown in Figures 6.1(b)-(d).

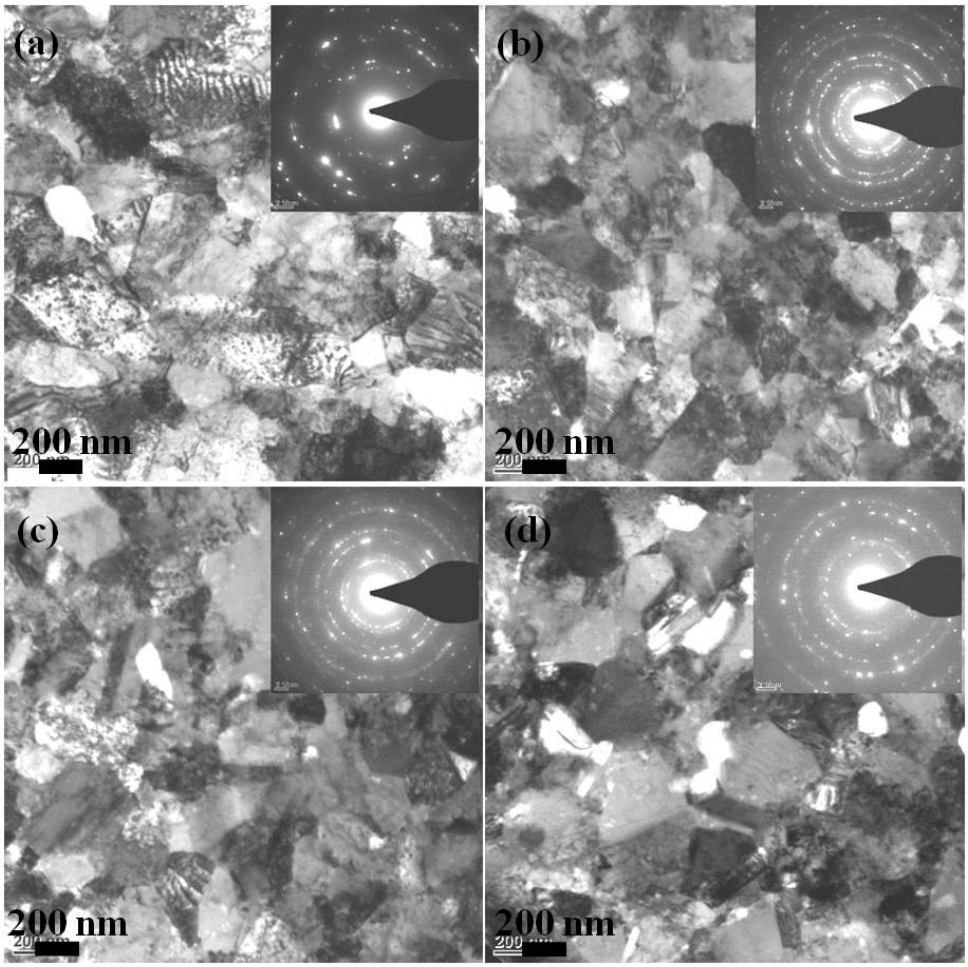

Figure 6.1: Bright field TEM micrograghs of the microstructures of (a) the as-extruded Cu-5vol.%Al_2O_3 nanocomposite sample and (b)-(d) the extruded sample after annealing at 500, 700 and 900°C for 1 h, respectively. The insets are their corresponding SAED patterns.

The variation of the average Cu grain size of the samples is presented in Figure 6.2. After annealing the extruded sample at 500°C for 1h, the average value of Cu grain size remained almost unchanged. The average Cu grain size of the extruded sample increased gradually with increasing annealing temperature and reached a value of 336 nm at 900°C, as shown in Figure 6.2.

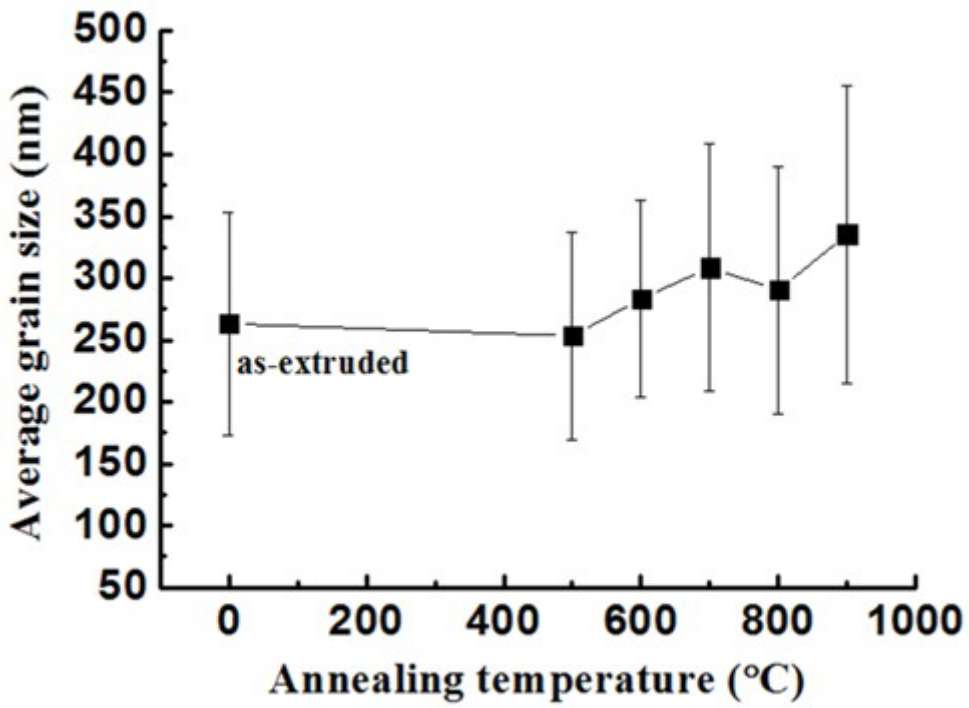

Figure 6.2: The average Cu grain size of the as-extruded Cu-5vol.%Al_2O_3 nanocomposite sample as a function of annealing temperature.

The microstructural change of the Cu matrix of the samples can be further quantified by the change of grain size distribution. As shown in Figure 6.3, in comparison with the as-extruded sample, the range of the Cu grain size distribution of the sample annealed shifted from left to right. This means that with increased annealing temperature, the volume fraction of smaller Cu grains decreases, indicating that the growth of Cu grains occurs. The extent of shifting was proportional to the annealing temperature, suggesting that the amount of Cu grain growth increases with increasing annealing temperature.

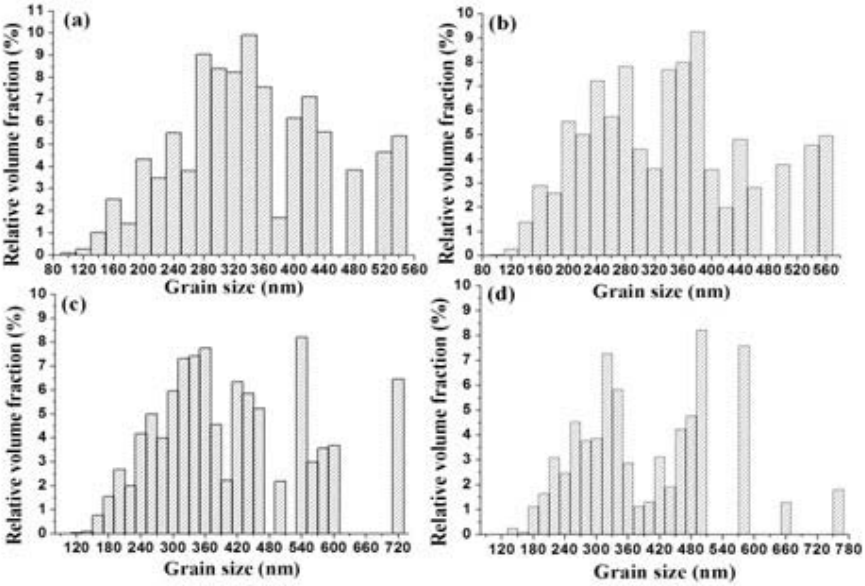

Figure 6.3: Cu grain size distributions of (a) the as-extruded Cu-5vol.%Al_2O_3 nanocomposite sample and the extruded sample annealed at (b) 500, (c) 700 and (d) 900°C for 1 h, respectively.

The SEM backscattered electron images of as-extruded and annealed samples, as-shown in Figure 6.4, demonstrated the coarsening of Al_2O_3 nanoparticles in the microstructure of the extruded sample with the increase of annealing temperature. As shown in Figure 6.4, it is not easy to see the difference between Al_2O_3 nanoparticles from the samples annealed at different temperatures.

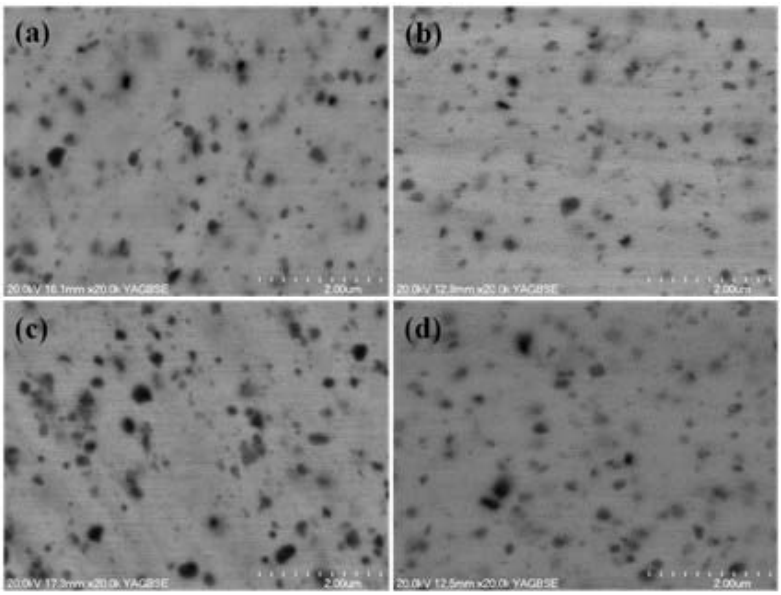

Figure 6.4: Backscattered electron images of (a) the as-extruded Cu-5vol.%Al_2O_3

nanocomposite sample and the extruded sample annealed at (b) 500, (c) 700 and (d) 900°C for 1 h, respectively.

To overcome this, the statistical data of Al_2O_3 nanoparticles of the samples annealed at different temperatures was collected and is presented in Figures 6.5-6.7, respectively. From the data shown in Figure 6.5, it can be seen that after 1h annealing at temperatures ≤600°C, the average Al_2O_3 particle size of the extruded sample increased from 100 to 116 nm when the annealing temperature was increased from room temperature to 600°C. With increasing the annealing temperature to 700°C, the average particle size of Al_2O_3 nanoparticles decreased unexpectedly to 95 nm. The average Al_2O_3 particle size increased with the further increase of the annealing temperature and reached 126 nm at 900°C. Figure 6.6 presents the change of the measured Al_2O_3 volume fraction of the extruded sample with changing the annealing temperature. It is clear that when the annealing temperature was ≤600°C, a slight increase of the volume fraction of Al_2O_3 nanoparticles of the annealed sample was observed as compared to that of the as-extruded sample. However, the measured Al_2O_3 volume fraction did not change much with the further increase of the annealing temperature from 600 to 900°C.

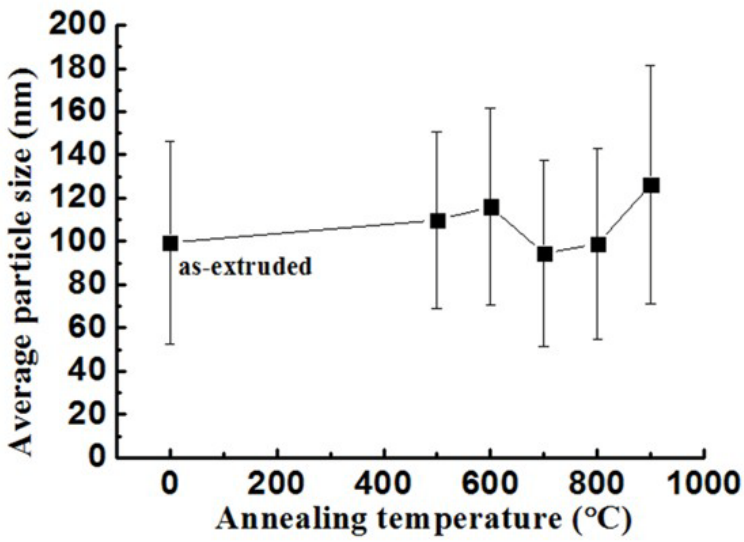

Figure 6.5: The average Al_2O_3 particle size of the Cu-5vol.%Al_2O_3 nanocomposite sample extruded as a function of annealing temperature.

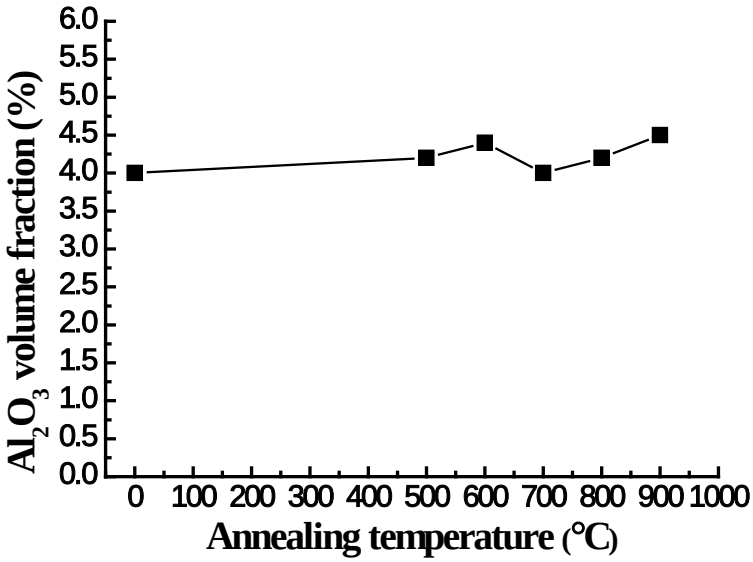

Figure 6.6: The Al_2O_3 volume fraction of the Cu-5vol.% Al_2O_3 nanocomposite sample extruded as a function of annealing temperature.

As shown in Figure 6.7, the relative volume fraction of Al_2O_3 nanoparticles with sizes smaller than 70 nm in the microstructure of 500°C annealed sample was clearly lower than that in the microstructure of the as-extruded sample, indicating that a fraction of small Al_2O_3 nanoparticles were consumed to achieve the coarsening of relatively large Al_2O_3 nanoparticles. Then with increasing the annealing temperature from 500 to 700°C, the relative volume fraction of Al_2O_3 nanoparticles with sizes smaller than 70nm increased significantly, indicating the precipitation of Al^{3+}/O^{2-} clusters in the extruded sample. Such precipitation which generates a considerable number of small Al_2O_3 nanoparticles leads to a sudden reduction in the average Al_2O_3 particle size, as shown in Figure 6.5. As shown in Figures 6.7(c) and 6.7(d), increasing the annealing temperature to 900°C, caused the relative volume fraction of Al_2O_3 nanoparticles with sizes smaller than 110 nm to decrease markedly, suggesting that coarsening of Al_2O_3 nanoparticles occurred.

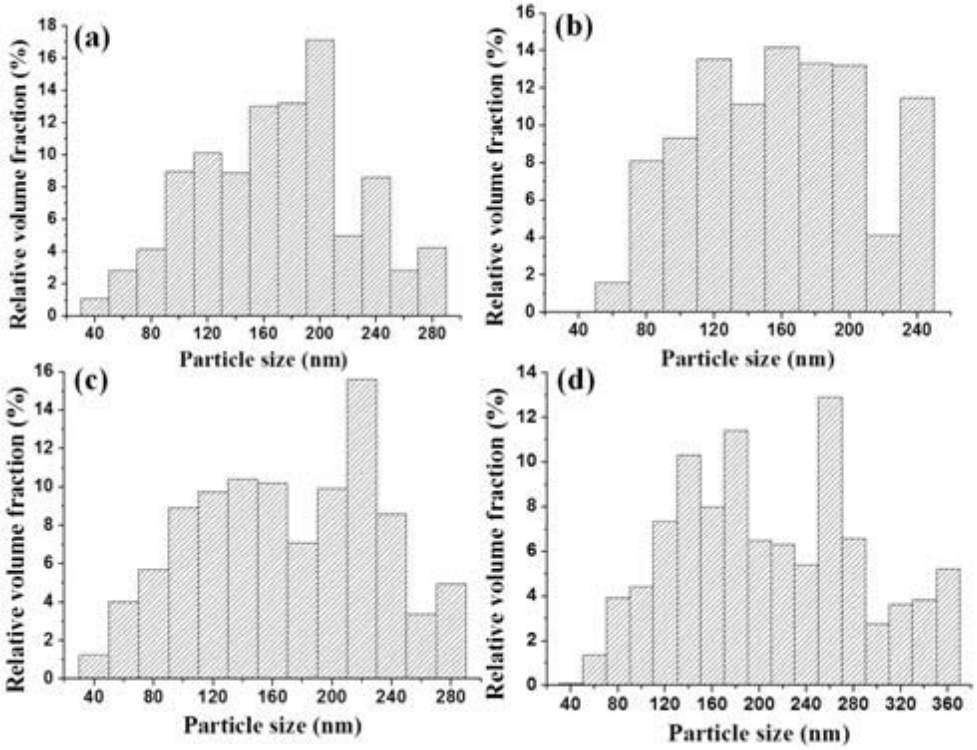

Figure 6.7: Al_2O_3 particle size distributions of (a) the as-extruded Cu-5vol.%Al_2O_3 nanocomposite sample and the extruded sample annealed at (b) 500, (c) 700 and (d) 900°C for 1 h, respectively.

6.2.2 The effect of heat treatment on microhardness

The microhardness of the extruded sample as a function of annealing temperature is shown in Figures 6.8. It can be seen that the microhardness of the extruded sample decreased with increasing the annealing temperature to 600°C from 1.8 to 1.6 GPa. As the annealing temperature was further increased to 700°C, the microhardness of the annealed sample suddenly increased to 1.7 GPa. With further increasing the annealing temperature to 800°C, the microhardness value of the annealed sample decreased slightly to 1.67 GPa, but then decreased significantly to 1.5 GPa with further increasing the annealing temperature to 900°C.

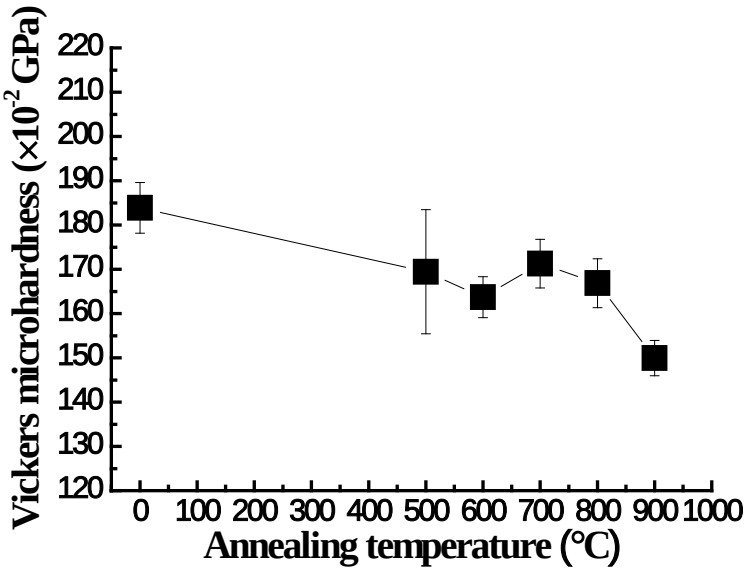

Figure 6.8: The variation of the microhardness of the Cu-5vol.%Al_2O_3 nanocomposite sample extruded with the annealing temperature for an annealing time of 1 h.

6.3 Discussion

Figures 6.1, 6.2 and 6.3 demonstrate that the grain growth behavior of the Cu matrix of the extruded sample occurs during 1h annealing in the temperature range 500-900°C. The average Cu grain size of the annealed sample increases from 263 to 336 nm when the annealing temperature is increased from room temperature to 900°C. In the present work, the growth behavior of Cu grains during annealing is mainly determined by the thermal stability of Al_2O_3 nanoparticles in the extruded sample. Thus, the low growth rate observed for the Cu grains in the extruded sample is attributed to the high resistance of Al_2O_3 nanoparticles to coarsening during annealing. While the coalescence of Al_2O_3 nanoparticles of the extruded sample was not significant during the process of annealing, such coarsening may be sufficient to break the balance between the grain growth driving force and pinning force provided by Al_2O_3 nanoparticles and subsequently account for the slight Cu grain grow observed. According to the Ostwald ripening theory [4-5], small Al_2O_3 nanoparticles must be consumed to achieve the growth of relatively big Al_2O_3 nanoparticles of the extruded sample during annealing. This must lead to the loss of the thermal stability

of some Cu grains. As a result, inhomogeneous grain growth of the extruded sample occurred during annealing (Figure 6.1).

Since the microhardness of the ultrafine structured metal matrix nanocomposites is closely related to its internal stress, average grain size and the size and distribution of second phase nanoparticles in the matrix, the change of the microhardness value of the Cu-5vol.%Al_2O_3 nanocomposite sample with the annealing temperature (Figure 6.8) can be explained in terms of the change of its microstructure during annealing. The observed decrease in the microhardness of the sample annealed at 500°C (Figure 6.8) is primarily caused by the coarsening of Al_2O_3 nanoparticles and Cu grains (Figures 6.2 and 6.5). When the annealing temperature is increased to 600°C, both Cu grains and Al_2O_3 nanoparticles coarsened further which results in a further reduction in microhardness. Although the sample annealed at 700°C has a greater average Cu grain size compared with those of the samples annealed at 500 and 600°C (Figure 6.2), the microhardness is larger. This is likely due to the precipitation of residual Al^{3+}/O^{2-} clusters of the as-extruded sample (Figures 6.5-6.7). In other words, the increase of the microhardness caused by the small precipitated Al_2O_3 nanoparticles of the sample annealed at 700°C exceeds the decrease of the microhardness resulting from the reduction of the dislocation density, Cu grain growth and the Al_2O_3 nanoparticle coarsening. Higher annealing temperature (>700°C) weakens the strengthening effect caused by small Al_2O_3 precipitates due to the coarsening of Al_2O_3 nanoparticles, in addition, the Cu grains become larger. These microstructural changes lead to a quick decrease in microhardness of the sample with increasing the annealing temperature to 900°C (Figure 6.8).

6.4 Summary

Annealing of the ultrafine structured Cu-5vol.% Al_2O_3 nanocomposite sample extruded at 900°C at temperatures ranging from 500 to 900°C for 1h was conducted. The results

obtained in this study allow the following conclusions to be drawn:

(1) Oxide dispersion strengthening enables excellent thermal stability of a bulk ultrafine structured Cu. The microstructure and microhardness of the extruded sample remain stable up to annealing at 800°C for 1 h;

(2) High resistance of Al_2O_3 nanoparticles to coarsening is responsible for the high thermal stability of the microstructure of the extruded sample;

(3) The sudden drop in microhardness of the sample annealed at 900°C is associated with the coarsening of Al_2O_3 nanoparticles and grain growth of the Cu matrix.

6.5 References

1. Biselli C, Morris DG, Randall N (1994) Mechanical alloying of high-strength copper alloys containing TiB_2 and Al_2O_3 dispersoid particles. Scripta Metallurgica 30 (10):1327-1332

2. Garcia OC, Muñoz-Morris MA, Morris DG (2003) High temperature structural coarsening of an ODS FeAl intermetallic. Intermetallics 11 (5):425-434

3. Oksiuta Z, Kozikowski P, Lewandowska M, Ohnuma M, Suresh K, Kurzydlowski K (2013) Microstructural changes upon annealing in ODS-strengthened ultrafine grained ferritic steel. Journal of Materials Science 48 (13):4620-4625

4. Lifshitz IM, Slyozov VV (1961) The kinetics of precipitation from supersaturated solid solutions. Journal of Physics and Chemistry of Solids 19 (1):35-50

5. Wagner C (1961) Theory of precipitate change by redissolution. Zeitschrift für Elektrochemie 65 (7-8):581-591

Chapter Seven

Conclusions and Recommendations for Future Work

7.1 Conclusions

- The microstructure of nanostructured Cu-5vol.%Al_2O_3 nanocomposite powder particles produced by HEMM had a dramatically high thermal stability at temperatures up to 600°C. After annealing at 600°C for 5 h, Cu nanograins in the microstructure of the nanocomposite powder particles only grew slightly and the microstructure of the Cu matrix of powder particles was still well within the nanostructure range. The activation energy for the grain growth of powder samples was calculated to be 63.4 kJ/mol suggesting grain boundary diffusion controlled grain growth behavior. The impressive thermal stability of the microstructure of the powder particle samples is mainly associated with the effect of Al_2O_3 nanoparticles on the grain growth through inhibiting the grain boundary diffusion, which leads to a higher grain growth activation energy compared to nanocrystalline pure Cu (30 kJ/mol).
- HEMM and consolidation conditions can significantly affect the microstructures of bulk ultrafine structured Cu-5vol.%Al_2O_3 nanocomposites and thus influence their mechanical properties such as strength and ductility. The dissolution of Al_2O_3 nanoparticles in the extruded sample was observed when the extrusion was done at 900°C. Such phenomenon was found to be beneficial to the enhancement of the strength and ductility of the extruded sample.
- Cu grains and the sizes and volume fractions of Al_2O_3 nanoparticles of bulk ultrafine structured Cu-5vol.%Al_2O_3 nanocomposite samples extruded increased with increased extrusion temperature. The average sizes of Cu grains and Al_2O_3 nanoparticles and the volume fraction of Al_2O_3 nanoparticles of the extruded samples increased from 132 nm, 43 nm and 0.75% to 263 nm, 100 nm and 4%,

respectively, as the extrusion temperature increased from 300 to 900°C. The increases in the sizes and volume fraction of the Al_2O_3 nanoparticles with the increase of the extrusion temperature were caused by the precipitation of Al_2O_3 nanoparticles during extrusion.

- The samples extruded at 400°C or lower fractured prematurely without yielding, while the samples extruded at T≥500°C fractured after yielding. The YS and UTS of such materials changed only slightly with the increase of the extrusion temperature and had values in the range 466-517 and 546-564 MPa. However, the tensile ductility of the extruded samples was proportional to the extrusion temperature and increased from 0.76 to 5.82% with increasing the extrusion temperature from 500 to 900°C. The increase in the ductility was associated with the improved interparticle atomic bonding and the coarsening microstructure of the Cu matrix. It was also found that the ductility of the extruded samples was primarily determined by the interparticle bonding when T≤800°C; when T=900°C it is controlled by both the interparticle bonding and the microstructure of the Cu matrix.
- The grain boundary strengthening made the largest contribution to the strength of the extruded samples relative to the nanoparticle strengthening and strain hardening and experimentally measured yield strength of the extruded samples could be predicted appropriately by the sum of Peierls stress, grain boundary strengthening, nanoparticle strengthening and strain hardening.
- Al_2O_3 nanoparticles enabled excellent thermal stability of the ultrafine structured Cu of the sample extruded at 900°C. The microstructure and microhardness of the sample extruded remained stable up to annealing at 800°C for 1 h. High resistance of Al_2O_3 nanoparticles to coarsening was responsible for this dramatically high thermal stability. The microhardness increase observed for the sample annealed at 700°C for 1 h came from the precipitation of small Al_2O_3 nanoparticles. The sudden drop in microhardness of the sample annealed at 900°C for 1 h was related to the coarsening of small Al_2O_3 nanoparticles and grain growth of the Cu matrix.

7.2 Recommendations for Future Work

- Measure electrical conductivity of the bulk ultrafine structured Cu-5vol.%Al_2O_3 nanocomposite sample extruded at 900°C and then use the measured electrical and mechanical data as input to further improve the property of the extruded sample by annealing and/or changing initial volume fraction of Al_2O_3 nanoparticles.
- Determine softening temperature of the sample with the optimized mechanical and electrical properties.
- Conduct high temperature tensile tests on the sample with the optimized mechanical and electrical properties to link high temperature strength with microstructure.

Appendix A

Materials Science & Engineering A 584 (2013) 67–72

Contents lists available at SciVerse ScienceDirect

Materials Science & Engineering A

journal homepage: www.elsevier.com/locate/msea

Factors controlling the tensile properties of ultrafine structured Cu–5vol%Al_2O_3 nanocomposite prepared by high energy mechanical milling and powder compact extrusion

D.S. Zhou [a], D.L. Zhang [a,b,*], C. Kong [c], P. Munroe [c]

[a] Waikato Centre for Advanced Materials (WaCAM), School of Engineering, The University of Waikato, Private Bag 3105, Hamilton, New Zealand
[b] State Key Laboratory for Metal Matrix Materials, School of Materials Science and Engineering, Shanghai Jiao Tong University, Shanghai 200240, China
[c] Electron Microscope Unit, The University of New South Wales, Sydney, Australia

ARTICLE INFO

Article history:
Received 19 April 2013
Accepted 4 July 2013
Available online 10 July 2013

Keywords:
High energy mechanical milling
Metal matrix nanocomposite
Ultrafine structure
Mechanical property
Strengthening mechanism

ABSTRACT

The microstructures and tensile properties of two ultrafine structured Cu–5vol%Al_2O_3 nanocomposite samples made by a combination of high energy mechanical milling of a mixture of Cu powder and gamma Al_2O_3 nanopowder and powder compact extrusion were studied. The sample extruded at 750 °C exhibited a microstructure consisting of Cu grains with sizes in the range of 100–500 nm and a dispersion of Al_2O_3 nanoparticles with sizes in the range of 20–345 nm. With the extrusion temperature increasing to 900 °C, the Cu grain sizes remained almost unchanged, but a large fraction of the Al_2O_3 nanoparticles were dissolved, leading to possible formation of nanometer sized Al^{3+}/O^{2-} clusters. This microstructural difference of the two samples causes an interesting difference in tensile properties, with the sample extruded at 900 °C showing approximately 150 MPa higher yield strength and ultimate tensile strength and also better ductility than the sample extruded at 750 °C. It appears that this significant beneficial effect of dissolution of Al_2O_3 nanoparticles is mainly caused by the significant strengthening effect of the nanometer sized Al^{3+}/O^{2-} clusters through Orowan mechanism.

1. Introduction

Metal matrix nanocomposites (MMNCs) reinforced by a dispersion of nanometer sized ceramic particles (diameter < 100 nm) have been extensively investigated [1–10]. In comparison with metal matrix composites (MMCs) reinforced with micrometer sized ceramic particles which have been widely studied, the advantages of using nanometer sized ceramic particles to reinforce the metal matrix are two folds: stronger strengthening effects through the Orowan mechanism due to much smaller interparticle distances [11,12] and prevention of particle cracking during deformation [13,14]. When the ceramic nanoparticles in the MMNCs are oxide nanoparticles and their volume fraction is not higher than 5%, such materials are also called oxide dispersion strengthened (ODS) alloys.

Among MMNCs which have been studied, copper based MMNCs have been most popular due to their potential of offering high strength, high electrical conductivity and high microstructural stability at elevated temperatures which are highly desirable for applications as resistance welding electrodes and electrical contact and connect materials [3–5,9–12,15–17]. Recently, attention has been paid to combining grain boundary strengthening of the metal matrix and nanoparticle strengthening to raise the strength of MMNCs with a given volume fraction of ceramic nanoparticles to a higher level [5–7,10]. To achieve significant grain boundary strengthening, the grain size of the metal matrix needs to be reduced to less than 500 nm. Such MMNCs are called ultrafine structured MMNCs. The most widely used materials processing route for synthesizing ultrafine structured MMNCs is high energy mechanical milling (HEMM) of a mixture of starting powders to produce nanostructured powder particles with or without nanometer sized ceramic particles dispersed in them followed by powder consolidation. If the nanoparticles in the final microstructure are not dispersed inside the powder particles through HEMM, they may be produced through reactions such as internal oxidation of powders (e.g. internal oxidation of Cu–Al alloy to form dispersed Al_2O_3 nanoparticles) or internal reactions during heat treatment of the milled powders or powder consolidation. As an excellent example, Nachum et al. [5] recently reported that the ultrafine structured Cu-(1 and 5) vol% Al_2O_3 nanocomposites made by a combination of HEMM, powder oxidation and powder consolidation exhibited high tensile yield strength of up to 460 and 620 MPa,

* Corresponding author at: School of Materials Science and Engineering, Shanghai Jiao Tong University, Shanghai 200240, China. Tel./fax: +86 21 54743248.
E-mail addresses: dz68@waikato.ac.nz (D.S. Zhou), zhangdeliang@sjtu.edu.cn (D.L. Zhang), c.kong@unsw.edu.au (C. Kong), p.munroe@unsw.edu.au (P. Munroe).

0921-5093/$ - see front matter © 2013 Elsevier B.V. All rights reserved.
http://dx.doi.org/10.1016/j.msea.2013.07.005

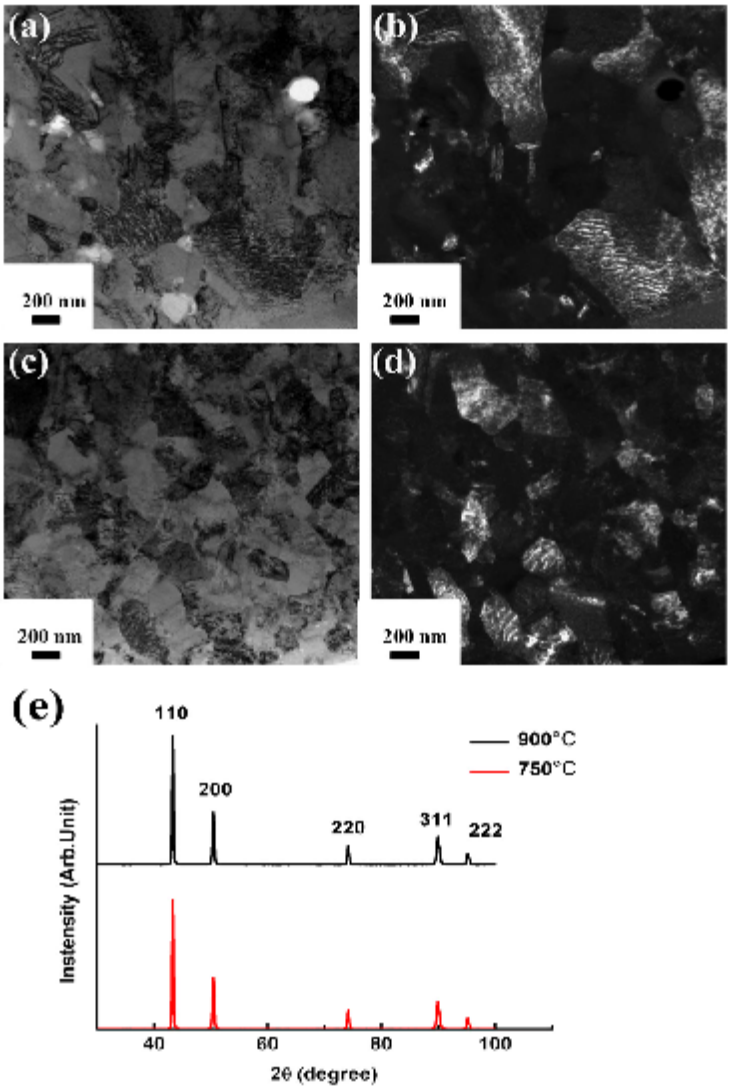

Fig. 1. Bright field ((a) and (c)) and dark field ((b) and (d)) TEM micrographs and XRD patterns ((e)) of Cu–5vol% Al_2O_3 samples extruded at 750 and 900 °C, respectively.

respectively, and a good ductility reflected by an elongation to fracture of 10%. To reinforce the achievement of this work, our study to be presented in this paper demonstrated that ultrafine structured Cu–5vol%Al_2O_3 nanocomposite samples with a combination of high strength and good ductility can also be produced by a combination of HEMM of a mixture of Cu powder and Al_2O_3 nanoparticles and powder compact extrusion. We also discovered that dissolution of Al_2O_3 nanoparticles during heating and extrusion had a significantly beneficial effect on the mechanical properties of the ultrafine structured Cu–5vol%Al_2O_3 nanocomposite.

2. Experimental procedure

The nanostructured Cu–5vol%Al_2O_3 powder was prepared using HEMM of a mixture of elemental Cu powder (99.7% pure, particle sizes: 1–65 μm) and gamma Al_2O_3 nanopowder (99.9% pure, average particle size: 50 nm). The HEMM process used consisted of two steps: milling 100 g of powder mixture under argon with 61 stainless steel balls of 12.5 mm in diameter to produce millimeter sized composite granules, and then milling the granules using 6 stainless steel balls of 25 mm in diameter and 13 stainless steel balls of 12.5 mm in diameter, also under argon. Each

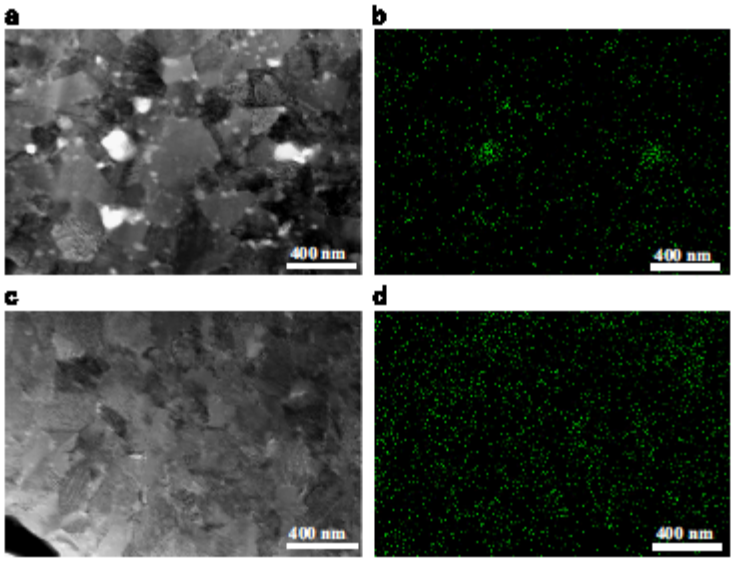

Fig. 2. STEM images ((a) and (c)) and corresponding EDX Al elemental maps ((b) and (d)) of Cu–5vol%Al_2O_3 samples extruded at 750 and 900 °C, respectively.

milling step involved 24 h of milling with an interval break of 30 min after every 30 min of milling. A Retch PM100 planetary ball mill operated at 400 rpm was used. The ball-to-powder weight ratio was 5:1 for both steps. The nanostructured MMNC powder produced by this HEMM process [6] was consolidated by powder compact extrusion. To prepare for the extrusion, the milled powder was compacted at 350 °C in air with a holding time of 10 min and a pressure of 300 MPa to produce powder compacts with a relative density of ~86%. The powder compacts were subsequently heated to 750 and 900 °C, respectively, under argon by induction heating, and extruded into rods of 8 mm in diameter. The extrusion ratio was 10:1.

X-ray diffraction (XRD) (Philips X-pert X-ray diffraction system, Cu Kα radiation and a graphite monochromator), scanning electron microscopy (SEM) (Hitachi S4000 SEM), transmission electron microscopy (TEM) (a Philips/FEI CM200 TEM) in conjunction with scanning transmission electron microscopy (STEM) and energy dispersive X-ray (EDX) spectrometry were used to characterize the microstructure of the consolidated samples. Dog-bone shaped tensile testing specimens with a rectangular cross-section of $2 \times 2\ mm^2$ and a gauge length of 20 mm were cut from the extruded rods using an electric discharge machining wire cutter, and tested using an Instron 4204 testing machine at a strain rate of $1 \times 10^{-4}\ s^{-1}$.

3. Results

From the bright and dark field TEM images and STEM images as shown in Figs. 1 and 2, it can be seen that the sample consolidated at 750 °C had a microstructure consisting of equiaxed Cu grains with sizes in the range of 100–500 nm, and increasing the extrusion temperature to 900 °C did not change the grain sizes significantly. The XRD patterns of the consolidated samples shown in Fig. 1(e) only exhibited diffraction peaks of Cu. The absence of Al_2O_3 peaks in the XRD patterns may be due to low crystallinity and small sizes of gamma Al_2O_3 nanoparticles. The mean grain size and internal strain of the two consolidated samples were estimated based on the XRD line broadening analysis of Cu peaks through the modified Williamson–Hall and classic Williamson–Hall methods [18,19]. The background and $K_{\alpha 2}$ signal were removed and careful correction of instrumental broadening was done from the peaks prior to carrying out the analysis. The calculated values of the mean grain size and the square root of the mean square of the internal strain were 272 nm and 1.24×10^{-7} for the sample extruded at 750 °C, and 237 nm and 6.4×10^{-7} for the sample extruded at 900 °C, respectively. By using the following equation [20,21]:

$$\rho = \frac{2\sqrt{3}}{db}\sqrt{\langle \varepsilon^2 \rangle} \quad (1)$$

where ρ, d, b and $\langle \varepsilon^2 \rangle$ are the dislocation density, mean grain size, burger's vector and mean square of the internal strain of the sample extruded, the dislocation densities of samples extruded at 750 and 900 °C were calculated to be 1.75×10^{13} and $3.98 \times 10^{13}\ m^{-2}$ respectively.

Based on the TEM bright field images, STEM images, EDX elemental mapping and SEM backscattered electron images shown in Figs. 1–3, we can see that the microstructure of the samples extruded at 750 °C had a dispersion of Al_2O_3 nanoparticles with sizes in the range of 20–345 nm. Based on the SEM backscattered electron images, the volume fraction of the Al_2O_3 nanoparticles and nanoparticle clusters was estimated to be around 5 vol%, showing that the amount of Al_2O_3 being dissolved in the matrix was insignificant. As clearly shown in Figs. 1 and 2(a), the Al_2O_3 nanoparticles/nanoparticle clusters are mostly distributed along the grain boundaries. With increasing the extrusion temperature from 750 to 900 °C, the sizes of Al_2O_3 nanoparticles/nanoparticle clusters clearly increased to the range of 20–450 nm, and the number density of the Al_2O_3 nanoparticles/nanoparticle clusters in the microstructure clearly decreased. Based on the SEM backscattered electron images of the sample extruded at 900 °C, the volume fraction of the Al_2O_3 nanoparticles/nanoparticle clusters was estimated to be about 1.38 vol%, showing that 3.62 vol% of

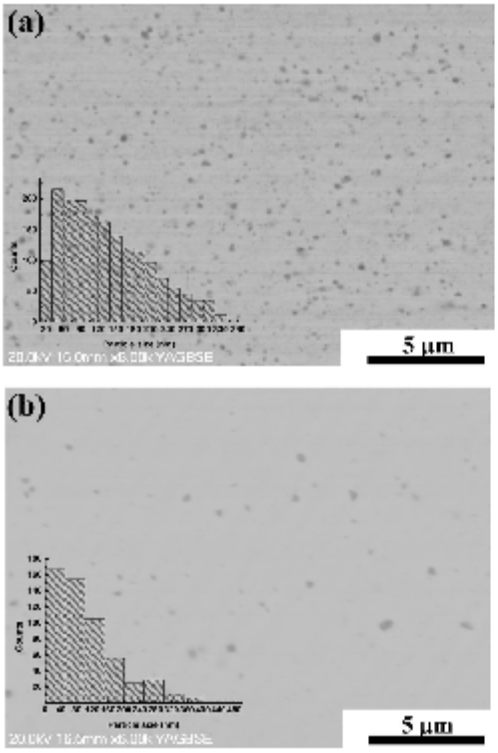

Fig. 3. SEM backscattered electron images of Cu–5vol%Al_2O_3 samples extruded at different temperatures: (a) 750 °C and (b) 900 °C. Insets in (a) and (b) are their corresponding Al_2O_3 particle size distributions.

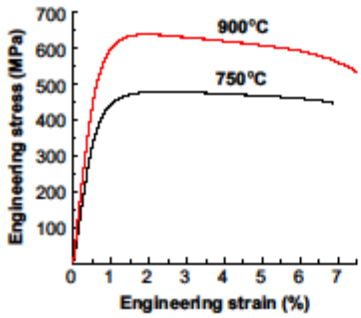

Fig. 4. Tensile engineering stress–engineering strain curves of Cu–5vol%Al_2O_3 samples extruded at 750 and 900 °C, respectively.

Al_2O_3 nanoparticles being dissolved during heating the powder compact to 900 °C and extrusion. The size distributions of Al_2O_3 nanoparticles/nanoparticle clusters in the two consolidated samples were also determined and they are shown in Fig. 3(a) and (b).

As seen from the tensile engineering stress–engineering strain curves shown in Fig. 4 and the values listed in Table 1, the samples consolidated at 750 and 900 °C had an average yield strength (YS) of 414 and 566 MPa, an average ultimate tensile strength (UTS) of 478 and 630 MPa and an average elongation to fracture of 5.65% and 7.63%, respectively. As shown by the tensile stress–strain curves, the samples exhibited nearly ideal (or nearly perfect) plastic deformation in tension, being lack of both significant strain hardening and necking before fracturing. This observation is consistent with the similar observations made on tensile mechanical response of ultrafine structured Cu-(1 and 5) vol% Al_2O_3 nanocomposites [5] and nanocrystalline pure Cu [22]. As shown in Fig. 5(a), the fracture surfaces of the tensile test specimens cut from the sample extruded at 750 °C showed a large number of rounded dimples which are indicators of cavities formed through Al_2O_3 nanoparticle/Cu matrix decohesion and perhaps also debonding at prior interparticle boundaries during plastic deformation. On the other hand, as shown in Fig. 5(b), the fracture surfaces of the tensile test specimens cut from the sample extruded at 900 °C showed a much smaller number of rounded dimples. Instead, much larger and deeper dimples formed by

Table 1
The average tensile yield strength (YS), ultimate tensile strength (UTS) and elongation to fracture (ηQUOTE) of the Cu–5vol%Al_2O_3 samples extruded at 750 and 900 °C, respectively.

ET (°C)	YS (MPa)	UTS (MPa)	η(%)
750	414 ± 46.4	478 ± 1.7	5.65 ± 2.26
900	566.5 ± 10.4	630 ± 6.2	7.54 ± 2.67

ET: Extrusion temperature.

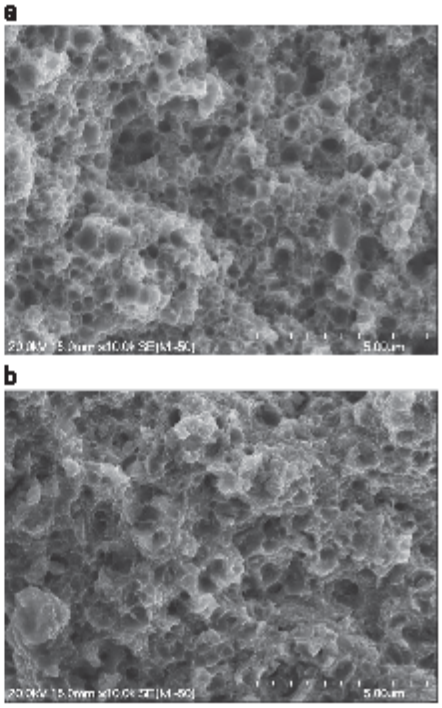

Fig. 5. Fracture surfaces of Cu–5vol%Al_2O_3 samples extruded at 750 and 900 °C, respectively.

intergranular fracture and smaller and shallower dimples formed through transgranular fracture were observed.

4. Discussion

It can be envisaged that the yield strength of the Cu–5-vol% Al_2O_3 nanocomposite samples, σ_y, is the sum of the basic strength of copper associated with lattice friction of dislocations, σ_0, the strength increase caused by grain boundary strengthening, $\Delta\sigma_{gb}$, nanoparticle strengthening, $\Delta\sigma_{np}$ and dislocation strengthening, $\Delta\sigma_d$. Thus, we have the following equation:

$$\sigma_y = \sigma_0 + \Delta\sigma_{gb} + \Delta\sigma_p + \Delta\sigma_d \quad (2)$$

For copper, $\Delta\sigma_0$ is quite small, being in the order of 5 MPa [23]. $\Delta\sigma_{gb}$ can be estimated by using the Hall–Petch relationship which is expressed by the following equation:

$$\Delta\sigma_{gb} = k_{HP} d^{-1/2} \quad (3)$$

where k_{HP} is the Hall–Petch coefficient. Based on previous work on the relationship between the strength of copper and its mean grain size [24], we can take $k = 0.142$ MPa m$^{1/2}$. As mentioned above, the mean grain sizes of samples extruded at 750 and 900 °C are 272 and 237 nm, respectively. By using Eq. (3), it can be estimated that $\Delta\sigma_{gb}$ is 272 and 291 MPa for the samples extruded at 750 and 900 °C, respectively. Based on the Orowan mechanism of nanoparticle strengthening which considers the interaction between dislocations and non-shearable nanoparticles leading to the formation of Orowan loops [25], $\Delta\sigma_{np}$ can be estimated using the following equation:

$$\Delta\sigma_{np} = 0.13\frac{Gb}{\lambda}\ln\left(\frac{r_p}{b}\right), \quad (4)$$

where G is the shear modulus, b is Burger's vector, r_p is the mean radius of the nanoparticles and $\lambda = r_p = \sqrt{(2\pi/3f)}$ [26] is the interparticle spacing (f is the volume fraction of the nanoparticles). For copper, we can take $G = 47.7$ GPa and $b = 0.256$ nm [23,27]. For the sample extruded at 750 °C, the nanoparticle clusters with sizes greater than 200 nm are disregarded in the consideration, since they are too large to be effective in causing strengthening through forming dislocation loops. For particles with sizes smaller than 200 nm, based on Fig. 3(a), the volume fraction and mean radius size of Al_2O_3 nanoparticles are 2.43% and 52.5 nm and thus $\lambda = 487.3$ nm. The same consideration is also used for the sample extruded at 900 °C, based on Fig. 3(b), the volume fraction and mean radius of Al_2O_3 nanoparticles smaller than 200 nm are 0.5% and 41.3 nm and from which we can get $\lambda = 845.1$ nm. Using this information and Eq. (3), it can be estimated that $\Delta\sigma_{np} = 17.3$ and 10 MPa for the samples extruded at 750 and 900 °C, respectively.

The dislocation strengthening, $\Delta\sigma_d$, can be estimated based on the Taylor equation [25]:

$$\Delta\sigma_d = \alpha G b\sqrt{\rho} \quad (5)$$

where α is the strength coefficient of the dislocation network which can be taken to be 0.2 [17]. As mentioned above, the dislocation densities are 1.75×10^{13} and 3.98×10^{13} m^{-2} for the samples extruded at 750 and 900 °C, respectively. Using this information and Eq. (4), $\Delta\sigma_d$ can be estimated to be 10.1 and 15.4 MPa for the samples extruded at 750 and 900 °C, respectively.

The sums of $\sigma_0 + \Delta\sigma_{gb} + \Delta\sigma_p + \Delta\sigma_d$ are 314.4 and 321.4 MPa for samples extruded at 750 and 900 °C, respectively. Referring to Table 1, it can be seen that these sums are about 110 and 245 MPa lower than the actual yield strength of the samples consolidated at 750 and 900 °C, respectively. For the sample consolidated at 750 °C, this significant discrepancy may be caused by the disregard of the synergy between grain boundary strengthening, which is the basis of the Hall–Petch relationship between strength increase and grain size, and nanoparticle strengthening in calculating the contributions of different strengthening mechanisms. As has been well known, Eq. (3) does not make any consideration of the effect of presence of hard nanoparticles on grain boundary strengthening. Similarly, Eq. (4) was derived based on the consideration that Orowan loops form around hard nanoparticles without the interference of grain boundaries. This is certainly not true for ultrafine structured metal matrix nanocomposites where the grain sizes are very similar to the distances between nanoparticles. More theoretical work is needed to quantify the synergy between grain boundary strengthening and nanoparticle strengthening in ultrafine structured MMNCs.

For the sample extruded at 900 °C, the discrepancy is even much larger. The very small volume fraction of particles (0.5%) present in the microstructure of this sample would not be sufficient to induce large enough synergetic effect of nanoparticle strengthening and grain boundary strengthening to account for the approximate 250 MPa discrepancy. It is clear that the main possible reason for this discrepancy is the disregard of the strengthening effect of Al^{3+} and O^{2-} ions and Al^{3+}/O^{2-} clusters in the Cu matrix FCC lattice formed by the dissolution of Al_2O_3 nanoparticles. At this point of research, it is not clear in which form the Al^{3+} and O^{2-} ions exist in FFC Cu lattice. Since Al^{3+} and O^{2-} ions are highly charged, it is very likely that they form electrically neutral Al^{3+}/O^{2-} clusters. The fact that the dissolution of 3.62 vol% Al_2O_3 nanoparticles did not cause any change of the lattice parameter of the Cu lattice (as confirmed by XRD analysis shown above) strongly suggest that all or most of the Al^{3+} and O^{2-} ions exist in the form of nanometer sized and electrically neutral Al^{3+}/O^{2-} clusters. It can be envisaged that the very strong electric field within the clusters would not allow the dislocations to cut through, and the dislocations would have to bypass the clusters by forming Orowan loops. This means that we can estimate the contribution of the strengthening effect of Al^{3+}/O^{2-} clusters based on the Orowan looping mechanism. If we take $r_p = 5$ nm and $f = 3.62$ vol%, we can get $\lambda = 38$ nm. Substituting these data into Eq. (3) and doing the calculation would give $\Delta\sigma_{np}(Al^{3+}/O^{2-}) = 125.3$ MPa. This value is still not sufficient to account for the 250 MPa discrepancy. However, if we take $r_p = 3$ nm and $f = 3.62$ vol%, we can get $\lambda = 22.81$ nm. Substituting these data into Eq. (3), we get $\Delta\sigma_{np}(Al^{3+}/O^{2-}) = 208.7$ MPa. This value is very close to the 250 MPa discrepancy. This strongly suggests that the dissolution of Al_2O_3 nanoparticles lead to the formation of Al^{3+}/O^{2-} clusters with sizes around 3 nm.

5. Conclusions

Ultrafine structured Cu–5vol%Al_2O_3 metal matrix nanocomposite samples prepared by a combination of high energy mechanical milling of a mixture of Cu powder and Al_2O_3 nanopowder and powder compact extrusion exhibit different microstructures due to the use of different extrusion temperatures (750 and 900 °C). Increasing the extrusion temperature from 7590 to 900 °C causes a large fraction of the Al_2O_3 nanoparticles being dissolved, and the dissolution of Al_2O_3 nanoparticles brings a dramatic beneficial effect of significant increase of the strength and clear increase of tensile ductility. It appears that this beneficial effect is caused by the strengthening effect of nanometer sized (possibly around 3 nm) Al^{3+}/O^{2-} clusters formed as a result of the dissolution of Al_2O_3 nanoparticles.

Acknowledgments

The funding from the China Scholarship Council (CSC), China and Foundation for Research, Science and Technology (FRST) (now

Ministry of Business, Innovation and Employment), New Zealand to support this work is gratefully acknowledged.

References

[1] Z. Zhang, T. Topping, Y. Li, R. Vogt, Y. Zhou, C. Haines, J. Paras, D. Kapoor, J.M. Schoenung, E.J. Lavernia, Scr. Mater. 65 (2011) 652.
[2] N.S. Qu, D. Zhu, K.C. Chan, Scr. Mater. 54 (2006) 1421.
[3] J. Naser, W. Riehemann, H. Ferkel, Mater. Sci. Eng. A 234 (1997) 467.
[4] J. Naser, H. Ferkel, W. Riehemann, Mater. Sci. Eng. A 234 (1997) 470.
[5] S. Nachum, N.A. Fleck, M.F. Ashby, A. Colella, P. Matteazzi, Mater. Sci. Eng. A 527 (2010) 5065.
[6] A. Mukhtar, D. Zhang, C. Kong, P. Munroe, J. Mater. Sci. 45 (2010) 4594.
[7] D. Kudashow, H. Baum, U. Martin, M. Heilmaier, H. Oettel, Mater. Sci. Eng. A 387 (2004) 768.
[8] R.K. Guduru, R.O. Scattergood, C.C. Koch, K.L. Murty, S. Guruswamy, M.K. McCarter, Scr. Mater. 54 (2006) 1879.
[9] N. Grant, K. Zwilsky, Trans. Metall. Soc. AIME 221 (1961) 371.
[10] C. Biselli, D.G. Morris, N. Randall, Scr. Metall. 30 (1994) 1327.
[11] V. Rajkovic, D. Bozic, M.T. Jovanovic, Mater. Des. 31 (2010) 1962.
[12] T.S. Srivatsan, N. Narendra, J.D. Troxell, Mater. Des. 21 (2000) 191.
[13] D.J. Lloyd, Int. Mater. Rev. 39 (1994) 1.
[14] D.J. Lloyd, Acta Metall. 39 (1991) 59.
[15] J. Groza, J. Mater. Eng. Perform. 1 (1992) 113.
[16] J. Čuríšin, K. Čuríšinová, M. Ondrinová, K. Saksl, Mater. Lett. 58 (2004) 3796.
[17] M. Besterci, Scr. Metall. 30 (1994) 1145.
[18] T. Ungár, I. Dragomir, Á. Révész, A. Borbély, J. Appl. Cryst. 32 (1999) 992.
[19] G.K. Williamson, W.H. Hall, Acta Metall. 1 (1953) 22.
[20] Y.H. Zhao, K. Lu, K. Zhang, Phys. Rev. B 66 (2002) 085404.
[21] G. Williamson, R. Smallman, Philos. Mag. 1 (1956) 34.
[22] Y. Champion, C. Langlois, S. Guérin-Mailly, P. Langlois, J.L. Bonnentien, M.J. Hÿtch, Science 300 (2003) 310.
[23] N. Hansen, B. Ralph, Acta Metall. 30 (1982) 411.
[24] D.J. Benson, H.H. Fu, M.A. Meyers, Mater. Sci. Eng. A 319 (2001) 854.
[25] G.E. Dieter, Mechanical Metallurgy, McGraw-Hill, New York, (1976) pp. 219.
[26] A.V. Nadkarni, Dispersion strengthened copper: properties and applications, SCM Metal Products, Cleveland, Ohio, (1984) pp. 77.
[27] L. Balogh, T. Ungár, Y. Zhao, Y.T. Zhu, Z. Horita, C. Xu, T.G. Langdon, Acta Mater. 56 (2008) 809.

Thermal stability of the nanostructure of mechanically milled Cu–5 vol% Al_2O_3 nanocomposite powder particles

Dengshan Zhou
Waikato Centre for Advanced Materials, School of Engineering, The University of Waikato, Hamilton, New Zealand
Deliang Zhang[a)]
State Key Laboratory for Metal Matrix Materials, School of Materials Science and Engineering, Shanghai Jiao Tong University, Shanghai 200240, China
Charlie Kong and Paul Munroe
Electron Microscope Unit, The University of New South Wales, Sydney, Australia
Rob Torrens
Waikato Centre for Advanced Materials, School of Engineering, The University of Waikato, Hamilton, New Zealand

(Received 8 November 2013; accepted 25 March 2014)

Isothermal annealing in the temperature range of 300–600 °C, microstructural characterization, and analysis of the grain growth kinetics during annealing were carried out for Cu–5 vol% Al_2O_3 nanocomposite powder particles produced by high energy mechanical milling. When the annealing temperature was 400 °C or lower, only reduction in dislocation density occurred during annealing. When the annealing temperature was 500 °C or higher, reduction in dislocation density, abnormal grain growth of the nanocrystalline Cu matrix, and coarsening of the Al_2O_3 nanoparticles occurred. It has been found that the microstructure of the nanocrystalline Cu matrix of the nanocomposite exhibits a far higher thermal stability than that of monolithic nanocrystalline Cu, even though the apparent activation energy of the grain growth of the former is similar to that of the latter over the temperature range of 400–600 °C, showing the dramatic drag effects of finely distributed Al_2O_3 nanoparticles and Al^{3+}/O^{2-} clusters on the grain boundary motion.

I. INTRODUCTION

It has been widely accepted that the consolidation of nanostructured powders is an effective way of synthesizing bulk nanostructured and ultrafine structured metallic materials and near-net shaped components.[1] For this approach to be used effectively, either or both of two conditions should be satisfied: (1) the time for keeping the nanostructured powder at relatively high temperature (above 0.6 T_m, where T_m is the melting temperature of the metal in Kelvin scale) during consolidation should be sufficiently short, being in the order of minutes rather than hours and (2) the thermal stability of the nanostructure of the powder particles is sufficiently high to allow the nanostructure to coarsen by only a small amount at relatively high temperatures. The first condition can be possibly satisfied if the powder is consolidated using processes that involve pressure and/or a large amount of plastic flow. Such processes include in situ consolidation of powder particles by high energy mechanical milling (HEMM),[2,3] powder compact forging,[4] powder compact extrusion,[5] and spark plasma sintering.[6] When such processes are not able to produce well-consolidated materials or are not cost-effective, it is necessary to improve the thermal stability of the nanostructure of the powder particles.

Thermodynamic and kinetic strategies have been used to increase the thermal stability of the nanostructure of materials.[7] The thermodynamic strategy which was first proposed by Weissmüller[8] uses the segregation of alloying atoms to grain boundaries to reduce the grain boundary energy and hence the driving force for grain growth. Experimental work has shown that this strategy is highly effective. For example, it has been shown that the thermal stability of the nanostructure of nanocrystalline Pd–19 at.% Zr,[9,10] Fe–(1–4) at.% Zr[11], and Cu–(1–5) at.% Zr[12] alloys are significantly higher than that of pure Pd, Fe, and Cu, respectively, due to the strong segregation of Zr atoms to the grain boundaries of these metals. Malow and Koch[13] and Liu and Mücklich[14] showed that nanocrystalline Fe and RuAl with segregated impurity atoms at grain boundaries exhibit high thermal stability. Recently, Chookajorn et al.[15] also successfully synthesized a nanocrystalline W–20 at.% Ti alloy, and proposed a new thermodynamic model to elucidate the underlying thermodynamic relationships that determine the high thermal stability of nanocrystalline alloys. The kinetic strategy which utilizes small second phase particles to retard the movement of grain boundaries has also been shown to be highly effective in stabilizing

a)Address all correspondence to this author.
e-mail: zhangdeliang@sjtu.edu.cn
DOI: 10.1557/jmr.2014.79

the microstructure of nanocrystalline materials at elevated temperatures up to 0.65 T_m.[16–22]

Although many nanostructured materials stabilized by fine second phase particles have been reported, systematic investigation of the grain growth behavior and kinetics of such kind of nanostructure is still missing. The present study is to investigate the grain growth of the nanocrystalline Cu matrix and other microstructural changes of the nanostructured Cu–5 vol% Al_2O_3 nanocomposite powder particles during isothermal annealing at different temperatures in the range of 300–600 °C. Comparison between the grain growth kinetics of the nanocrystalline Cu matrix of the nanocomposite and those of monolithic nanocrystalline Cu is also made. It is hoped that through this study, an in-depth understanding of the changes and stability of the nanostructure of metal matrix nanocomposites during annealing would be achieved.

The motivation for selecting the ball milled nanostructured Cu–5 vol% Al_2O_3 nanocomposite powder in this study is based on two considerations. From practical application point of view, this powder material can be used to make bulk ultrafine structured Cu–5 vol% Al_2O_3 nanocomposite which has the potential of having high room temperature and elevated temperature strength, good ductility, high thermal stability, and good conductivity. These properties are very attractive to many applications including making spot welding electrodes and electrical contact materials for electrical switches and circuit breakers. From academic point of view, this material is a good model system for studying microstructure-property relationships and thermal stability of microstructures of nanostructured and ultrafine structured metal matrix nanocomposites.

II. EXPERIMENTAL PROCEDURE

A nanostructured Cu–5 vol% Al_2O_3 nanocomposite powder was prepared using HEMM of a mixture of elemental Cu powder (99.7% pure, particle sizes: 1–100 μm) and gamma Al_2O_3 nanopowder (99.9% pure, average particle size: 50 nm). For each batch of sample, 100 g (in total) of the Cu powder and Al_2O_3 nanopowder were mixed by ball milling for 12 h under an argon atmosphere and using a Retch PM100 planetary ball mill with a speed of 100 rpm and 61 stainless steel balls of 12.5 mm in diameter. Then HEMM of the powder mixture was done under an argon atmosphere and using the same ball mill at a speed of 400 rpm and with six stainless steel balls of 25 mm in diameter and 13 stainless steel balls of 12.5 mm in diameter. The net milling time was 48 h with a break of 30 min after every 30 min interval of milling. The ball-to-powder weight ratio was 5:1 for both mixing and milling steps. The as-milled powder particles were subsequently annealed at different temperatures in the range of 300–600 °C for a time in the range of 0.1–5 h in a vacuum of 10^{-6} mbar. A heating rate of 10 °C/min was used to heat the samples up to the holding temperature and then furnace cooling was used to cool the samples down after holding at the annealing temperature. The microhardness of the as-milled and annealed powder particles was measured using a Vickers microindentation tester, LECO LM700 with a load of 25 gf and a dwell time of 15 s. For each sample, 10 indents were made onto the polished cross sections of powder particles to obtain one average microhardness measurement. As-milled and annealed powder particle samples were first mounted using epoxy and then ground and polished to get "mirror" cross-sectional surfaces of powder particles for microhardness measurements. The bottom surface of the mounted sample, which does not contain powder particles, was also ground carefully and made to be parallel to the top one with powder particles. To avoid influence from the epoxy substrate during microhardness measurements, all indents were produced in the cross sections of relatively large powder particles.

The composition of the as-milled Cu–5 vol% Al_2O_3 powder was measured to be 1.346 wt.% Al (equivalent to ~2.542 wt.% Al_2O_3), 0.175 wt.% Fe, 0.002 wt.% Mn and the balance Cu, using a Spectro XLab2000 x-ray fluorescence system. The as-milled and annealed powder samples were examined using x-ray diffractometry (XRD) (Philips X-pert XRD system, Cu K_α radiation, and a graphite monochromator), scanning electron microscopy (SEM; Hitachi S4000 SEM, Hitachi High-Technologies Corporation, Tokyo, Japan), transmission electron microscopy (TEM; Philips/FEI CM200 TEM, FEI Corporation, Hillsboro, OR) in conjunction with scanning transmission electron microscopy (STEM), and energy dispersive x-ray (EDX) spectrometry. TEM specimens were prepared by cutting thin sections from powder particles using a dual beam focused ion beam (FIB)/SEM microscope.

III. RESULTS

As shown in Fig. 1, the Cu peaks of the XRD patterns of the as-milled and annealed Cu–5 vol% Al_2O_3 nanocomposite powders became narrower with increasing annealing temperature, suggesting that the Cu grains grew during annealing. The Cu peaks of the XRD patterns were analyzed to determine the average Cu grain sizes and dislocation densities of the samples. Prior to doing this, background and $K\alpha_2$ signals were removed from the XRD diffraction peaks, and instrumental broadening was corrected by producing an XRD pattern of the same Cu powder annealed at 900 °C for 1 h. The Scherrer equation, as given below,[23,24] was applied to the first peak of the XRD patterns to evaluate the average grain size of the powder particles:

$$D_{hkl} = \frac{K\lambda}{\beta_{hkl}\cos\theta} \quad , \qquad (1)$$

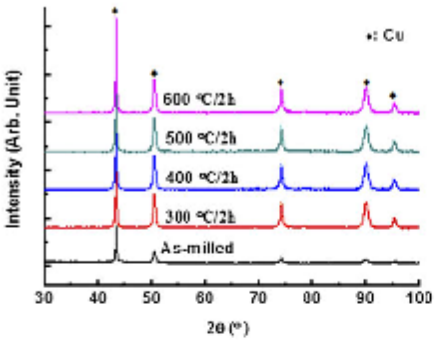

FIG. 1. XRD patterns of as-milled and annealed nanostructured Cu–5 vol% Al_2O_3 nanocomposite powders.

where D_{hkl} is the mean grain size, K is a constant and normally taken to be 1, λ is the wave length of the x-rays used to generate the XRD patterns, β_{hkl} is the integral breadth of the x-ray diffraction peak (in radians) of the planes with Miller indices of {hkl}, and θ is the Bragg angle of the peak used. The internal strain, ε_{hkl}, of the samples was derived from the following equation[25]:

$$\varepsilon_{hkl} = \frac{\beta_{hkl}}{4\tan\theta} \quad . \tag{2}$$

The dislocation density of samples, ρ, was evaluated by the formula given below[26–28]:

$$\rho = \frac{2\sqrt{3}\langle\varepsilon^2_{hkl}\rangle^{1/2}}{D_{hkl}b} \quad , \tag{3}$$

where b is the Burger's vector of pure Cu. In the dislocation density calculation, the first three peaks of XRD patterns were used to obtain the average dislocation densities of the samples.

Figures 2(a) and 2(b) show the average grain sizes as a function of annealing time at different annealing temperatures and a function of annealing temperature with different annealing times, respectively. Figures 2(a) and 2(b) demonstrate that the grain sizes almost remained unchanged with increasing annealing time for an annealing temperature of 400 °C, or lower, whereas when the annealing temperature was 500 °C or higher, the grain sizes first increased at a rate which became higher with increasing annealing temperature, and then reached stagnation with prolonged annealing time. The dislocation densities as a function of annealing time at different annealing temperatures and a function of annealing temperature with different annealing times are presented in Figs. 3(a) and 3(b), respectively. As shown in Fig. 3(a),

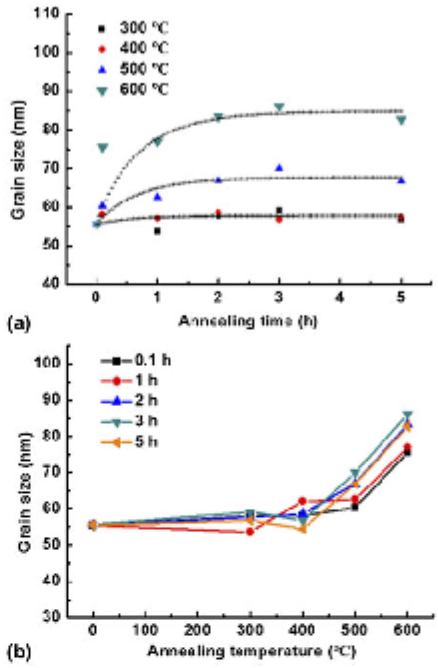

FIG. 2. Changes of grain sizes of the nanocrystalline Cu matrix of the Cu–5 vol% Al_2O_3 nanocomposite powder particles with annealing time at different annealing temperatures (a) and with annealing temperature for different annealing times (b).

at a given annealing temperature, the dislocation density dropped significantly within the first 0.1 h of annealing, then underwent fluctuation with increasing annealing time, and subsequently changed little with further increasing annealing time. As shown in Fig. 3(b), the dislocation density of the annealed powder particles did not change significantly with increasing annealing temperature from room temperature to 300 °C, and then decreased significantly and linearly with increasing annealing temperature from 300 to 600 °C.

Figure 4 shows the TEM bright field micrographs of the microstructure of the nanostructured Cu–5 vol% Al_2O_3 nanocomposite powder particles under as-milled condition and after annealing at 600 °C for 5 h, and the grain size distributions of the nanocrystalline Cu matrix of the samples under these two heat treatment conditions, respectively. The grain size distributions of the nanocrystalline Cu matrix of the nanocomposite samples were determined by measuring the sizes of 188 and 247 Cu grains in the microstructures. As shown by the results of the TEM examination of the as-milled and annealed powder particles, the grain sizes of the nanocrystalline

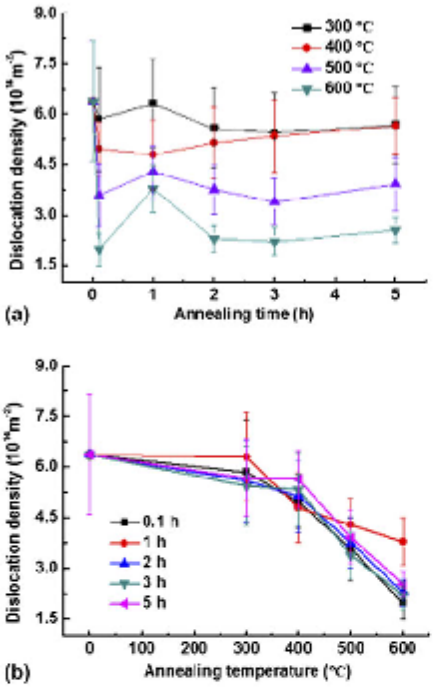

FIG. 3. Variation of dislocation density of nanostructured Cu–5 vol% Al_2O_3 nanocomposite powder particles with annealing time at different annealing temperatures (a) and with annealing temperature for different annealing times (b).

Cu matrix of the nanocomposite under as-milled condition were in the range of 17–120 nm, with the average value being 50 ± 20 nm, whereas after annealing for 5 h at 600 °C, the majority of Cu grains grew slightly larger, with the sizes being in the range of 20–200 nm. Some large Cu grains with sizes in the range of 200–300 nm and surrounded by nanometer-sized Cu grains were also found in the microstructure of the powder particles annealed for 5 h at 600 °C, as shown in Fig. 4(b), indicating that abnormal grain growth occurred during annealing at 600 °C. The average grain size of the Cu matrix of the nanocomposite particles after annealing for 5 h at 600 °C was 91 ± 47 nm. As shown by the selected area electron diffraction patterns shown in Figs. 5(a) and 5(b), annealing as-milled powder particles at 600 °C for 5 h generated a group of weak diffraction spots corresponding to Al_2O_3 {311} [Fig. 5(b)], which were absent from the SADP of the as-milled powder particle [Fig. 5(a)]. This implies that the growth of Al_2O_3 nanoparticles occurred during annealing at 600 °C.

As shown by the SEM backscattered electron images, STEM images and EDX Al elemental maps shown in Figs. 6 and 7, a fraction of Al_2O_3 nanoparticles were dissolved during milling, and relatively large Al_2O_3 nanoparticles survived in the microstructure of the as-milled powder. With the subsequent annealing, the Al^{3+} and O^{2-} ions re-precipitated out to either form new Al_2O_3 nanoparticles or to cause the growth of pre-existing Al_2O_3 nanoparticles, as shown in Figs. 6(b)–6(d) and 7(c) and 7(d). This is in agreement with the appearance of the Al_2O_3 {311} diffraction spots in the SADP of the powder particle annealed at 600 °C and for 5 h shown in Fig. 5.

Figure 8 displays the change of the microhardness of the Cu–5 vol% Al_2O_3 nanocomposite powder particles with increasing annealing time at different annealing temperatures. It shows that the value of the microhardness of the Cu–5 vol% Al_2O_3 nanocomposite powder particles annealed at a given annealing temperature decreased with increasing annealing time within the first 2 h annealing and then reached a plateau with further increase in annealing time. Moreover, the microhardness of the annealed Cu–5 vol% Al_2O_3 nanocomposite powder particles decreased from 259 to 168 Hv with increasing annealing temperature from room temperature to 600 °C. Such changes in the microhardness of the powder particles with the annealing condition clearly reflects the Cu grain growth behavior shown in Fig. 2 and the decrease of the dislocation density of the powder particles with increasing annealing time and annealing temperature shown in Fig. 3.

IV. DISCUSSION

A. Microstructural evolution during annealing

As shown in Figs. 2 and 3, when the as-milled powder particles are annealed at temperatures ≤400 °C, the average Cu grain size remains nearly unchanged, whereas those powder particles annealed at temperatures ≥500 °C exhibit clear grain growth (Fig. 2). This observation is similar to the finding obtained by Čížek et al.[29] that no visible grain growth or recrystallization of the nanocrystalline Cu matrix occurs during annealing of Cu–0.5 wt.% Al_2O_3 nanocomposite at temperatures below 400 °C. In contrast, the dislocation density of the as-milled powder particles decreases continuously with increasing annealing temperature from 300 to 600 °C (Fig. 3). Abnormal grain growth occurs during annealing at 600 °C, as shown in Fig. 4(b). This might be caused by the coarsening of Al_2O_3 nanoparticles during annealing. As shown in Figs. 6, 7, and 9, a fraction of the Al_2O_3 particles of the as-milled powder particles coarsen and their sizes reach a level larger than 100 nm after annealing at 600 °C for 5 h. These large Al_2O_3 particles are less effective in dragging the migration of grain boundaries and thus allow faster grain growth than Al_2O_3 nanoparticles smaller than 50 nm during annealing.[30] As a result, some grains adjacent to large Al_2O_3 particles grew abnormally, as shown in Fig. 4(b).

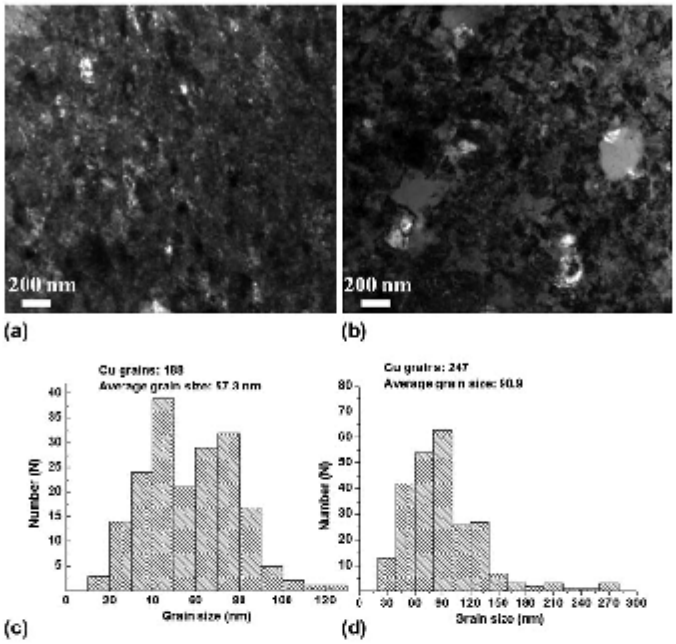

FIG. 4. (a) and (b) TEM bright field micrographs of the microstructure of the nanostructured Cu–5 vol% Al_2O_3 nanocomposite powder particles under as-milled condition and after annealing at 600 °C for 5 h, respectively; and (c) and (d) their corresponding grain size distributions, respectively.

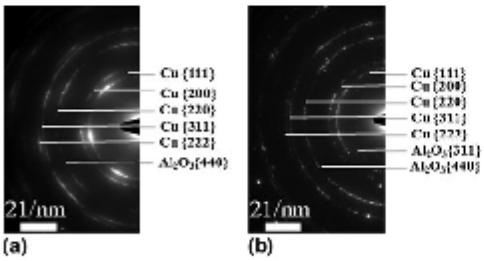

FIG. 5. Selected area electron diffraction patterns corresponding to the TEM micrographs shown in Figs. 4(a) and 4(b), respectively.

As shown in Fig. 3(a), for samples annealed at 300, 500, and 600 °C, respectively, the dislocation density is found to increase with increasing annealing time from 10 min to 1 h and then decrease with further increasing annealing time. A possible reason for this behavior might be that there is residual elastic strain (and stress) at the Al_2O_3 nanoparticle/Cu matrix interfaces caused by incompatible plastic deformation of the two phases during milling. Within a short annealing time of 1 h, this residual strain is relaxed and turns into dislocations emitting from the interface. This may cause an increase of dislocation density in the powder particles annealed. In the meantime, the additional free energy of the dislocations would drive their annihilation by reactions among them, their movement to grain boundaries which work as sinks for dislocations and even formation and growth of new dislocation free grains through recrystallization. This will cause a decrease of dislocation density with increasing annealing time. These two opposite effects operate simultaneously during annealing. Due to very high dislocation density of the as-milled powder particles, the rate of the dislocation density decrease caused by the second effect is much higher than that of dislocation increase caused by the first effect, leading to a sharp decrease of the dislocation density in the samples annealed for a very short time of 10 min. With the level of the dislocation density being lower, the second effect becomes weaker, leading to a lower rate of dislocation density decrease, and this makes the first effect become dominant, causing increase of dislocation density. Once the residual elastic strain is relaxed, the first effect diminishes, making the second effect dominant again, leading to decrease of dislocation density with increasing annealing time. For the samples annealed at

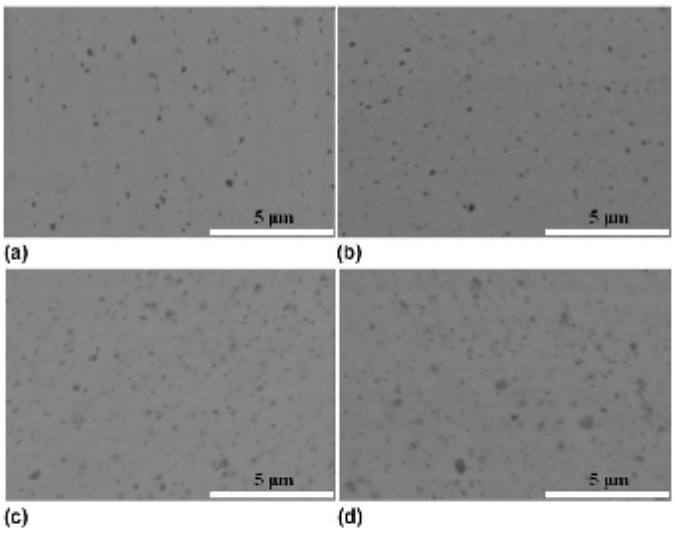

FIG. 6. SEM backscattered electron images showing coarsening of Al_2O_3 nanoparticles in the nanostructured Cu–5 vol% Al_2O_3 nanocomposite powder particles under different annealing conditions: (a) as-milled; (b) 400 °C for 5 h; (c) 500 °C for 5 h; and (d) 600 °C for 5 h.

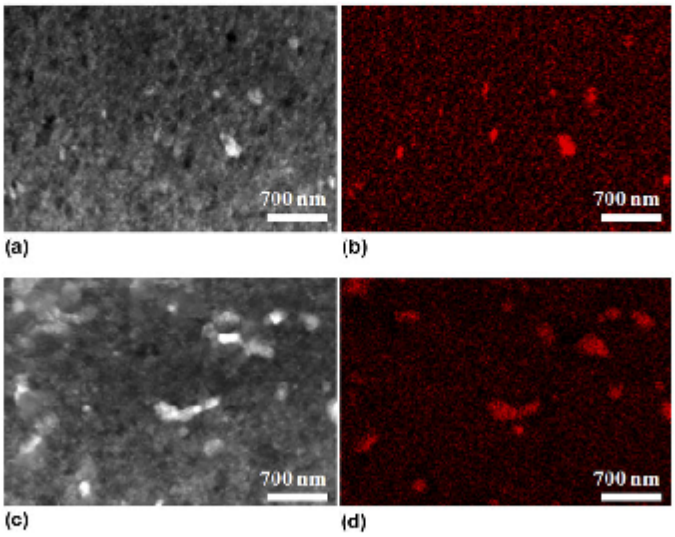

FIG. 7. STEM images of the microstructure of (a) as-milled nanostructured Cu–5 vol% Al_2O_3 nanocomposite powder particles and (c) powder particles annealed at 600 °C for 5 h, respectively, and (b) and (d) their corresponding EDX Al elemental maps, respectively.

400 °C, the dislocation density is found to increase slightly and continuously with increasing annealing time beyond 10 min up to 5 h. The inconsistent behavior of the samples annealed at 400 °C as compared with the samples annealed at 300, 500, and 600 °C, respectively, may be because of the role of temperature in determining the rate of dislocation density increase and decrease due to the two opposite effects as explained above.

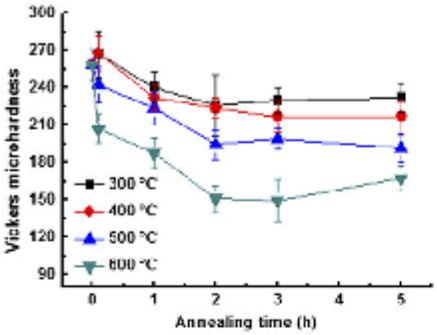

FIG. 8. Microhardness of the nanostructured Cu–5 vol% Al_2O_3 nanocomposite powder particles as a function of annealing time at different annealing temperatures.

B. The kinetics of grain growth of the nanocrystalline Cu matrix

Based on the consideration that the grain growth of a polycrystalline material is driven by the grain boundary curvature, the grain size, D, as a function of annealing time, t, can be described by using a power law equation[31,32]:

$$D^n - D_0^n = kt \quad , \tag{4}$$

where n is a constant, D_0 is the initial grain size at time $t = 0$, and k is a temperature-dependent grain growth rate constant. If the material is a pure single phase material, $n = 2$. However, during grain growth, many factors such as second phase particles,[33] impurities,[13,14] solute atoms,[34] strain release,[35] pores, and grain boundary triple junctions[36,37] can affect the kinetics of grain growth and lead to $n > 2$.[38] In this study, we assume that the curvature-driven grain growth mechanism is still operative and Eq. (4) can be used to quantify the grain growth. Considering the influence of Al_2O_3 nanoparticles on the grain growth of nanocrystalline Cu matrix, we take $n = 3$, and Eq. (4) is rewritten as:

$$D^3 - D_0^3 = kt \quad . \tag{5}$$

The values of k at different annealing temperatures were obtained by fitting Eq. (5) with the grain size data obtained from the isothermal annealing experiments shown in Fig. 2(a). k changes with temperature according to the Arrhenius relationship[31]:

$$k = k_0 \exp\left[-\frac{E}{RT}\right] \quad , \tag{6}$$

where R is the ideal gas constant, T is the absolute temperature, E is the apparent activation energy for grain growth, and k_0 is a constant. Based on Eq. (6), the value of the grain growth activation energy, E, can be obtained from the slope of the line of $\ln(k)$ versus $1/RT$.

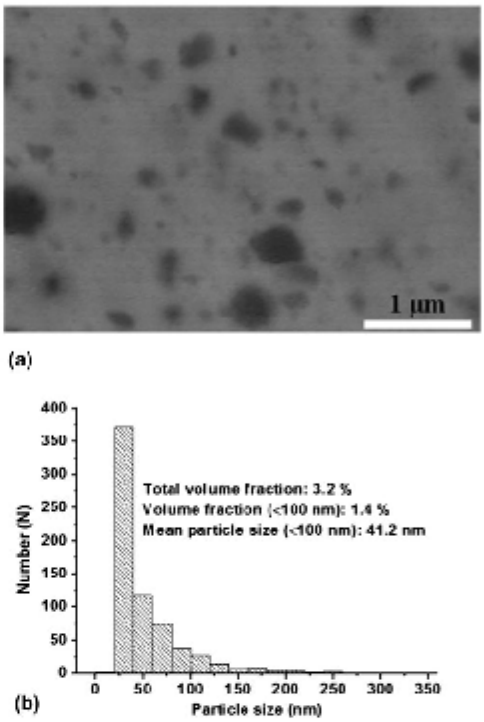

FIG. 9. (a) SEM backscattered electron image of the Cu–5 vol% Al_2O_3 nanocomposite powder particle annealed at 600 °C for 5 h; (b) particle size distribution of the Al_2O_3 nanoparticles.

From the slope of the line which best fits the experimental data points of ($1/RT$, k) at three different annealing temperatures (400, 500, and 600 °C), as shown in Fig. 10, the value of the activation energy of grain growth of the nanocrystalline Cu matrix of the Cu–5 vol% Al_2O_3 nanocomposite powder particles has been determined to be 63.4 kJ/mol. For comparison, the values of the apparent activation energy of grain growth of monolithic nanocrystalline Cu collected from the published literature[35,39–43] along with the value obtained in this study are summarized in Table I. It can be seen that the reported values of the apparent activation energy of grain growth of monolithic nanocrystalline Cu are in the range of 30–83 kJ/mol, which is much smaller than that of the grain growth of microcrystalline Cu (211 kJ/mol).[44] This is not surprising, since the grain growth of nanocrystalline Cu is grain boundary diffusion controlled, whereas the

grain growth of microcrystalline Cu is lattice diffusion controlled. On the other hand, the value of the apparent activation energy of grain growth of the nanocrystalline Cu matrix of the Cu–5 vol% Al_2O_3 nanocomposite (63.4 kJ/mol) falls well into the range of the reported values of the apparent activation energy of grain growth of monolithic nanocrystalline Cu shown in Table I. This shows that the grain growth kinetics of the nanocrystalline Cu matrix of the Cu–5 vol% Al_2O_3 nanocomposite powder particles prepared by HEMM are also controlled by grain boundary diffusion.

C. The effect of Al_2O_3 nanoparticles on the grain growth of nanocrystalline Cu matrix

Fine second phase particles located at grain boundaries exert a retarding force to the grain boundaries so that their migration becomes more difficult. Such an effect can result in a much lower rate of the grain growth of a nanocrystalline metal matrix dispersed with fine second phase particles compared with its monolithic nanocrystalline counterpart. Indeed, although the apparent activation energy of grain growth of the nanocrystalline Cu matrix of the Cu–5 vol% Al_2O_3 nanocomposite [Fig. 2(a)] is very close to that of monolithic nanocrystalline Cu, the growth rate of the former during annealing at elevated temperatures in the range of 400–600 °C is far lower than that of the latter in the same temperature range. This is reflected by the fact that after 5 h annealing at 500 °C, the average grain size of monolithic nanocrystalline Cu increases from 50 to 280 nm,[39] whereas the annealing at a higher temperature of 600 °C for the same time of 5 h only causes the average grain size of the nanocrystalline Cu matrix of the Cu–5 vol% Al_2O_3 nanocomposite only to increase from 57 to 91 nm, as shown in Fig. 4.

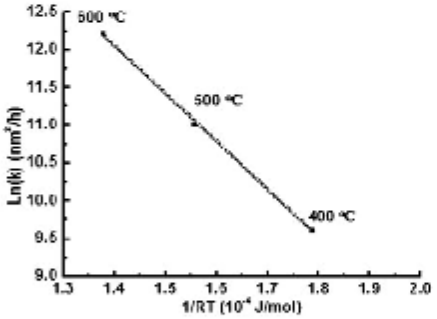

FIG. 10. Arrhenius plot of the grain growth rate constant for the nanocrystalline Cu matrix of the Cu–5 vol% Al_2O_3 nanocomposite powder particles in the temperature range of 400–600 °C.

According to Burke,[31] a balance between the pinning force exerted on a grain boundary by fine second phase particles and the driving force for grain growth can be established in a metal dispersed with second phase particles, and in such a metastable state the grain growth would virtually stop with further annealing at the same temperature. Based on the particle pinning theory of grain growth,[45] the relationship between the particle parameters (i.e., volume fraction, f, and size, d) and grain size, D, can be empirically described by the following equation:

$$\frac{D}{d} = \frac{4}{3f} \quad . \tag{7}$$

The powder particles annealed at 600 °C for 5 h is taken as a model to analyze the effect of Al_2O_3 nanoparticles on the grain growth of nanocrystalline Cu matrix of the Cu–5 vol% Al_2O_3 nanocomposite. In this analysis, Al_2O_3 particles with sizes larger than 100 nm are not taken into account because of their negligible effect on the thermal stability of the nanocrystalline Cu matrix. By substituting $d = 41.19$ nm and $f = 1.36\%$ presented in Fig. 9(b) into Eq. (7), we get $D = 4038$ nm. Apparently, this predicted value of the average grain size of the Cu matrix is by far much larger than the actual average grain size of the nanocrystalline Cu matrix of the Cu–5 vol% Al_2O_3 nanocomposite annealed at 600 °C for 5 h which is 91 nm. As shown by the information in Fig. 9(b), the volume fraction of Al_2O_3 nanoparticles accounted for in the measurement is 3.23 vol%, indicating that there is still ~1.77 vol% Al_2O_3 left in the matrix and which may

TABLE I. Values of apparent activation energy for grain growth of monolithic nanocrystalline Cu published in the literature and that of the nanocrystalline Cu matrix of the Cu–5 vol% Al_2O_3 nanocomposite obtained in this study (IKA: isothermal kinetics analysis).

Preparation method	Materials	Temperature range (K)	Study method	Activation energy (kJ/mol)	Reference
Inert gas condensation + compaction	Nanocrystalline Cu (99.95% pure)	283–425	Tracer or nuclear magnetic relaxation	61.56 or 66.37	42,44
DC magnetron sputtering	Nanocrystalline Cu	573–773	IKA ($n = 2$)	38.7	45
DC magnetron sputtering	Nanocrystalline Cu	373–773	IKA ($n = 3$)	35 ± 11	41
Sliding wear	Nanocrystalline Cu (99.2 pure)	575–675	IKA ($n = 4$)	30 ± 9	43
Electrodeposition	Nanocrystalline Cu (99.983 pure)	373–423	IKA ($n = 4$)	83 ± 13	37
HEMM	Nanocrystalline Cu matrix	573–873	IKA ($n = 3$)	63.4 ± 2	This study

be in the form of Al^{3+}/O^{2-} clusters, being too small to be resolved clearly by SEM and TEM. We assume that the Al^{3+}/O^{2-} clusters have an average size of 2 nm and then do the calculation using Eq. (7) again. This calculation generates a value of D of 151 nm, which is fairly close to the actual measured average grain size of 91 nm, considering the simplicity of the model and the level of inaccuracy of the measurement of the average grain size. This means that the high thermal stability of the nanocrystalline Cu matrix of the Cu–5 vol% Al_2O_3 nanocomposite is mainly caused by the pinning effect of Al^{3+}/O^{2-} clusters. In addition, there is a small amount of Fe impurity in the as-milled powder (~0.175 wt.%, as shown by the chemical analysis), and the iron atoms in the lattice and segregated at the grain boundaries of the Cu matrix may impose a retarding force against the motion of the grain boundary via the solute drag effect.

D. The effect of Al_2O_3 nanoparticles on the dislocation density in nanocrystalline Cu matrix

It is expected that the Al_2O_3 nanoparticles also significantly affect the dislocation density of nanostructured Cu matrix in the annealed samples. Upon annealing, Al_2O_3 nanoparticles at the grain boundaries and inside the grains of the nanocrystalline Cu matrix could serve as effective pinning sites for dislocation movement needed for annihilation through reactions among them and moving to grain boundaries which work as dislocation sinks. In addition, Al_2O_3 nanoparticles work as barriers for formation and growth of new grains during recrystallization, and this also effectively reduces the rate of dislocation density decrease with increasing annealing time. As a result of this effect, it is expected that with the same annealing temperature and time, the dislocation density of nanostructured Cu–5 vol% Al_2O_3 nanocomposite powder would be much higher than that of monolithic nanocrystalline pure Cu. This behavior has been reported by Čížek et al.[46]

V. CONCLUSIONS

A systematic investigation of the microstructural changes that occur during isothermal annealing of a nanostructured Cu–5 vol% Al_2O_3 nanocomposite powder prepared by HEMM has been performed. The results show that annealing at 300 or 400 °C only causes a reduction of the dislocation density of the powder particles, whereas annealing at 500 or 600 °C causes reduction of dislocation density, abnormal grain growth of the nanocrystalline Cu matrix, and coarsening of Al_2O_3 nanoparticles of the nanocomposite particles.

Analysis of the grain growth kinetics of the nanocrystalline Cu matrix of the Cu–5 vol% Al_2O_3 nanocomposite shows that the apparent activation energy of the grain growth in the temperature range of 400–600 °C is 63.4 kJ/mol, being very similar to that of monolithic nanocrystalline Cu in the same temperature range. However, the microstructure of the nanocrystalline Cu matrix of the nanocomposite exhibits a far higher thermal stability than that of monolithic nanocrystalline Cu, with most of the Cu grains being still in the nanometer scale after annealing at 600 °C for 5 h. This high thermal stability of the nanocrystalline Cu matrix of the nanocomposite can be attributed to the drag effects of finely distributed Al_2O_3 nanoparticles and Al^{3+}/O^{2-} clusters on the grain boundary motion.

ACKNOWLEDGMENTS

The funding from the China Scholarship Council (CSC), National Natural Science Foundation of China (Project No. 51271115), Ministry of Science and Technology, China (Project No. 2012CB619600), and Ministry of Business, Innovation and Employment, New Zealand (Contract No. UOWX1001) to support this work is gratefully acknowledged.

REFERENCES

1. B.Q. Han, J. Ye, A.P. Newbery, Y.T. Zhu, J.M. Schoenung, and E.J. Lavernia: In *Bulk Nanostructured Materials*, M.J. Zehetbauer and Y.T. Zhu ed.; Wiley-VCH Verlag: Weinheim, 2009; p. 273.
2. D.L. Zhang, S. Raynova, C.C Koch, R.O. Scattergood, and K.M. Youssef: Consolidation of a Cu-2.5 vol.% Al_2O_3 powder using high energy mechanical milling. *Mater. Sci. Eng., A* **410**, 375 (2005).
3. S. Cheng, E. Ma, Y.M Wang, L.J. Kecskes, K.M. Youssef, C.C. Koch, U.P Trociewitz, and K. Han: Tensile properties of in situ consolidated nanocrystalline Cu. *Acta Mater.* **53**(5), 1521 (2005).
4. L. He and E. Ma: Processing and microhardness of bulk Cu-Fe nanocomposites. *Nanostruct. Mater.* **7**(3), 327 (1996).
5. C. Langlois, M.J. Hytch, S. Lartigue-Korinek, Y. Champion, and P. Langlois: Synthesis and microstructure of bulk nanocrystalline copper. *Metall. Mater. Trans. A* **36**(12), 3451 (2005).
6. M. Pozuelo, C. Melnyk, W.H. Kao, and J-M. Yang: Cryomilling and spark plasma sintering of nanocrystalline magnesium-based alloy. *J. Mater. Res.* **26**(07), 904 (2011).
7. C.C. Koch, R.O. Scattergood, K.A. Darling, and J.E. Semones: Stabilization of nanocrystalline grain sizes by solute additions. *J. Mater. Sci.* **43**(23), 7264 (2008).
8. J. Weissmüller: Alloy effects in nanostructures. *Nanostruct. Mater.* **3**(1), 261 (1993).
9. B.K. VanLeeuwen, K.A. Darling, C.C. Koch, R.O. Scattergood, and B.G. Butler: Thermal stability of nanocrystalline $Pd_{81}Zr_{19}$. *Acta Mater.* **58**(12), 4292 (2010).
10. C.E. Krill, H. Ehrhardt, and R. Birringer: Thermodynamic stabilization of nanocrystallinity. *Z. Metallkd.* **96**(10), 1134 (2005).
11. K.A. Darling, B.K. VanLeeuwen, C.C. Koch, and R.O. Scattergood: Thermal stability of nanocrystalline Fe-Zr alloys. *Mater. Sci. Eng., A* **527**(15), 3572 (2010).
12. M.A. Atwater, R.O. Scattergood, and C.C. Koch: The stabilization of nanocrystalline copper by zirconium. *Mater. Sci. Eng., A* **559**, 250 (2013).
13. T.R. Malow and C.C. Koch: Grain growth in nanocrystalline iron prepared by mechanical attrition. *Acta Mater.* **45**(5), 2177 (1997).
14. K.W. Liu and F. Mücklich: Thermal stability of nano-RuAl produced by mechanical alloying. *Acta Mater.* **49**(3), 395 (2001).
15. T. Chookajorn, H.A. Murdoch, and C.A. Schuh: Design of stable nanocrystalline alloys. *Science* **337**(6097), 951 (2012).

16. X. Zhang, N.Q. Vo, P. Bellon, and R.S. Averback: Microstructural stability of nanostructured Cu–Nb–W alloys during high-temperature annealing and irradiation. *Acta Mater.* **59**(13), 5332 (2011).
17. L. Shaw, H. Luo, J. Villegas, and D. Miracle: Thermal stability of nanostructured $Al_{93}Fe_3Cr_2Ti_2$ alloys prepared via mechanical alloying. *Acta Mater.* **51**(9), 2647 (2003).
18. R.J. Perez, B. Huang, and E.J. Lavernia: Thermal stability of nanocrystalline Fe-10 wt.% Al produced by cryogenic mechanical alloying. *Nanostruct. Mater.* **7**(5), 565 (1996).
19. D.G. Morris and M.A. Morris: Microstructure and strength of nanocrystalline copper alloy prepared by mechanical alloying. *Acta Metall.* **39**(8), 1763 (1991).
20. B. Huang, R.J. Perez, and E.J. Lavernia: Grain growth of nanocrystalline Fe–Al alloys produced by cryomilling in liquid argon and nitrogen. *Mater. Sci. Eng., A* **255**(1), 124 (1998).
21. L. Hashemi-Sadraei, S.E. Mousavi, R. Vogt, Y. Li, Z. Zhang, E.J. Lavernia, and J.M. Schoenung: Influence of nitrogen content on thermal stability and grain growth kinetics of cryomilled Al nanocomposites. *Metall. Mater. Trans. A* **43**(2), 747 (2012).
22. E. Botcharova, J. Freudenberger, and L. Schultz: Mechanical and electrical properties of mechanically alloyed nanocrystalline Cu–Nb alloys. *Acta Mater.* **54**(12), 3333 (2006).
23. J.I. Langford and A.J.C. Wilson: Scherrer after sixty years: a survey and some new results in the determination of crystallite size. *J. Appl. Crystallogr.* **11**(2), 102 (1978).
24. U. Holzwarth and N. Gibson: The Scherrer equation versus the "Debye-Scherrer equation". *Nat. Nanotech.* **6**(9), 534 (2011).
25. A.R. Stokes and A.J.C. Wilson: The diffraction of X rays by distorted crystal aggregates-I. *Proc. Phys. Soc.* **56**(3), 174 (1944).
26. G.K. Williamson and R.E. Smallman, III. Dislocation densities in some annealed and cold-worked metals from measurements on the x-ray debye-scherrer spectrum. *Philos. Mag.* **1**(1), 34 (1956).
27. Y.H. Zhao, K. Lu, and K. Zhang: Microstructure evolution and thermal properties in nanocrystalline Cu during mechanical attrition. *Phys. Rev. B* **66**(8), 085404 (2002).
28. S. Ni, Y.B. Wang, X.Z. Liao, S.N. Alhajeri, H.Q. Li, Y.H. Zhao, E.J. Lavernia, S.P. Ringer, T.G. Langdon, and Y.T. Zhu: Grain growth and dislocation density evolution in a nanocrystalline Ni–Fe alloy induced by high-pressure torsion. *Scripta Mater.* **64**(4), 327 (2011).
29. J. Čížek, I. Procházka, M. Cieslar, R. Kužel, Z. Matěj, V. Cherkaska, R.K. Islamgaliev, and O. Kulyasova: Influence of ceramic nanoparticles on grain growth in ultra fine grained copper prepared by high pressure torsion. *Phys. Status Solidi C* **4**(10), 3587 (2007).
30. J. Ďurišin, K. Ďurišinová, M. Orolínová, and K. Saksl: Effect of the MgO particles on the nanocrystalline copper grain stability. *Mater. Lett.* **58**(29), 3796 (2004).
31. J.E. Burke: Some factors affecting the rate of grain growth in metals. *Trans. Metall. Soc. AIME* **180**, 73 (1949).
32. H.V. Atkinson: Overview no. 65: Theories of normal grain growth in pure single phase systems. *Acta Metall.* **36**(3), 469 (1988).
33. F. Zhou, J. Lee, and E.J. Lavernia: Grain growth kinetics of a mechanically milled nanocrystalline Al. *Scripta Mater.* **44**(8–9), 2013 (2001).
34. A. Michels, C.E. Krill, H. Ehrhardt, R. Birringer, and D.T. Wu: Modelling the influence of grain-size-dependent solute drag on the kinetics of grain growth in nanocrystalline materials. *Acta Mater.* **47**(7), 2143 (1999).
35. L. Lu, N.R. Tao, L.B. Wang, B.Z. Ding, and K. Lu: Grain growth and strain release in nanocrystalline copper. *J. Appl. Phys.* **89**(11), 6408 (2001).
36. G. Gottstein, L.S. Shvindlerman, and B. Zhao: Thermodynamics and kinetics of grain boundary triple junctions in metals: Recent developments. *Scripta Mater.* **62**(12), 914 (2010).
37. L.S. Shvindlerman and G. Gottstein: Efficiency of drag mechanisms for inhibition of grain growth in nanocrystalline materials. *Z. Metallkd.* **95**(4), 239 (2004).
38. F.J. Humphreys and M. Hatherly: *Recrystallization and Related Annealing Phenomena*, 2nd ed.; Elsevier Science Ltd.: Oxford, UK, 2004; pp. 200–244.
39. S. Simões, R. Calinas, M.T. Vieira, M.F. Vieira, and P.J. Ferreira: In situ TEM study of grain growth in nanocrystalline copper thin films. *Nanotechology* **21**(14), 145701 (2010).
40. J. Horvath, R. Birringer, and H. Gleiter: Diffusion in nanocrystalline material. *Solid State Commun.* **62**(5), 319 (1987).
41. S.K. Ganapathi, D.M. Owen, and A.H. Chokshi: The kinetics of grain growth in nanocrystalline copper. *Scripta Metall.* **25**(12), 2699 (1991).
42. W. Dickenscheid, R. Birringer, H. Gleiter, O. Kanert, B. Michel, and B. Günther: Investigation of self-diffusion in nanocrystalline copper by NMR. *Solid State Commun.* **79**(8), 683 (1991).
43. Z.H. Cao, F. Wang, L. Wang, and X.K. Meng: Coupling effect of the electric and temperature fields on the growth of nanocrystalline copper films. *Phys. Rev. B* **81**(11), 113405 (2010).
44. H. Mehrer: *Diffusion in Solids: Fundamentals, Methods, Materials, Diffusion-Controlled Processes*, 1st ed.; Springer-Verlag: Berlin, 2007; pp. 304.
45. C.S. Smith: Grains, phases, and interfaces: an interpretation of microstructure. *Met. Technol.* **15**(4), 1 (1948).
46. J. Čížek, I. Procházka, R. Kužel, and R. Islamgaliev: In *Nanostructured Materials*, H. Hofmann, Z. Rahman, and U. Schubert eds.; Springer: Vienna, 2002; p. 137.